

CZECH TECHNICAL UNIVERSITY IN PRAGUE

Faculty of Nuclear Sciences and Physical Engineering

Study of inclusive electron-positron pair production  
in collisions of Ar+KCl at 1.756 A GeV

Doctoral Thesis

**Filip Křížek**

September 3, 2008

Thesis Advisor

**RNDr. Andrej Kugler, CSc.**



Department of Physics  
Faculty of Nuclear Sciences and Physical Engineering  
Czech Technical University in Prague

Břehová 7, CZ-115 19 Prague 1, Czech Republic  
fax: +420 222 320 861, phone: +420 224 351 111

<http://www.fjfi.cvut.cz>

---

---

## Abstract

Spectroscopy of di-leptons emerging in decays of the light vector mesons  $\rho^0$ ,  $\omega$ , and  $\phi$  is a promising way how to investigate changes of properties of these hadrons in the surrounding nuclear environment. This thesis deals with an analysis of inclusive  $e^+e^-$  pair emission from Ar+KCl collisions at a kinetic beam energy of 1.756 A GeV. The measurement was carried out using the High Acceptance Di-Electron Spectrometer (HADES). HADES is a unique apparatus dedicated to study of  $e^+e^-$  pair production in hot and dense hadronic matter. After an introduction to the field, the HADES spectrometer is briefly described. Then we focus on the analysis of the Ar+KCl run. We describe and discuss event selection performed by the on-line trigger, lepton identification, and the subsequent pair analysis. Efficiency corrected spectra of pairs are compared with predictions of a thermal model based Monte Carlo event generator (Pluto) and, further, with forecasts of a microscopic transport code (HSD). Finally, we compare results from the HADES Ar+KCl and C+C runs. With respect to the expected di-electron yield from  $\eta \rightarrow \gamma e^+e^-$  decay, in the invariant mass region 0.15–0.50 GeV/ $c^2$ , our spectra exhibit a large excess of pairs coming from other sources. Within a model dependent approach, it is shown that the total yield from this excess grows for a given size of a collision system with the beam energy similarly to  $\pi^0$  multiplicity. Moreover, there is a hint that the dependence of this excess yield on the number of reaction participants is non-trivial.

---

## Abstrakt

Spektroskopie di-leptonů vznikajících v rozpadech lehkých vektorových mezonů  $\rho^0$ ,  $\omega$  a  $\phi$  se zdá být slibným přístupem jak studovat změny vlastností těchto hadronů v jaderném prostředí. Tato disertační práce se zabývá analýzou experimentu, v němž byla zkoumána produkce  $e^+e^-$  párů ve srážkách Ar+KCl při kinetické energii svazku 1,756 A GeV. Měření proběhlo na di-elektronovém spektrometeru HADES. HADES je jedinečné zařízení, které bylo navrženo a sestrojeno pro studium tvorby  $e^+e^-$  párů v horké a husté jaderné hmotě. Po úvodu do problematiky je v krátkosti načrtnuta stavba spektrometru HADES. Následně se zaměříme na analýzu experimentu Ar+KCl. Popíšeme a budeme diskutovat výběr reakcí triggerem, identifikaci leptonů a navazující analýzu párů. Spektra párů opravená na efektivitu rekonstrukce a identifikace srovnáme s předpovědí programu Pluto, založeném na termálním modelu, a dále pak s výpočtem transportního kódu HSD. Na závěr porovnáme výsledky experimentů, v nichž HADES zkoumal produkci di-elektronů v reakcích Ar+KCl a C+C. Oproti předpokládanému výtěžku di-elektronů z rozpadu  $\eta \rightarrow \gamma e^+e^-$  jsme v oblasti invariantních hmotností 0,15–0,50 GeV/ $c^2$  zjistili značný přebytek párů pocházejících z jiných zdrojů. V rámci modelového přístupu ukážeme, že tento nadbytečný výtěžek roste pro danou velikost reakčního systému s energií svazku stejně rychle jako multiplicita  $\pi^0$ . Navíc lze očekávat netriviální závislost jeho velikosti na počtu nukleonů účastnících se reakce.

---

## Acknowledgments

In the first place, I would like to thank to Dr. Pavel Tlustý for his help, patience, and fruitful discussions. Then there is a very long list of persons which merit my gratefulness for introducing me into the analysis and worthwhile advices. So my thanks belong also to Dr. Malgorzata Sudol, Dr. Simon Lang, Dr. Alexander Schmah, Martin Jurkovič, Dr. Jacek Otwinowski, Dr. Piotr Salabura, Dr. Romain Holzmann, Dr. Tassilo Christ, Dr. Yvonne Pachmayer, Dr. Jochen Markert, Dr. Ilse Koenig, Dr. Jurek Pietraszko, Dr. Witold Przygoda, Dr. Jehad Mousa, Dr. Vladimír Wagner, and many others. I owe a lot to my supervisor Dr. Andrej Kugler for careful reading the thesis and his comments. Finally, I would like to thank to my family for their love, understanding, and support.

The presented research was supported by GA AS CR IAA100480803, MSMT LC07050, and INTAS 06-1000012-8861.

## Declaration

Hereby I declare that this dissertation is a result of my own work, except where explicit reference to the work of others is made, and has not been formerly submitted to another university for degree purposes.

# Contents

<b>1. Introduction</b>	<b>1</b>
1.1. Real and virtual photons . . . . .	1
1.2. Di-lepton production in relativistic A+A collisions . . . . .	2
1.3. Goals of the thesis . . . . .	2
1.4. Layout of the thesis . . . . .	3
<b>2. State of the art</b>	<b>5</b>
2.1. Lagrangian of QCD . . . . .	5
2.2. Symmetries of QCD . . . . .	6
2.3. Vacuum condensates . . . . .	7
2.4. In-medium condensates . . . . .	8
2.5. In-medium changes of the light vector mesons . . . . .	10
2.5.1. Effective meson Lagrangians . . . . .	10
2.5.2. Finite density . . . . .	11
2.6. Spectroscopy of the light vector mesons in medium . . . . .	12
2.7. Nuclear densities close to $\rho_0$ . . . . .	13
2.8. Nuclear densities up to 2–3 $\rho_0$ . . . . .	16
2.9. Nuclear densities up to 3–4 $\rho_0$ . . . . .	19
2.10. High energy densities at RHIC . . . . .	21
<b>3. HADES spectrometer</b>	<b>23</b>
3.1. RICH . . . . .	23
3.2. Tracking system . . . . .	25
3.2.1. MDC . . . . .	25
3.2.2. Magnet . . . . .	26
3.3. Time of flight wall . . . . .	27
3.3.1. TOF . . . . .	27
3.3.2. TOFino . . . . .	29
3.4. Shower . . . . .	29
3.5. START and VETO detectors . . . . .	30
3.6. Trigger and data acquisition system . . . . .	30
3.6.1. First level trigger . . . . .	31
3.6.2. Second level trigger . . . . .	32
3.7. Software tools . . . . .	32
<b>4. Ar+KCl @ 1.756 A GeV</b>	<b>33</b>
4.1. Target and beam . . . . .	34
4.2. Calibration of the TOF detector . . . . .	34

---

<b>5. Trigger studies</b>	<b>37</b>
5.1. Empty target run . . . . .	37
5.2. Event vertex cut . . . . .	38
5.3. Simulation of the LVL1 trigger . . . . .	38
5.4. Simulation of the LVL2 trigger . . . . .	41
5.5. Impact parameter distribution . . . . .	42
5.6. Summary of this chapter . . . . .	43
<b>6. Lepton analysis</b>	<b>45</b>
6.1. Lepton identification in RICH . . . . .	45
6.1.1. RICH-inner MDC matching . . . . .	47
6.1.2. Ring quality parameters . . . . .	48
6.2. Lepton identification in the Time of flight wall . . . . .	49
6.3. Lepton identification in Shower . . . . .	49
6.4. Track selection . . . . .	51
6.5. Single lepton spectra . . . . .	55
6.6. Purity of the selected lepton sample . . . . .	59
6.6.1. Fake ring-track matchings . . . . .	59
6.6.2. Purity of lepton sample in simulations . . . . .	62
6.7. Single lepton LVL2 trigger efficiency . . . . .	64
<b>7. Pair analysis</b>	<b>65</b>
7.1. Pair Background . . . . .	66
7.2. Reconstruction of combinatorial background . . . . .	66
7.3. Background rejection . . . . .	67
7.4. Mixed-event background . . . . .	73
7.5. Efficiency correction . . . . .	79
7.6. Normalization . . . . .	82
7.7. Estimation of systematic error . . . . .	85
<b>8. Discussion of results</b>	<b>87</b>
8.1. Comparison with Pluto . . . . .	87
8.2. Comparison with HSD . . . . .	91
8.3. Comparison to lighter systems . . . . .	96
<b>9. Summary and conclusions</b>	<b>103</b>
<b>A. Efficiency correction</b>	<b>106</b>
<b>Bibliography</b>	<b>113</b>

# Notation

In the following text, the natural system of units  $c = \hbar = 1$  is mostly adopted. Hence, the relation between energetic units and units of length is

$$\hbar c = 1 \doteq 197 \text{ MeV fm.}$$

The standard representation of the Dirac matrices  $\gamma_\mu$  is considered

$$\gamma_0 = \begin{pmatrix} I & 0 \\ 0 & -I \end{pmatrix}, \gamma_1 = \begin{pmatrix} 0 & \sigma_1 \\ -\sigma_1 & 0 \end{pmatrix}, \gamma_2 = \begin{pmatrix} 0 & \sigma_2 \\ -\sigma_2 & 0 \end{pmatrix}, \gamma_3 = \begin{pmatrix} 0 & \sigma_3 \\ -\sigma_3 & 0 \end{pmatrix},$$

where  $I$  is the unit matrix  $2 \times 2$  and  $\sigma_i$  are the Pauli  $2 \times 2$  matrices. The  $\gamma_5$  matrix is defined as

$$\gamma_5 = i\gamma_0\gamma_1\gamma_2\gamma_3 = \begin{pmatrix} 0 & I \\ I & 0 \end{pmatrix}.$$

The well-known anticommutation relations of the Dirac matrices are

$$\{\gamma_\mu, \gamma_\nu\} = \gamma_\mu\gamma_\nu + \gamma_\nu\gamma_\mu = 2g_{\mu\nu} \quad \text{and} \quad \{\gamma_5, \gamma_\mu\} = \gamma_5\gamma_\mu + \gamma_\mu\gamma_5 = 0,$$

where  $g_{\mu\nu} = \text{diag}(1, -1, -1, -1)$  is a diagonal metric matrix.

Let us also recall the frequently used set of the Gell-Mann matrices

$$\lambda_1 = \begin{pmatrix} 0 & 1 & 0 \\ 1 & 0 & 0 \\ 0 & 0 & 0 \end{pmatrix}, \lambda_2 = \begin{pmatrix} 0 & -i & 0 \\ i & 0 & 0 \\ 0 & 0 & 0 \end{pmatrix}, \lambda_3 = \begin{pmatrix} 1 & 0 & 0 \\ 0 & -1 & 0 \\ 0 & 0 & 0 \end{pmatrix}, \lambda_4 = \begin{pmatrix} 0 & 0 & 1 \\ 0 & 0 & 0 \\ 1 & 0 & 0 \end{pmatrix},$$

$$\lambda_5 = \begin{pmatrix} 0 & 0 & -i \\ 0 & 0 & 0 \\ i & 0 & 0 \end{pmatrix}, \lambda_6 = \begin{pmatrix} 0 & 0 & 0 \\ 0 & 0 & 1 \\ 0 & 1 & 0 \end{pmatrix}, \lambda_7 = \begin{pmatrix} 0 & 0 & 0 \\ 0 & 0 & -i \\ 0 & i & 0 \end{pmatrix}, \lambda_8 = \begin{pmatrix} \frac{1}{\sqrt{3}} & 0 & 0 \\ 0 & \frac{1}{\sqrt{3}} & 0 \\ 0 & 0 & \frac{-2}{\sqrt{3}} \end{pmatrix}.$$

The Einstein's summation convention, i.e., summing over repeating indices is adopted.

For a scalar product of two vectors of a dimension  $n$  we have

$$t_a\theta_a = \vec{t}\vec{\theta} = \sum_{a=1}^n t_a\theta_a.$$

Greek alphabet indices are the Lorentz space-time indices. The tensor  $g_{\mu\nu}$  plays an important role when transforming from the covariant to the contravariant indices

$$\gamma_\mu\gamma^\mu = g_{\mu\nu}\gamma^\mu\gamma^\nu = g^{\mu\nu}\gamma_\mu\gamma_\nu.$$

If a local fermion field operator is denoted by  $\psi$  then  $\bar{\psi}$  is defined in the standard way as

$$\bar{\psi} = \psi^+\gamma_0.$$

Here  $\psi^+$  stands for the Hermitian conjugate of the operator  $\psi$ .

# Abbreviations

GSI	Gesellschaft fuer Schwerionenforschung
SIS	Schwerionen Synchrotron
HADES	High Acceptance Di-Electron Spectrometer
DLS	Dilepton Spectrometer
TAPS	Two Arm Photon Spectrometer
HSD	Hadron String Dynamics
UrQMD	Ultrarelativistic Quantum Molecular Dynamics
RICH	Ring Imaging Cherenkov
MDC	Multiwire Drift Chamber
TOF	part of Time of flight wall ( $45^\circ < \theta < 88^\circ$ )
TOFino	part of Time of flight wall ( $18^\circ < \theta < 45^\circ$ )
HYDRA	Hades sYstem for Data Reduction and Analysis
LVL1	first level trigger
LVL2	second level trigger

---

# 1 Introduction

Current nuclear physics is greatly interested in properties of hot and dense hadronic matter. Open questions concerning quark-gluon plasma, the exact form of the nuclear equation of state, or modifications of hadrons in medium are only few examples of problems, which are strong motives for this kind of research.

The High Acceptance Di-Electron Spectrometer (HADES) is one of the experiments designed to collect data about particle properties in nuclear medium. It works at GSI Darmstadt since 2001. The GSI accelerator facility SIS provides beams of heavy ions up to gold having kinetic energies up to 2 A GeV. In the phase diagram of hadronic matter in Figure 1.1, we may see the region where HADES operates.

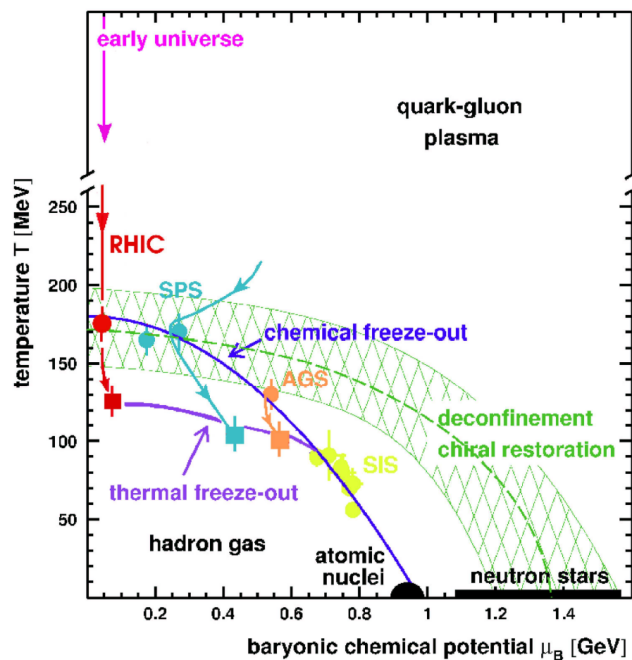


Figure 1.1.: Phase diagram of hot and dense hadronic matter in the temperature and baryon chemical potential plane [1]. The colour points indicate freeze-out points at SIS, AGS, and SPS energies.

## 1.1. Real and virtual photons

Hot and dense hadronic matter produced in (ultra)relativistic heavy ion collisions is a very fleeting state. Real and virtual photons are recognized to be the convenient probes, which may deliver us information about this medium. These particles have many advantageous properties. Real photons interact only electromagnetically, hence they leave the collision zone undistorted. Virtual photons can directly couple to the light vector mesons  $\rho^0$ ,  $\omega$ , and  $\phi$ . Thus, these vector mesons have a “weakly”

interacting di-lepton decay mode; however, branching ratio to this channel is rather small. From the phenomenological point of view, it is also important that the electromagnetic interaction is theoretically well understood. The light vector mesons, see Table 1.1, live only for a very short time and a significant part of them decays already inside hot and compressed nuclear medium. Therefore, a lepton pair originating from a decay of a vector meson brings us direct information about properties which this meson had in the surrounding dense baryonic environment.

Vector meson	Mass [MeV]	Width [MeV]	$c\tau$ [fm]	Dominant decay mode	Branching ratio to $e^+e^-$ channel
$\rho^0$	770	149.2	1.3	$\pi\pi$	$4.5 \times 10^{-5}$
$\omega$	782	8.44	23.4	$\pi^+\pi^0\pi^-$	$6.9 \times 10^{-5}$
$\phi$	1019	4.26	46.3	$K^+K^-$	$2.9 \times 10^{-4}$

Table 1.1.: Properties of the light neutral vector mesons [2].

In nucleus-nucleus collisions, many other types of particles are also produced, e.g., pions, kaons, and etas. However, these hadrons undergo the final state interaction. Thus, information about the place, where these particles emerged, is corrupted or lost already before the freeze-out point.

## 1.2. Di-lepton production in relativistic A+A collisions

Lepton pairs are produced in all stages of a relativistic heavy ion collision. Already when two nuclei approach each other, di-leptons can be generated from the decelerating Coulomb field by means of coherent Bremsstrahlung [3]. Nevertheless, this contribution to the total di-lepton yield is found to be negligible. In the next step, both nuclei overlap and their baryonic matter is compressed and heated. According to the initial energy, interactions proceed either on the partonic or on the hadronic level. If we restrict our description only to low energy processes then at this stage, many mesons are created and baryons may be excited to resonant states. The nuclear liquid medium changed to a hadron gas. Di-leptons originate from various processes, e.g., resonance and vector meson decays, pion or kaon annihilation. The volume of the hot hadronic matter gradually expands. After it reaches the freeze-out point, di-leptons are still produced in Dalitz decays of  $\pi^0$ ,  $\eta$ ,  $\omega$ , and  $\phi$ .

## 1.3. Goals of the thesis

One of the key motives which triggered construction of the HADES spectrometer was to solve the so-called ‘‘DLS puzzle’’ [4]. The DLS experiment measured di-electrons emerging in nuclear collisions during the nineties. Beam was provided by the Bevalac accelerator (1–2 A GeV). It turned out that transport models of the time

had problems with reproducing the DLS data from heavy ion collisions. Measured di-lepton yields showed a strong excess over predictions of all transport models in the invariant mass region 0.3–0.6 GeV. Similar difficulties with data interpretation were reported also by other experiments, like CERES [8] or HELIOS-3 [47]. Theorists suggested various scenarios in order to explain the observed excess in the pair yield. Often it was thought that the excess has a connection with a partially restored chiral symmetry in nuclear medium. But maybe only some important source of di-leptons was omitted. The HADES collaboration intends to repeat some of the DLS measurements with improved mass resolution. Further, they also plan to investigate di-electron production in new systems like  $\pi+N$  or  $\pi+A$ .

The subject of this thesis is an analysis of the recent HADES measurement of inclusive di-electron production in collisions of Ar+KCl at a kinetic beam energy of 1.756 A GeV. The main goals of the thesis are the following:

- to analyse electron-positron pairs from this experiment,
- to compare the obtained efficiency corrected pair spectra with predictions of a microscopic transport code,
- to compare the obtained efficiency corrected pair spectra with the available experimental data from lighter collision systems.

## 1.4. Layout of the thesis

In Chapter 2, I briefly summarize concept of the chiral symmetry. It will be discussed why this symmetry is spontaneously broken in nature and why it should partially restore in hot and dense hadronic medium. Further, this chapter contains an overview on results of the experiments which use electromagnetic probes to study properties of vector mesons in nuclear medium. In Chapter 3, the HADES spectrometer is described. Starting from the Chapter 4, I concentrate on analysis of the HADES run which was dedicated to the measurement of inclusive di-electron production in collisions of Ar+KCl at a kinetic beam energy of 1.756 A GeV. In Chapter 8, obtained results will be compared with predictions of a thermal model based Monte Carlo event generator (Pluto) and a sophisticated transport code (HSD). Finally, the efficiency corrected invariant mass spectra from the Ar+KCl measurement and the C+C runs of HADES are compared. Chapter 9 summarizes this thesis and emphasizes the main contributions and results.

## 1. Introduction

---

## 2 State of the art

### 2.1. Lagrangian of QCD

Quantum Chromodynamics (QCD) belongs to the successful family of gauge field theories. It describes strong interactions of coloured particles, quarks and gluons, which are the fundamental constituents of all hadrons. The QCD Lagrangian  $\mathcal{L}_{QCD}$  can be derived from a free fermion field Lagrangian when a local gauge transformation invariance with respect to the group  $SU(3)_{Colour}$  is required,

$$\mathcal{L}_{QCD} = -\frac{1}{4}\vec{G}_{\mu\nu}\vec{G}^{\mu\nu} + \bar{\Psi}(i\partial_\mu\gamma^\mu - \mathcal{M}^0)\Psi + g\bar{\Psi}\gamma_\mu\vec{t}\vec{A}^\mu\Psi. \quad (2.1)$$

Here  $\Psi = (u, d, s, c, b, t)^\top$  is the vector of all quark flavour fields each having three colour components,  $g$  is the coupling constant, and  $\mathcal{M}^0$  is the diagonal  $6 \times 6$  matrix containing current quark masses  $\mathcal{M}^0 = \text{diag}(m_u^0, m_d^0, m_s^0, \dots)$ . In the scalar product  $\vec{t}\vec{A}^\mu$ , the eight  $SU(3)_{Colour}$  group generators  $\vec{t}$  are multiplied with the eight gluon fields  $\vec{A}^\mu$ . The vector of eight gauge invariant gluon field tensors is denoted as  $\vec{G}^{\mu\nu}$ . Its  $a$ -th component is defined as

$$G_a^{\mu\nu} = \frac{\partial A_a^\nu}{\partial x_\mu} - \frac{\partial A_a^\mu}{\partial x_\nu} + gf_{abc}A_b^\mu A_c^\nu,$$

where  $f_{abc}$  stands for the structure constants of the group  $SU(3)_{Colour}$ . Let us point out that this definition of  $G_a^{\mu\nu}$  is similar to the photon field tensor known from Quantum Electrodynamics (QED); nevertheless, there is one substantial difference. The last term in the above definition is responsible for three and four gluon vertices in QCD. Such photon contact vertices cannot appear in QED.

As a consequence of renormalization of quantum-loops in QCD, it follows that the interaction coupling constant  $g$  depends on a space-time distance, or equivalently, on the four-momentum  $Q$  transferred in the given strong process. Therefore, the strong interaction ‘‘fine-structure constant’’  $\alpha_s \equiv g^2/4\pi$  changes according to the formula

$$\alpha_s(Q) = \frac{\alpha_s(\Lambda)}{1 + \alpha_s(\Lambda)\frac{33-2N_f}{12\pi}\ln\left(\frac{Q^2}{\Lambda^2}\right)}, \quad (2.2)$$

where  $\Lambda$  stands for the scale at which the coupling constant is to be fixed by an experiment and  $N_f$  is the number of quark flavours.

The above equation suggests that  $\alpha_s$  gets smaller with growing  $Q^2$ . For sufficiently large four-momenta transferred, this results that QCD can be treated using perturbation theory. Moreover, in the limit  $Q^2 \rightarrow \infty$ , the so-called *asymptotic freedom*, i.e., non-interaction between colour particles, is reached. On the other hand, at momentum scales of  $\sqrt{Q^2} \simeq 1$  GeV, the strong interaction ‘‘fine-structure constant’’ increases towards smaller  $\sqrt{Q^2}$  so rapidly that the perturbative approach breaks down. Relevant degrees of freedom of the field theory change from quarks and gluons to colourless hadrons and the colour *confinement* establishes.

## 2.2. Symmetries of QCD

Apart from the  $SU(3)_{Colour}$  symmetry, the QCD Lagrangian has also the global  $U(1)_V$  symmetry, i.e., it is invariant with respect to a phase transformation of  $\Psi$ . As follows from the Noether's theorem this implies the conservation of the baryon current. Further, some other symmetries reveal in the limit of vanishing current quark masses. This limit can be justified for the light quarks  $u$  and  $d$  and with somewhat lesser extent also for the strange quark  $s$ . Therefore, from now on, only this  $SU(3)_{Flavour}$  sector will be considered, which is of crucial importance for light mesons.

Massless fermions with the spin 1/2 have properly defined projection of their spin to the direction of their motion, the so-called *helicity* or *chirality*. Such fermions can only be left-handed or right-handed. Hence, a local fermion field operator can be decomposed to these two components

$$\psi_L = \frac{1}{2}(1 - \gamma_5)\psi \quad \text{and} \quad \psi_R = \frac{1}{2}(1 + \gamma_5)\psi.$$

When this decomposition is applied in Equation (2.1) together with  $\mathcal{M}^0 \rightarrow 0$ , we obtain

$$\mathcal{L} = -\frac{1}{4}\vec{G}_{\mu\nu}\vec{G}^{\mu\nu} + \bar{\Psi}_L iD_\mu \gamma^\mu \Psi_L + \bar{\Psi}_R iD_\mu \gamma^\mu \Psi_R,$$

where  $D_\mu = \partial_\mu - i\vec{t}\vec{A}_\mu$  stands for the so-called covariant derivative. The Lagrangian is now invariant with respect to simultaneous global  $SU(3)_{Flavour}$  group transformations of the left-handed and the right-handed fermion fields

$$\Psi_L \longrightarrow \exp\left(-i\vec{\alpha}_L \frac{\vec{\lambda}}{2}\right)\Psi_L \quad \text{and} \quad \Psi_R \longrightarrow \exp\left(-i\vec{\alpha}_R \frac{\vec{\lambda}}{2}\right)\Psi_R,$$

where  $\vec{\alpha}_L$  and  $\vec{\alpha}_R$  are the vectors of eight arbitrary real constants and  $\vec{\lambda}$  is the vector of the eight Gell-Mann matrices. This symmetry, i.e.,  $SU(3)_L \otimes SU(3)_R$ , is called the *chiral symmetry*, see [5]. It implies that left- and right-handed quarks are dynamically not mixed.

The  $SU(3)_L \otimes SU(3)_R$  symmetry is equivalent to the global vector and the axialvector transformations

$$\Psi \longrightarrow \exp\left(-i\vec{\alpha}_V \frac{\vec{\lambda}}{2}\right)\Psi \quad \text{and} \quad \Psi \longrightarrow \exp\left(-i\vec{\alpha}_A \frac{\vec{\lambda}}{2}\gamma_5\right)\Psi$$

in the  $SU(3)$  flavour space. The corresponding conserved charges are

$$Q_V^i = \int d^3x \bar{\Psi} \gamma_0 \frac{\lambda^i}{2} \Psi \quad \text{and} \quad Q_A^i = \int d^3x \bar{\Psi} \gamma_0 \gamma_5 \frac{\lambda^i}{2} \Psi.$$

It can be shown that the conservation of the left- and the right-handed four-currents implies the conservation of the vector and the axialvector four-currents and vice versa.

When the current quark masses tend to zero, the Lagrangian of QCD has also the global  $U(1)_A$  symmetry

$$\Psi \longrightarrow \exp(-i\alpha\gamma_5) \Psi .$$

Here  $\alpha$  is an arbitrary real constant. However, it is known that this symmetry is broken in nature, see [5, 10]. This breaking is manifested by the large mass of the  $\eta'$  meson ( $m_{\eta'} = 958$  MeV) which is much higher with respect to masses of the other pseudoscalar mesons  $\pi$ , K, and  $\eta$ . Theory states that the  $\eta'$ 's mass excess is a consequence of the  $U(1)_A$  axial anomaly.

To complete the list of possible symmetries of the QCD Lagrangian, let us also mention that in the limit of infinitely heavy quarks, it possesses the so-called *central symmetry*. As masses of quark fields are large, their kinetic term can be omitted. The Lagrangian then describes only gluon-dynamics and interactions of gluons with static quarks. There are indications that the central symmetry is related to the confinement.

But now, let us return back to the case when quark masses vanish and the symmetry of the QCD Lagrangian is reduced to  $U(1)_V \otimes SU(3)_L \otimes SU(3)_R$ , or equivalently to  $U(1)_V \otimes SU(3)_V \otimes SU(3)_A$ .

## 2.3. Vacuum condensates

It is thought that in nature, the symmetry  $U(1)_V \otimes SU(3)_V \otimes SU(3)_A$  is spontaneously broken down to  $U(1)_V \otimes SU(3)_V$  in the QCD vacuum. The QCD Hamiltonian has thus more symmetries than the ground state. While

$$[Q_A^i, H_{QCD}] = 0 ,$$

holds for  $i = 1, \dots, 8$ , the charges  $Q_A^i$  do not annihilate the vacuum  $Q_A^i |0\rangle \neq 0$ , more details can be found in [11]. Signals supporting this conjecture are twofold:

1. Existence of the eight (nearly massless) Goldstone bosons, i.e., pions, kaons, and  $\eta$ . Their spin and parity quantum numbers are  $J^P = 0^-$ .
2. Absence of parity doublets. If the chiral symmetry was unbroken, one would expect to have degenerate hadronic isospin multiplets with the opposite parity [11]. This was not seen in experiments.

In [11], it is shown that a sufficient condition for the observed spontaneous symmetry breaking would be the existence of a non-vanishing scalar quark condensate  $\langle \bar{\Psi}\Psi \rangle$  in the QCD vacuum. Value of this condensate can be estimated from the Gell-Mann-Oakes-Renner relation [9]

$$m_\pi^2 f_\pi^2 = -2M \langle \bar{q}q \rangle , \tag{2.3}$$

where  $M$  stands for the average current mass of the  $u$  and the  $d$  quark, i.e.,  $M = (m_u^0 + m_d^0)/2 \approx 6$  MeV. The symbol  $m_\pi$  denotes the pion mass and  $f_\pi = 93$  MeV is the pion decay constant. Derivation of Equation (2.3) assumes isospin symmetry in

the scalar quark condensate  $\langle \bar{q}q \rangle = \langle \bar{u}u \rangle = \langle \bar{d}d \rangle$ . This condensate plays a role of the parameter of spontaneous chiral symmetry breaking. The Gell-Mann-Oakes-Renner relation thus connects the parameters of the spontaneous ( $\langle \bar{q}q \rangle$ ) and the explicit ( $m_u^0, m_d^0$ ) chiral symmetry breaking with the corresponding pion structure constants ( $m_\pi, f_\pi$ ). From the known values, it was obtained

$$\langle \bar{q}q \rangle = -(240 \text{ MeV})^3 = -1.8 \text{ fm}^{-3}.$$

The Nambu and Jona-Lasinio model [10] (NJL) offers a phenomenological description of the scalar quark condensate. The NJL model is based on an effective Lagrangian approach and describes low energetic quark interactions. The gluon degrees of freedom are frozen and quarks interact only via a local fermion-fermion coupling. This model shows a mechanism how the constituent quark mass emerges due to an effective interaction between a quark and the condensate. In the NJL approach, the quark condensate represents a scalar density of the filled negative energy Dirac sea integrated up to momenta  $|\vec{p}| \leq \Lambda_{cut}$ . The cut-off parameter  $\Lambda_{cut}$  is added into this model in order to make it renormalizable.

## 2.4. In-medium condensates

Medium modifications of the quark condensate are a great challenge for the current theoretical physics. The main goal is to study, how various density and temperature conditions may partially restore the chiral symmetry in the light quark sector. For this purpose, one can employ, e.g., the Nambu and Jona-Lasinio model [10]. Although it cannot be expected that the artificial NJL model will give us quantitatively reliable predictions, it can show us general trends, how the quark condensate will develop under different medium conditions.

The effective Lagrangian of the NJL model can be generally written as

$$\mathcal{L}_{NJL} = \bar{\Psi}(i\partial_\mu\gamma^\mu - \mathcal{M}^0)\Psi + \mathcal{L}_{int}^{(4)} + \mathcal{L}_{int}^{(6)}. \quad (2.4)$$

Here  $\mathcal{L}_{int}^{(4)}$  represents a local fermion current-current interaction invariant with respect to the global  $U(1)_V \otimes U(1)_A \otimes SU(3)_V \otimes SU(3)_A$  group of transformations and  $\mathcal{L}_{int}^{(6)}$  is a local six point fermion vertex, which breaks down the  $U(1)_A$  symmetry. Hence, the whole Lagrangian has the global  $U(1)_V \otimes SU(3)_V \otimes SU(3)_A$  symmetry only, the symmetry of QCD, see Section 2.2.

Equilibrium properties of a grand canonical system are determined using the partition function

$$\mathcal{Z} = \text{Tr} \exp(-\beta(H - \mu_i N_i)).$$

Here the parameter  $\beta$  is connected with temperature,  $\beta = (kT)^{-1}$ . In case of the NJL model,  $N_i$  are the numbers of valence quarks  $i = u, d, s$ , and  $\mu_i$  are the corresponding chemical potentials. The trace runs through all eigenstates of the NJL Hamiltonian  $H$ . The thermal average of any operator  $\mathcal{O}$  can be expressed as

$$\langle\langle \mathcal{O} \rangle\rangle = \mathcal{Z}^{-1} \text{Tr}(\mathcal{O} \exp(-\beta(H - \mu_i N_i))).$$

When applying the mean field approximation, the Lagrangian (2.4) of the NJL model is linearized and a quark propagator takes the form  $(\gamma_\nu p^\nu - m^0 - \Sigma)^{-1}$ , where  $p^\nu$  is the quark four-momentum,  $m^0$  is its current mass, and  $\Sigma$  stands for the self-energy. Contributions to the selfenergy originate from two sources. First, there is a dynamical mass shift  $\Delta m = m - m^0$  from the current mass  $m^0$  to the constituent mass  $m$  due to the interaction with the quark condensate. Second, the vector interaction causes a shift in the chemical potential  $\Delta\mu$ . Hence, the selfenergy equals

$$\Sigma = \Delta m + \gamma_0 \Delta\mu .$$

To the Lagrangian (2.4), one can find the corresponding Hamiltonian and then evaluate the partition function and the thermodynamic potential  $\Omega$ ,

$$\Omega = -\beta^{-1} \ln \mathcal{Z} .$$

Conditions on its minimum with respect to  $\Delta m$  and  $\Delta\mu$

$$\frac{\partial \Omega}{\partial(\Delta m)} = \frac{\partial \Omega}{\partial(\Delta\mu)} = 0$$

gave to the authors of the paper [10] a set of gap equations for the constituent quark masses. These equations form with the relations for thermal averages  $\ll \bar{q}q \gg$  and  $\ll q^+q \gg$ ,  $q = u, d, s$ , a system of self-consistent equations. The quark condensate as a function of temperature and density can be determined from this system of equations.

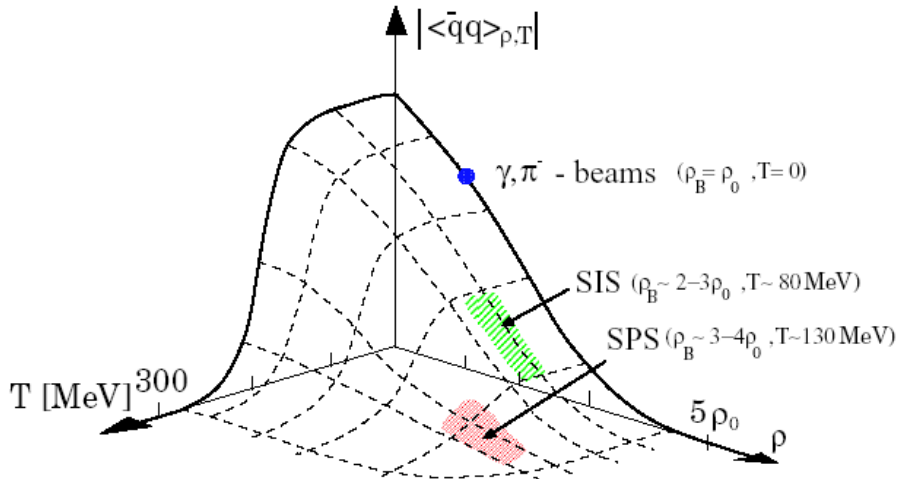


Figure 2.1.: Changes of the chiral condensate as a function of temperature ( $T$ ) and baryonic density ( $\rho$ ) [12]. Regions reachable at SIS and SPS are highlighted by colours. The normal nuclear density is denoted  $\rho_0$ ,  $\rho_0 = 0.16$  nucleon/ $\text{fm}^3$ .

Results of the NJL model calculations in finite temperature and density performed by Klimt et al. [12] can be seen in Figure 2.1. In the limit of the vanishing current quark masses, restoration of the chiral symmetry occurs when  $\ll \bar{q}q \gg = 0$ . At this point, the constituent quark masses turn out to be zero and we observe a sharp

phase boundary in the temperature-density plane. According to [10], the critical temperature at zero density should be in the interval 150–200 MeV and the critical density at zero temperature is expected to be 1.5–2 times the normal nuclear density. However, in nature, all quarks have their current mass non-zero. This breaks the chiral symmetry explicitly. The phase transition is still apparent in case of the quarks  $u$  and  $d$ . Nevertheless, now it is smooth and the sharp boundary disappears. For the much heavier strange quark, changes in density and temperature are flat without any phase transition.

The major reproach to the NJL model is that it does not include the confinement. At low temperatures and densities, eigenstates of the QCD Hamiltonian are not single quarks but hadrons. Therefore, in finite temperature regime, the quark condensate is frequently calculated from theoretical approaches based on the chiral meson theory, e.g., [13].

## 2.5. In-medium changes of the light vector mesons

It is thought that changes of the chiral condensate in hot and dense hadronic matter should have some impact on medium properties of the light vector mesons  $\rho$ ,  $\omega$ , and  $\phi$ . So far, theoretical approaches how to handle this problem are not unified. Current models employed to investigate medium properties of the light vector mesons can be roughly divided into two streams. The first one works with effective, purely mesonic Lagrangians and its predictions relate to the finite temperature region. The latter one takes into account baryonic fields and covers the realm of finite baryonic density. For more details concerning various model approaches see paper [5].

### 2.5.1. Effective meson Lagrangians

In paper [14], Pisarski studied finite temperature behaviour of the linear  $\sigma$ -model. This effective theory is attractive, because its Lagrangian can be rewritten in the way that it incorporates the chiral symmetry. The sigma meson is usually considered to be a very broad two pion resonance having the width of the same order as the mass. However, Pisarski suggested that in the limit of the chiral symmetry restoration, phase space for the two pion decay should reduce and the  $\sigma$  turns out to be a well-defined excitation. By means of thermal loop expansion to the lowest order in coupling constant  $g$ , Pisarski estimated finite temperature corrections to the selfenergy. At low temperatures and in the chiral limit, he obtained for the on-shell  $\rho$  and  $a_1$  masses

$$m_\rho^2(T) = m_\rho^2 - \frac{g^2\pi^2T^4}{45m_\rho^2} \left( \frac{4m_{a_1}^2(3m_\rho^2 + 4q^2)}{(m_{a_1}^2 - m_\rho^2)^2} - 3 \right) + \dots$$

$$m_{a_1}^2(T) = m_{a_1}^2 + \frac{g^2\pi^2T^4}{45m_\rho^2} \left( \frac{4m_{a_1}^2(3m_\rho^2 + 4q^2)}{(m_{a_1}^2 - m_\rho^2)^2} + \frac{2m_\rho^4}{m_{a_1}^2(m_{a_1}^2 - m_\sigma^2)} - \frac{m_{a_1}^2}{m_\rho^2} \right) + \dots$$

Here  $m_\rho$ ,  $m_{a_1}$ , and  $m_\sigma$  are the vacuum masses of  $\rho$ ,  $a_1$ , and  $\sigma$ , respectively,  $g$  denotes the coupling constant of the model,  $q$  is the four-momentum, and  $T$  stands for

temperature. Pisarsky examined also the critical temperature limit for the chiral symmetry restoration and he found out that masses of  $\rho$  and  $a_1$  should become degenerate. Shift in the  $\omega$  meson pole mass was only negligible.

Nevertheless, the broad width of the  $\sigma$  meson may invoke a question concerning the credibility of the low temperature limit of the previous model. Models based on massive Yang-Mills approach try to get rid of this drawback by eliminating the  $\sigma$  meson degree of freedom from the linear sigma model. A convenient way how to do this is to use a non-linear realization of the chiral symmetry [15]. Following this idea, Song [16] showed that with growing temperature,  $\rho$  meson mass increases whereas  $a_1$  meson mass decreases. However, the temperature dependencies were found to be weak.

Plenty of models concerning medium properties of the light vector mesons are based on phenomenological Lagrangians. These are constructed in the way to incorporate empirically important interactions and symmetries. Haglin [17] investigated scattering processes of on-shell vector mesons in a thermal bath consisting of pions and kaons. These pseudoscalar Goldstone bosons dominate to a thermal meson gas at medium and low temperatures. He found out that interaction with a thermal bath which has a temperature of  $T = 150$  MeV should cause broadening of the  $\rho$  meson width by approximately 40 MeV and by 30 MeV in case of the  $\omega$  meson. Broadening of the  $\phi$  meson was smaller. Haglin's work was further supplemented by Gao et al. [18] who changed the Haglin's Lagrangian to take into account isospin exchange interactions, they modified  $\pi\rho a_1$  vertex, and used different method for regularization of the singularity in the  $t$ -channel of the pion exchange diagram. They also incorporated broadening of the in medium decay width of  $\rho \rightarrow \pi\pi$  due to the pion Bose-Einstein enhancement factors. Gao learned that at  $T = 150$  MeV, broadening of the  $\rho$  meson should be substantially larger when compared to the previous results of Haglin. While scattering in pion gas increases the  $\rho$  meson width by 58 MeV, effect of the Bose-Einstein enhancement causes additional 25 MeV broadening.

### 2.5.2. Finite density

Brown and Rho [19] pointed out that if the current quark masses are omitted, the QCD Lagrangian (2.1) is scale invariant. The only energetic scale is given by means of the QCD scale  $\Lambda$ , see (2.2). Their conjecture states that hadron masses (except pion), pion decay constant, and the quark condensate should scale with  $\Lambda$ . This led them to a simple relation, which connects vacuum (in denominator) and medium (in numerator) masses of vector mesons and nucleons

$$\frac{f_\pi^*}{f_\pi} \simeq \frac{m_\rho^*}{m_\rho} \simeq \frac{m_\omega^*}{m_\omega} \simeq \frac{m_N^*}{m_N} \simeq \left( \frac{\langle \bar{\Psi}\Psi \rangle_\rho}{\langle \bar{\Psi}\Psi \rangle} \right)^\alpha.$$

There are several versions of the ‘‘Brown–Rho scaling’’ with different value of the exponent  $\alpha$ , e.g.,  $\alpha = 1/2$  or  $1/3$ . Even at the normal nuclear density, the ratio  $f_\pi^*/f_\pi$  should equal roughly to 0.8. The formula, thus, predicts quite a sizeable shift of vector meson pole masses already in usual cold nuclear matter. However, validity

of the ‘‘Brown–Rho scaling’’ in the finite temperature sector is rather controversial, see [5].

Based on the in-medium QCD sum rule analysis, Hatsuda and Lee [20] derived a simple formula, which estimates mass shifts of the non-strange light vector mesons in dense hadronic matter

$$\frac{m_{\omega,\rho}^*}{m_{\omega,\rho}} = 1 - (0.18 \pm 0.06) \frac{\rho}{\rho_0}, \quad (2.5)$$

where  $\rho_0$  is the normal nuclear density,  $\rho_0 = 0.16$  nucleon/fm<sup>3</sup>.

Other group of models tries to reflect changes in a pion cloud embedded to a nuclear environment. Nucleon-pion interaction in the P-wave can populate isobare-hole ( $\Delta N^{-1}$ ) or nucleon-hole ( $NN^{-1}$ ) states. Since the  $\rho$  meson can be viewed as a broad  $\pi\pi$  resonance, changes in the two-pion propagator will affect also the  $\rho$  meson self-energy. This should be manifested by broadening of the  $\rho$  meson width. The  $NN^{-1}$  and  $\Delta N^{-1}$  bubbles in the diagrammatic representation require to perform vertex corrections for  $\pi\pi\rho$  and  $\rho\rho\pi\pi$  couplings. This was done by Urban et al. [21]; besides of the  $\rho$  meson spectral function broadening, they found out an upward mass shift of the resonance.

In-medium vector meson spectral functions were evaluated also by Klingl et al. [22]. In their approach, the starting point was the  $SU(3)$  chiral Lagrangian for pseudoscalar mesons and baryons. In order to incorporate coupling between baryons and vector mesons, photon field was replaced by a term proportional to a combination of vector meson fields. Klingl et al. have shown that density effects should influence especially the spectral functions of the  $\rho$  and  $\omega$  mesons, which exhibited substantial broadening with increasing nuclear density. Further, dense medium caused a decline of the  $\omega$  meson pole mass. However, the spectral function of the  $\phi$  meson turned out to be practically unchanged.

Surrounding nuclear medium may also enhance the number of processes, where  $\rho$  meson directly couples to nucleons forming a resonance-hole states. Adding these vertices to an interaction Lagrangian changes the in-medium selfenergy and the spectral function of the  $\rho$  meson. Peters et al. [23] considered in their model nine baryonic states N(939),  $\Delta(1232)$ , N(1440), N(1520),  $\Delta(1620)$ ,  $\Delta(1700)$ , N(1720),  $\Delta(1905)$ , and N(2000). He showed that phase space for  $N(1520) \rightarrow N + \rho$  decay enhances due to the appearing of a low energy strength in the broaden in-medium  $\rho$  spectral function. Consequently, the decay width of N(1520) should substantially enlarge in dense medium.

## 2.6. Spectroscopy of the light vector mesons in medium

In Section 1.1, we discussed why di-leptons have the potential to give us answers on the frequently asked questions: Does the surrounding nuclear medium change properties of the light vector mesons? If yes, which theoretical scenario is realized in nature? Within a few last decades, the in-medium spectroscopy of the light vector

mesons was extensively experimentally investigated. Recent review on experiments examining di-leptons emerging from hot and dense hadronic matter was given, e.g., by Tserruya [24].

Different experiments probe properties of the light vector mesons at different conditions. According to density which is reached in a reaction, experiments can be divided roughly into four groups. Experiments investigating the mesons in

1. normal nuclear matter ( $\rho_0 = 0.16$  nucleon/fm<sup>3</sup>),
2. nuclear densities 2–3  $\rho_0$ ,
3. nuclear densities 3–4  $\rho_0$ , and
4. high energy densities.

The next four sections are devoted to a review on experiments pursuing each of these regions.

## 2.7. Nuclear densities close to $\rho_0$

The experiment E325 at KEK-PS was searching for di-electron signal coming out of p+C and p+Cu reactions at 12 GeV [25, 26]. Such reaction do neither heat nor compress nuclear matter too much. Produced vector mesons may thus decay outside or inside the cold nuclear medium, which can be considered have the normal nuclear density. Further, the E325 collaboration was searching for kaons originating from the decay  $\phi \rightarrow K^+K^-$ . The OZI rule qualitatively explains why the two kaon decay channel of the  $\phi$  meson is enhanced when compared to its three pion decay, although the phase space for the latter process is much larger. However, only a small shift of the  $\phi$  meson mass in nuclear medium would cause substantial changes of the branching ratio for the two kaon decay. If the  $\phi$  meson mass decreases in medium one would then observe suppressed production of the kaon pairs. The E325 spectrometer is described in detail in [27]. It has an excellent mass resolution, which is slightly better than 1 % at the  $\phi$  pole mass.

In Figure 2.2, we may find the E325 results on di-electron production in p+Cu at 12 GeV. In the left-hand side plot, an invariant mass spectrum of  $e^+e^-$  pairs is shown. The grey line represents a sum of contributions from known hadronic sources and combinatorial background. Notice that there is a visible excess in the pair yield in the region close to the lower edge of the omega peak. In the right-hand side figure, the same data after combinatorial background subtraction are shown. Now, the grey line represents a fit of the data with a prediction of Toy model. This simple model supposes that in-medium modifications of the light vector meson masses follow the Hatsuda and Lee dropping mass scenario discussed in Section 2.5.2,

$$\frac{m_{\omega,\rho}^*}{m_{\omega,\rho}} = 1 - 0.16 \frac{\rho}{\rho_0}. \quad (2.6)$$

Further, the model presumes uniform production of the mesons  $\rho$  and  $\omega$  at the surface of the incident hemisphere of each nucleus. Vector mesons emerge having their

## 2. State of the art

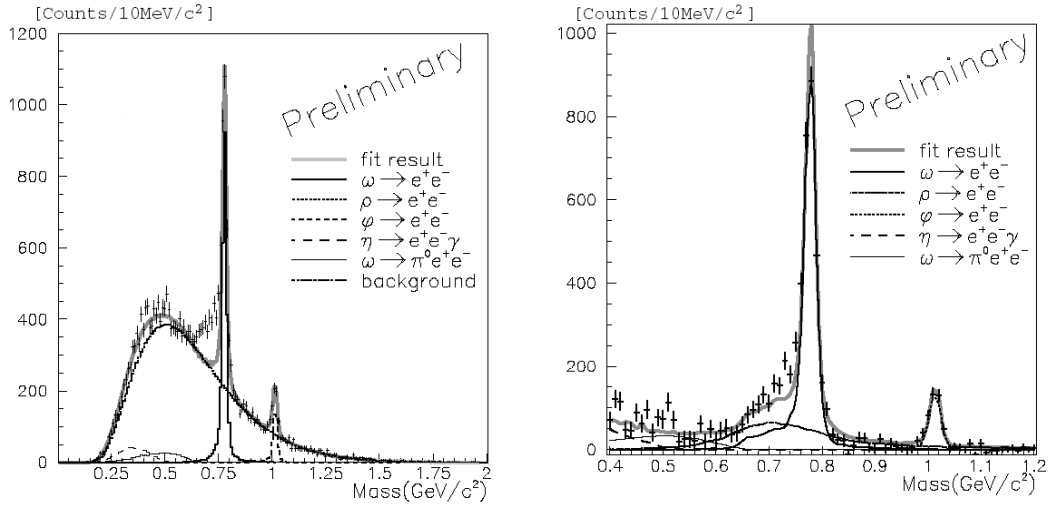


Figure 2.2.: Invariant mass spectra of di-electrons as measured by the KEK-PS E325 collaboration in p+Cu reactions at 12 GeV [26]. **Left:** Invariant mass spectrum of  $e^+e^-$  pairs. **Right:** Data after combinatorial background subtraction. See the text for comments to both plots.

vacuum mass. Their 3-momentum distribution is calculated by the nuclear cascade code JAM. At the decay point, masses of vector meson are modified according to the local density and Equation (2.6). The experiment E325 found a good agreement between the Toy model and the measured data. Nevertheless, it is necessary to take the results of the E325 experiment with a great caution. The main reproaches to the data interpretation are the following: combinatorial background was estimated from the mixed event technique. This can be a problem as it is known that a mixed event background describes wrongly the correlated background coming from  $\pi^0$ ,  $\eta$ , and  $\omega$  decays. The E325 collaboration should check if the shape of their background is correct. Further, the like-sign same-event technique (see Section 7.2) was not used for the normalization of the mixed event background. The mixed event background was only scaled to fit the data. Use of global fits is dangerous, since they prefer those parts of spectrum where is a good statistics of counts. This can easily smear a broad signal such as the  $\rho^0$  contribution. Thus the  $\rho^0$  contribution to the invariant mass spectrum is probably determined incorrectly. The E325 collaboration did not clearly prove that the observed broadening of the omega peak towards lower invariant masses is not connected to some unexpected behaviour of their spectrometer. It can be anticipated that this broadening should be absent in p+p or p+d collisions. To increase credibility of the obtained results these systems should be studied also using the same set-up.

Some experimental facilities study vector mesons emerging in reactions  $\gamma+A$ . This reaction is somewhat simpler when compared to A+A collision which has complicated dynamics and which provides only results integrated over a whole range of density and temperature.

One of these experiments is called CLAS (*CEBAF Large Acceptance Spectrometer*) [28]. It is situated at the Jefferson Laboratory. The CLAS detector is used to study

photo- and electro-induced nuclear and hadronic reactions. Tagged-bremsstrahlung photon beams are prepared using *Continuous Electron Beam Accelerator Facility* (CEBAF). The CLAS collaboration presented some preliminary  $e^+e^-$  invariant mass spectra from  $\gamma+A$  reactions during the Meson 2008 conference in Cracow [29]. They are sensitive to the  $\rho^0$  mesons which have their momentum between 0.8–2 GeV in medium. The collaboration claims that their fit of the in-medium  $\rho^0$  meson spectral function is compatible with no mass shift. The spectral function exhibited broadening consistent with many-body effects.

A large reduction of the  $\rho^0$  vector meson mass in the nuclear medium was reported by the TAGX collaboration [30]. They pursued di-pion photo-production in the reaction  $\gamma+{}^3\text{He}\rightarrow\pi^+\pi^-+X$ . Tagged photons had energies  $800\leq E_\gamma\leq 1120$  MeV. Hence,  $\rho^0$  mesons emerged mostly below the free production threshold. This region is believed to be sensitive to modifications of properties of the light vector mesons at nuclear-matter densities. Masses of the  $\rho^0$  were reconstructed for three  $E_\gamma$  intervals, see Table 2.1. TAGX observed decrease of the pole mass of the  $\rho^0$ , nevertheless, it is questionable whether this behaviour cannot be caused by the final state interaction of the produced pions.

$E_\gamma$ [MeV]	800–880	880–960	960–1040
$m_{\rho^0}^*$ [MeV]	$642\pm 40$	$669\pm 32$	$682\pm 56$

Table 2.1.: In-medium masses ( $m_{\rho^0}^*$ ) of the  $\rho^0$  meson for three photon energy ( $E_\gamma$ ) intervals. Data are taken from the TAGX experiment [30].

The Crystal Barrel/TAPS experiment at the ELSA tagged photon facility in Bonn investigated the photo-production of the  $\omega$  mesons on nuclei. Possible in-medium modifications were studied in reactions  $\gamma+A\rightarrow\omega+X\rightarrow\pi^0\gamma+X'$ . The decay channel  $\omega\rightarrow\pi^0\gamma$  is favourable, because its branching ratio is about 9 %. This is three orders of magnitude higher than in the case of  $\omega\rightarrow e^+e^-$  decay and two orders of magnitude higher than the branching ratio for  $\rho^0\rightarrow\pi^0\gamma$ . Contributions from  $\rho^0$  decays to the invariant mass spectrum of  $\pi^0\gamma$  are thus suppressed. A problem may arise only from the final state interaction of  $\pi^0$ , which may couple to nucleons producing an intermediate  $\Delta$  resonance. However, the Crystal Barrel/TAPS collaboration claims that in the invariant mass range  $0.6\text{ GeV}\leq M_{\pi^0\gamma}\leq 0.9\text{ GeV}$ , only 3 % of all events were influenced by the neutral pion final state interaction. The Crystal Barrel/TAPS experiment measured  $\omega$  production on Nb nuclei and also on a reference liquid hydrogen target [31]. They found a significant enhancement of a yield at lower invariant masses for  $\omega$  mesons produced on the Nb target when compared to the yield from the liquid hydrogen target, see Figure 2.3. Further, the experiment observed that this mass shift occurs only for the omegas with momentum lower than cca 500 MeV, which due to their low velocity decayed with increased probability already inside the nucleus. The assessed in-medium  $\omega$  meson mass at an estimated average nuclear density of  $0.6\rho_0$  was  $m_\omega^*=[722_{-4}^{+4}(\text{stat})_{-5}^{+35}(\text{syst})]\text{ MeV}$ .

Consistency with the Hatsuda–Lee like scaling [20]

$$\frac{m_\omega^*}{m_\omega} = 1 - 0.14 \frac{\rho}{\rho_0}, \quad (2.7)$$

was found. The invariant masses of the long-living mesons  $\pi^0$ ,  $\eta$ , and  $\eta'$ , which decay outside of the nucleus, were also reconstructed. In this case, no difference in the line shape for the two data samples was observed.

However, this promising signal of the “in-medium”  $\omega$  modification is probably not real. As it was pointed by professor Metag in his speech at the 20th Indian Summer School in Řež, the recent reanalysis of the data from this experiment does not confirm the mass shift of the  $\omega$  meson [32]. The observed in-medium effect was probably caused by an incorrect shape of the combinatorial background.

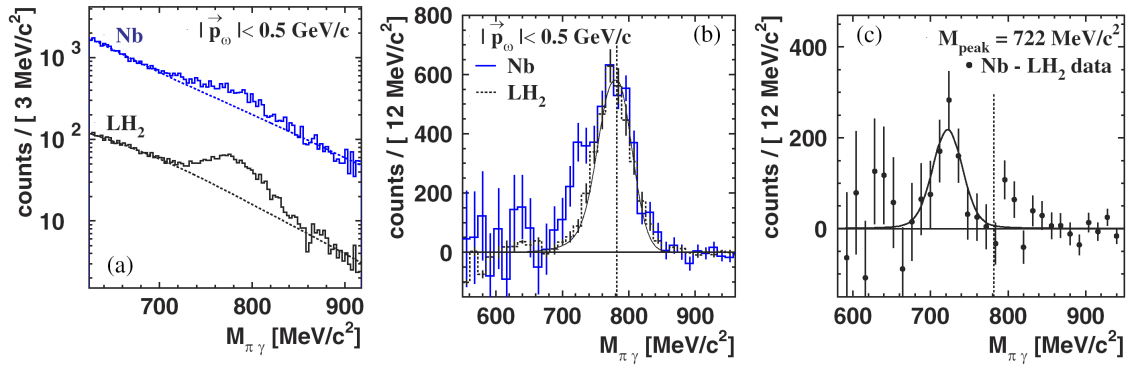


Figure 2.3.: **Left:** Inclusive  $\pi^0\gamma$  invariant mass spectra for the  $\omega$  mesons with momenta below 500 MeV. The upper histogram shows  $\gamma$ +Nb data, the lower histogram depicts liquid hydrogen target reference measurement. The dashed lines indicate fits to the respective background. **Middle:**  $\pi^0\gamma$  invariant mass spectrum from the  $\gamma$ +Nb (solid histogram) and  $\gamma$ +p (dashed histogram) measurement after background subtraction. The error bars show statistical uncertainties only. **Right:** In-medium decays of  $\omega$  mesons along with the Voigt fit (Breit–Wigner folded with Gaussian) to the data. The vertical line indicates the vacuum  $\omega$  pole mass (782 MeV). Figure was taken from [31].

## 2.8. Nuclear densities up to 2–3 $\rho_0$

The *Dilepton Spectrometer* (DLS) [33, 34] measured  $e^+e^-$  pairs emerging in elementary nucleon-nucleon reactions as well as in collisions of heavier A+A systems. The Bevalac accelerator provided heavy ion beams with kinetic energies of 1–2 A GeV. The DLS two arm spectrometer is described in [35]. Let us only point out that the spectrometer had two significant drawbacks: a small geometrical acceptance and a poor resolution in invariant mass (only  $\sigma_{M_{ee}}/M_{ee} \simeq 10\%$ ).

Unfortunately, the first generation DLS data were corrupted by a trigger inefficiency. Hence, only the second generation data can be compared with model predictions. This was done by Bratkovskaya et al. in papers [36, 4, 37]. It turned out

to be a problem to reproduce the DLS A+A data satisfactorily. In Figure 2.4, the DLS invariant mass spectrum of  $e^+e^-$  pairs from Ca+Ca collisions at 1 A GeV is contrasted to a prediction of the transport code HSD (*Hadron String Dynamics*), for more details see [4]. First, Bratkovskaya et al. assumed that the  $\rho^0$  meson has in nuclear medium the same spectral function as in the vacuum. However, this led to large discrepancies between the experimental data points and the HSD predictions. Especially in the invariant mass region  $0.2 \leq M_{ee} \leq 0.6$  GeV, the measured  $e^+e^-$  yields were underestimated by factor 3–5. Agreement between the HSD cocktail and the DLS data slightly improved when Bratkovskaya et al. took into account changes of the  $\rho^0$  meson spectral function due to its in-medium coupling, see the right-hand side plot in Figure 2.4. Further, it was shown that the remaining excess in the region 0.2–0.4 GeV could be explained if one would adopt for the  $\eta$  meson the in-medium Hatsuda and Lee like dropping mass scenario [20]. Such behaviour of the  $\eta$  mass would, however, violate the  $m_\perp$  scaling, which was observed by the TAPS collaboration [78, 79]. Interpretation of the heavy ion DLS data was thus a puzzle.

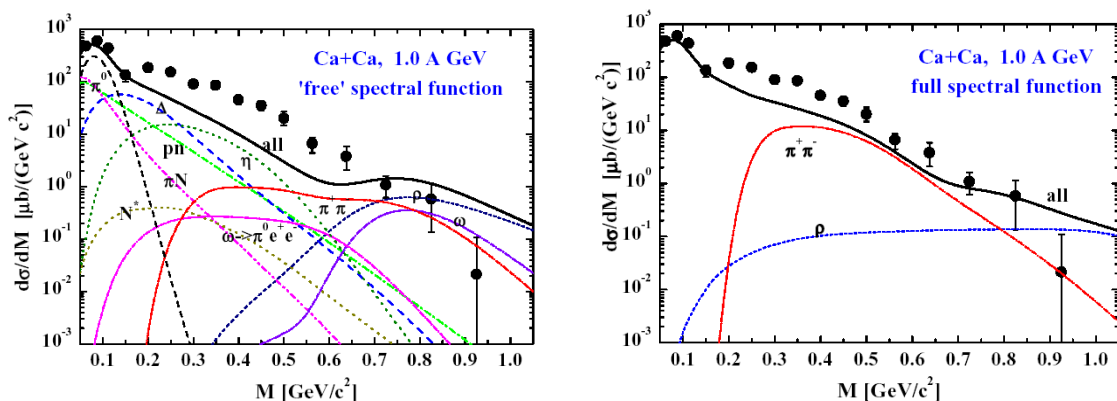


Figure 2.4.: Invariant mass spectra of  $e^+e^-$  pairs as measured by the DLS collaboration in Ca+Ca reactions at 1 A GeV [4]. **Left:** The DLS data are compared with the HSD prediction (full-black line) which assumed that the spectral function of the  $\rho^0$  meson has the “vacuum” shape. **Right:** In-medium broadening of the  $\rho^0$  meson spectral function is taken into account using the model [23]. Colour lines show the contributions of  $\pi^+\pi^- \rightarrow \rho^0 \rightarrow e^+e^-$  and  $\rho^0 \rightarrow e^+e^-$ .

The observed disagreement between transport code predictions and the DLS nucleus-nucleus data was one of the incentives to build a new experiment called *High Acceptance Di-Electron Spectrometer* (HADES) [6, 7], which would examine  $e^+e^-$  pair production in the same energy region of nuclear collisions as DLS. The HADES spectrometer is situated at GSI Darmstadt. It should be capable to measure pair yields in heavy ion reactions up to 8 A GeV Au+Au collisions. The collaboration, further, wants to study  $e^+e^-$  production in elementary processes such as p+p, p+n,  $\pi$ +p, and reactions p+A or  $\pi$ +A. Data taking started in 2001. So far, emission of pairs was measured in the experiments p+p at 1.25, 2.2, and 3.5 GeV and in d+p at 1.25 A GeV. The collaboration had also three runs with heavier systems, C+C

## 2. State of the art

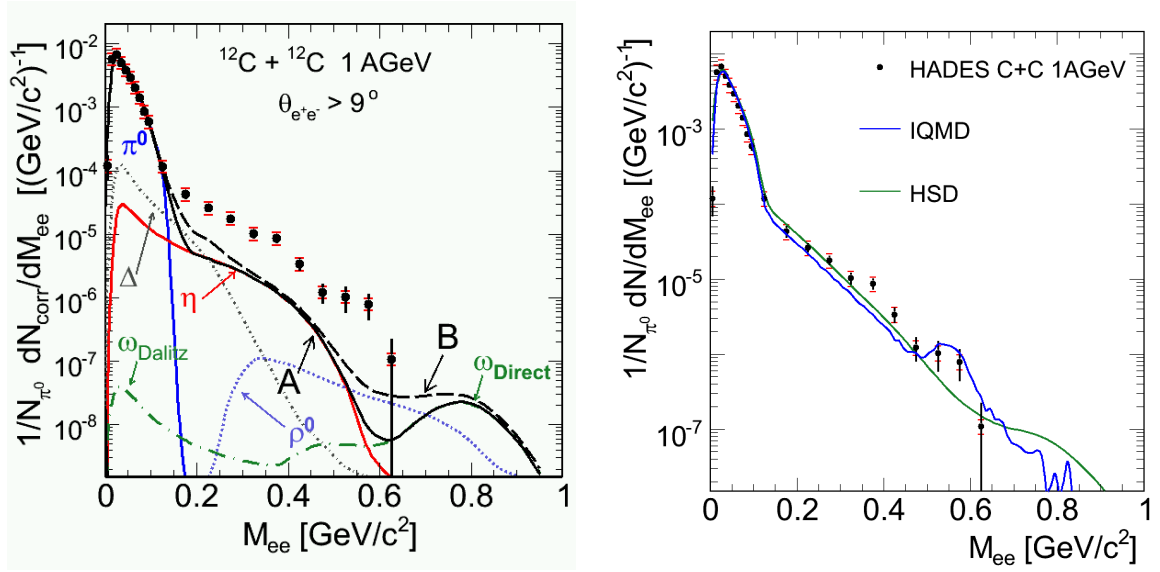


Figure 2.5.: Inclusive invariant mass spectrum of  $e^+e^-$  pairs from  $^{12}\text{C}+^{12}\text{C}$  collisions at 1 A GeV as measured by the HADES collaboration [38]. **Left:** Experimental di-electron yields are compared with the sum of hadronic sources produced by the event generator Pluto [66]. Spectral functions of the light vector mesons are assumed to be the same as in the vacuum. **Right:** The experimental data are compared with predictions of two transport codes, HSD and IQMD.

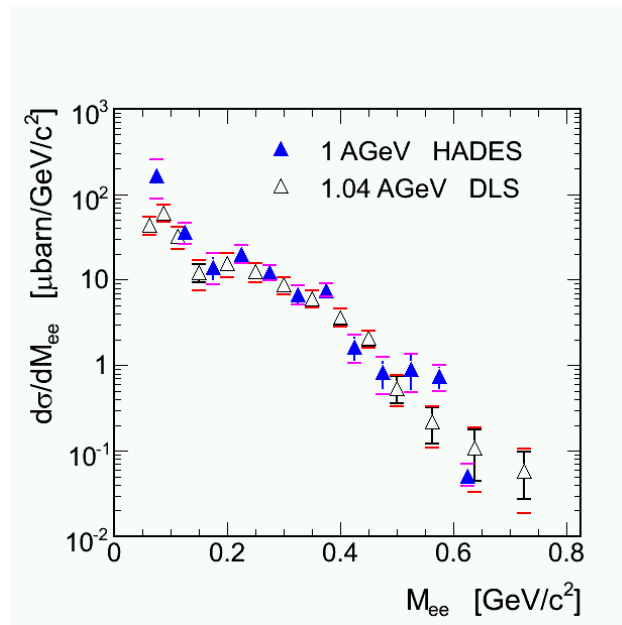


Figure 2.6.: Comparison between the HADES and the DLS pair invariant mass spectrum from C+C at 1 A GeV collisions [38]. The HADES data points were extrapolated into the geometrical acceptance of the DLS spectrometer.

at 1 and 2 A GeV and Ar+KCl at 1.756 A GeV. Analysis of all these data is not finished yet.

The final results on  $e^+e^-$  pair production in C+C at 1 A GeV are shown in Figure 2.5. In the left-hand side plot, the HADES data points are compared with predictions of our thermal model based Monte Carlo event generator Pluto [66]. The simulated cocktail shows the expected di-electron yield from  $\pi^0$ ,  $\eta$ ,  $\omega$ ,  $\Delta$ , and  $\rho^0$  based on their known production and decay rates. Pluto does not provide satisfactory description of the measured yield and we may see large discrepancies in the invariant mass region  $0.2 \leq M_{ee} \leq 0.6$  GeV. On the other hand, the same data points are well reproduced if we use the cocktail generated with the more sophisticated transport codes like HSD [80] or IQMD [40], which involve wider spectrum of baryonic resonances and reaction processes. In case of the C+C 1 A GeV data, the HADES measurement corroborates results of the DLS collaboration, see Figure 2.6.

## 2.9. Nuclear densities up to 3–4 $\rho_0$

The CERES/NA45 collaboration at CERN SPS studied di-electron production in nuclear reactions ranging with their kinetic beam energies from 40 up to 200 A GeV. The CERES apparatus is described in [8, 42].

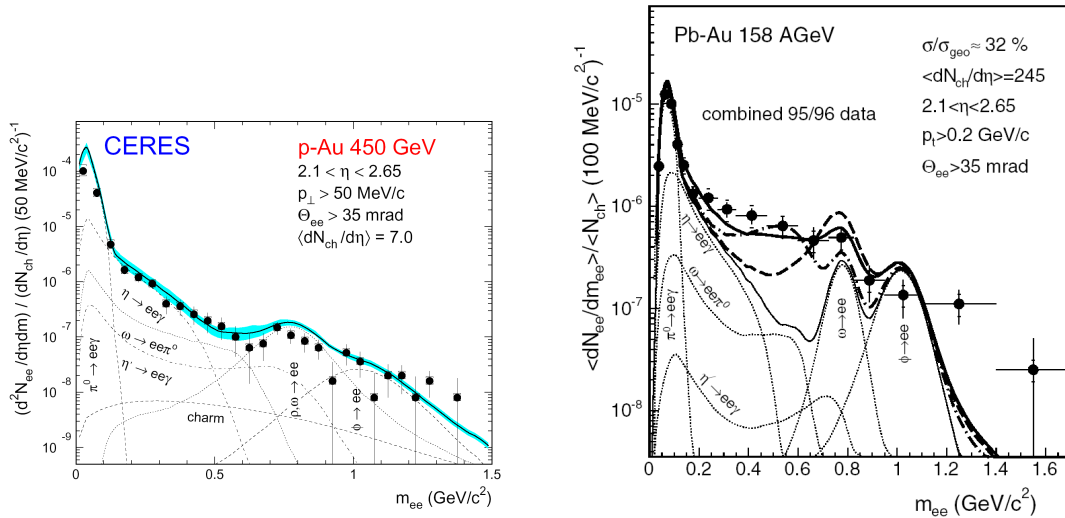


Figure 2.7.: Invariant mass spectra of di-electrons measured by the CERES collaboration. **Left:** p+Au at 450 GeV [43]. **Right:** Pb+Au at 158 A GeV [41]. For comments to both figures see the text.

CERES showed that its di-electron yield from p+A reactions can be satisfactorily reproduced with a cocktail based on measured hadron multiplicities and decay rates, see the left-hand side plot in Figure 2.7. However, such a cocktail of expected hadron decays could not reproduce the data from the heavier Pb+Au at 158 A GeV system, see the thin solid line in the right-hand side plot in Figure 2.7. The Pb+Au data are compared also with predictions of two models. The first one assumes that in

## 2. State of the art

medium, the light vector mesons follow dropping mass scenario (dash-dotted line) and the second model takes into account in-medium broadening of the vector meson widths (thick solid line), for more details see [41]. Note that both models describe the data equally well. Thus, it is natural to ask, how it can be distinguished, which of these scenarios is realized in nature. It seems to that largest differences between these two models are in the region between the  $\omega$  and the  $\phi$  pole masses. Because the CERES experiment is nearly finished, a careful scan of this region is up to the NA60 experiment.

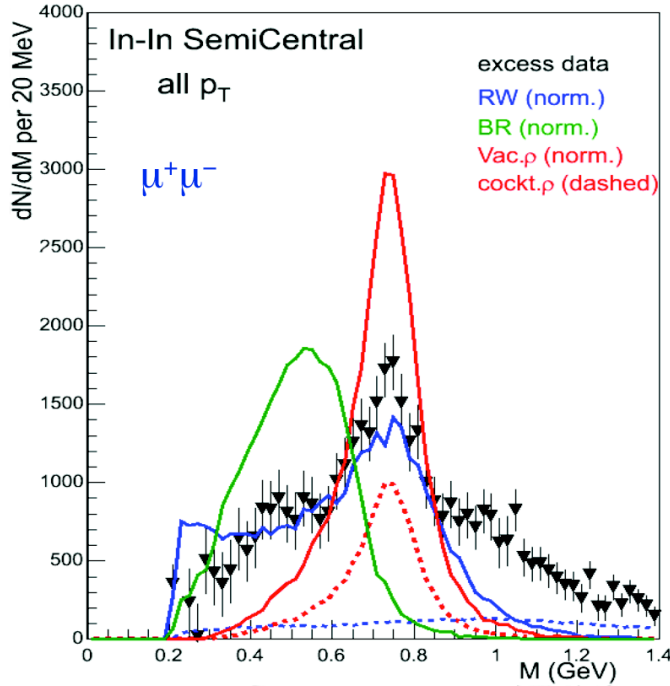


Figure 2.8.: Di-muon invariant mass spectrum of the  $\rho^0$  component in the semi-central In+In collisions at 158 A GeV as measured by the NA60 collaboration [55]. Experimental points are compared with predictions of the model which assumes the “Brown–Rho scaling” (BR, green solid line) and the calculation of Rapp–Wambach (RW, blue solid line) which incorporated in-medium broadening of the  $\rho^0$  meson width. Further, the plot shows the expected shape of the  $\rho^0$  meson based on its vacuum properties (vac.  $\rho$ , solid red line).

Research program of the NA60 collaboration at CERN is aimed at study of low and intermediate mass di-muon production and examining the  $J/\psi$  production and suppression in nuclear collisions. Thus, it continues and further extends the work of the precursor NA38 [51] and NA50 [52] experiments. The NA60 spectrometer has an excellent mass resolution of around 20 MeV at the  $\omega$  meson pole mass. In 2003, the NA60 collaboration measured In+In collisions at a kinetic beam energy of 158 A GeV [44]. Results from this run were presented during the Quark Matter 2005 conference. In Figure 2.8, we may see one of the figures that especially attracted the attention of physical community. It shows a comparison of the  $\rho^0$  meson component, extracted from the measured di-muon invariant mass spectrum [46], with predictions of several theoretical models. During the conference, it was claimed that this figure completely

rules out the conjecture of “Brown–Rho scaling”. However, in the subsequent papers [53, 54], Brown and Rho objected that the model which was used to predict the “Brown–Rho scaling” like behaviour of vector meson masses in Figure 2.8 is not what they think the “Brown–Rho scaling” is. So, the situation is not resolved yet. The data from the In+In run further suggest that the  $\rho^0$  meson spectral function gets broader with increasing centrality of the collision [45]. In addition, no shift in the  $\rho^0$  pole mass was observed.

To end up this section, let us also mention results of the HELIOS-3 [47, 50] collaboration. At CERN SPS, they studied di-muons in p+A and A+A collisions from the production threshold up to  $J/\psi$ . In congruence with the CERES results, HELIOS-3 observed enhancement of  $\mu^+\mu^-$  yields in S+W collisions at 200 A GeV in the invariant mass region 0.2–0.6 GeV when compared to di-muon signal obtained in p+A measurement. The experimental pair yield from the S+W run could be reproduced only when in-medium changes of the light vector meson properties were assumed.

## 2.10. High energy densities at RHIC

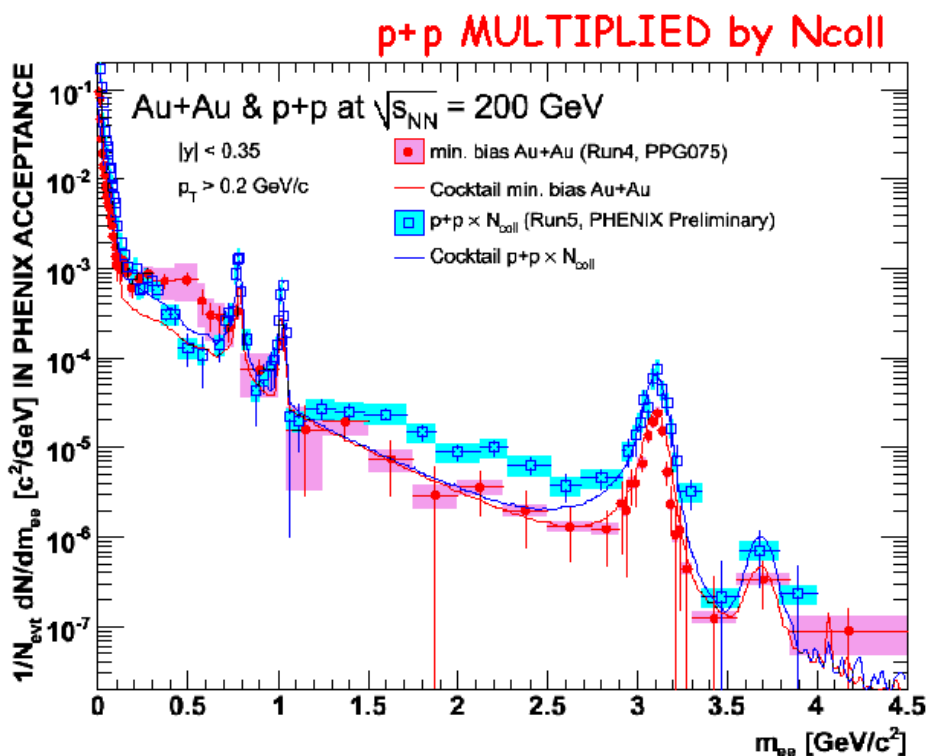


Figure 2.9.: Invariant mass spectrum of  $e^+e^-$  pairs from Au+Au and p+p collisions at  $\sqrt{s} = 200$  A GeV as measured by the PHENIX collaboration [59].

Towards to the higher and higher energies of A+A collision, quark and gluon degrees of freedom start to play an important role. In the very early stage of a heavy

ion reaction at RHIC ( $\sqrt{s} = 200 A$  GeV), collisions between nucleons proceed on the partonic level. High energy di-leptons are produced, e.g., in annihilation of D-mesons, the Drell-Yan process,  $\Upsilon$  decay, etc. The experiment PHENIX [56, 57] at RHIC is exploring a completely new region of di-lepton production. In a central Au+Au collision, energy densities reach at least  $15 \text{ GeV}/\text{fm}^3$  [58]. Nevertheless, the density of baryonic matter is assumed to be low.

Recently, PHENIX reported new data on  $e^+e^-$  pair production from Au+Au at  $\sqrt{s} = 200 A$  GeV [59]. In Figure 2.9, the inclusive invariant mass spectrum of  $e^+e^-$  pairs from this run is compared with the results of the p+p measurement taken at the same collision energy per nucleon. The p+p data are scaled up by the mean number of nucleon-nucleon interactions that occur in one Au+Au collision. From our point of view, it is interesting that the invariant mass spectrum of  $e^+e^-$  pairs from the nucleus-nucleus system shows an enhancement with respect to the p+p data in the region below the  $\omega$  peak.

PHENIX analysis has to face several challenges. The number of produced charged hadrons is several orders of magnitude larger than the multiplicity of created leptons. Further, majority of the observed leptons originates from trivial sources such as  $\pi^0$  decay or  $\gamma$  conversion. Hence, PHENIX suffers from a rather small signal to background ratio and has to fight with a large combinatorial background.

## 3 HADES spectrometer

It is believed that spectroscopy of the light vector mesons, based on their electromagnetic decay channel, has a capability to reveal us slight changes in their properties caused by the surrounding nuclear medium. However, in order to be sensitive to such a fine phenomenon, we have to employ an effective detection system. The *High Acceptance Di-Electron Spectrometer* (HADES) was designed to measure di-electron pairs which are produced in heavy ion collisions (1–2 A GeV) and elementary particle reactions. The HADES spectrometer covers the polar angle between 18–85 deg and almost the full azimuthal angle. It was designed to possess a large acceptance for pair detection. Based on the Monte Carlo simulations, it was shown [62] that the geometry of the spectrometer ensures nearly flat di-electron acceptance (about 30 % for pairs with invariant mass  $M < 1.5$  GeV and transverse momentum  $p_T < 1.5$  GeV). The spectrometer has a hexagonal symmetry with a beam line running through its axis, see Figure 3.1. Since HADES is a fixed target experiment, all detection systems are placed in the forward angle region, see Figure 3.2. Leptons are identified by means of the Cherenkov radiation, time of flight measurements, and electromagnetic shower detection. In order to reduce multiple scattering of emitted electrons, all tracking detectors and the shell and the mirrors of the Ring Imaging Cherenkov detector are made of low  $Z$  materials.

The following sections are devoted to a brief description of all HADES sub-detectors. The spectrometer is described in more detail elsewhere, e.g., in [60, 61].

### 3.1. RICH

The spectrometer is equipped with a “hadron blind” Ring Imaging Cherenkov detector (RICH). It enables us an efficient selection of events in which leptons arise. RICH is used as a threshold detector. It registers only charged particles<sup>1</sup> which have  $\gamma > 18.3$ . This corresponds to velocities  $\beta > 0.9985$ .

The RICH radiator encloses the target in the whole forward hemisphere. The radiator is filled with  $C_4F_{10}$  gas with a refractive index of  $n = 1.00151$ . This gas is transparent for the light down to the wave length  $\lambda = 145$  nm and does not show any significant scintillation from charged particles. The number of produced Cherenkov photons depends on a path length travelled by a lepton in the radiator. This distance can vary from 36 cm to 65 cm.

Cherenkov light is in all azimuthal angles reflected and focused on a photon detector by means of a spherical mirror. An electron circle has approximately a constant diameter of 5 cm. The mirror has a radius of curvature of 871 mm and a diameter of 1.5 m. It is divided into six sectors each composed of three panels made of pure carbon. They are machined to a thickness 2 mm, polished, and coated with thin Al and  $MgF_2$  layers.

---

<sup>1</sup>The threshold condition is fulfilled already for  $e^{+-}$  with an energy of 9.35 MeV. The threshold energies for heavier particles are higher, 1934 MeV in case of  $\mu^{+-}$  and 2555 MeV for  $\pi^{+-}$ .

### 3. HADES spectrometer

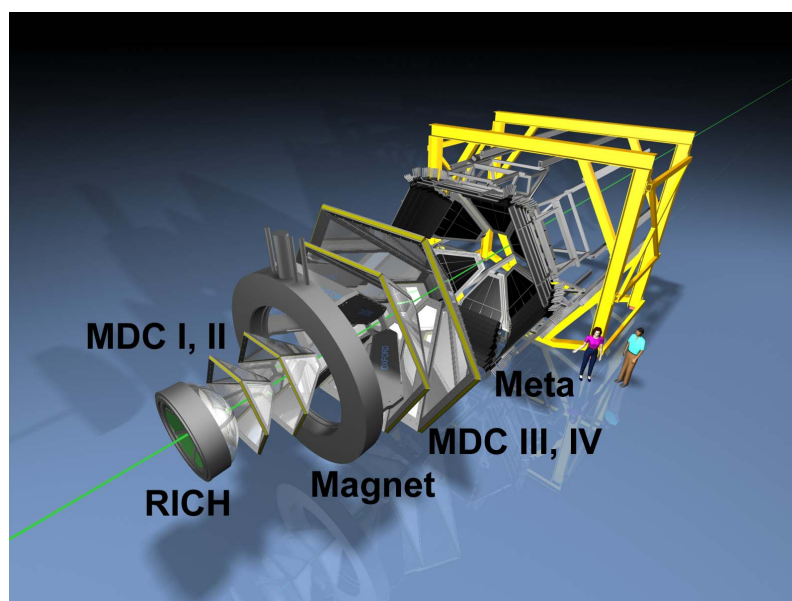


Figure 3.1.: Disassembled HADES spectrometer. The spectrometer has a toroidal geometry with 6 sectors arranged symmetrically around the beam line (green line). If a reaction occurs in the target a part of its products flies through the threshold Cherenkov detector RICH. Then they pass through the tracking system, formed by 2+2 layers of the drift chambers (MDC I, II and MDC III, IV) with a superconducting magnet in between. Finally, particles produce a signal in the system of the so-called Meta detectors. This system consists of the detectors measuring time of flight (TOF positioned at larger polar angles and TOFino situated at smaller polar angles) and electromagnetic showers. The last mentioned detector is called Shower and it is placed behind TOFino.

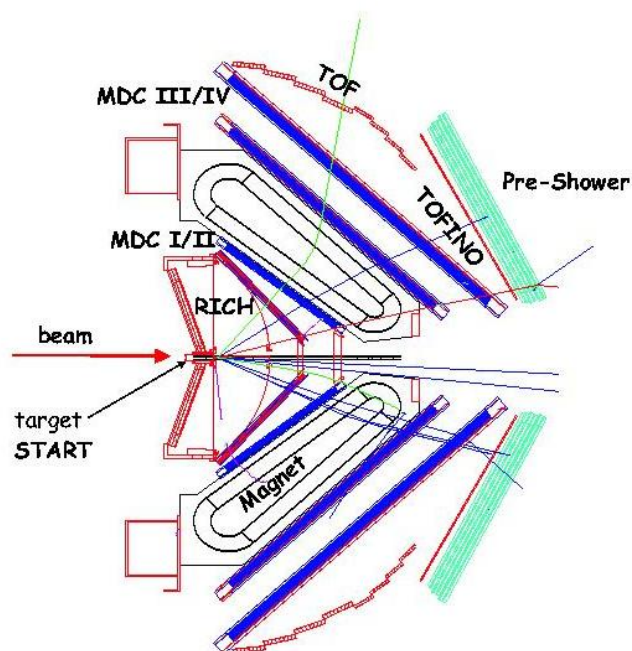


Figure 3.2.: Cross section through the HADES spectrometer.

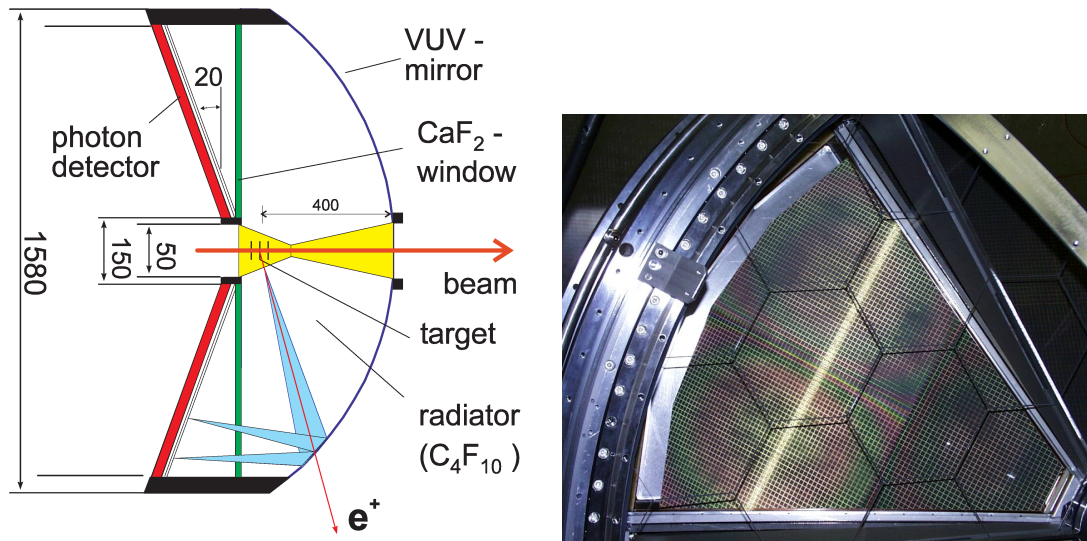


Figure 3.3.: **Left:** Side cross section of the RICH detector. **Right:** Wires of the photon detector viewed through the entrance window of CaF<sub>2</sub> crystals.

After reflecting off the mirror, Cherenkov photons enter the photon detector through a CaF<sub>2</sub> entrance window. The photon detector consists of six multi-wire proportional chambers with 3 wire layers and a cathode pad readout. The detector gas is methane. In a solid CsI photo-cathode evaporated onto pads, Cherenkov photons are converted into photo-electrons which are then registered in the multi-wire proportional chambers.

## 3.2. Tracking system

The tracking system of the HADES spectrometer consists of two sets (each set has two layers) of Multiwire Drift Chambers (MDC) placed in front of and behind a superconducting toroidal magnet. The achieved accuracy of momentum reconstruction is about  $\sigma_p/p = 1.5\text{--}2\%$ . The total detector thickness per one chamber in the units of a radiation length is below  $5 \times 10^{-4}$ .

### 3.2.1. MDC

Each drift chamber layer composes of six trapezoidal modules. One module covers 60 degrees of azimuthal angle. Module sizes (height times larger baseline) range from 88 cm  $\times$  80 cm in the plane I to 280 cm  $\times$  230 cm in the plane IV. In order to achieve a constant granularity in all MDC layers, drift cell sizes vary from 5 $\times$ 5 mm<sup>2</sup> (plane I) up to 14 $\times$ 10 mm<sup>2</sup> (plane IV). The total number of the drift cells is about 27000. Space resolution reached by the MDCs is cca 150  $\mu$ m. An inclination of each MDC module was chosen in such a way that trajectories of particles emitted from the target are more or less perpendicular to its surface. Each MDC module is composed out of six drift cell layers. Anode wires are oriented  $-40$  deg,  $+20$  deg,

### 3. HADES spectrometer

0 deg, 0 deg,  $-20$  deg , and  $+40$  deg, with respect to the module baseline margin. Wires in the six cathode planes are all perpendicular to this margin, see Figure 3.4.

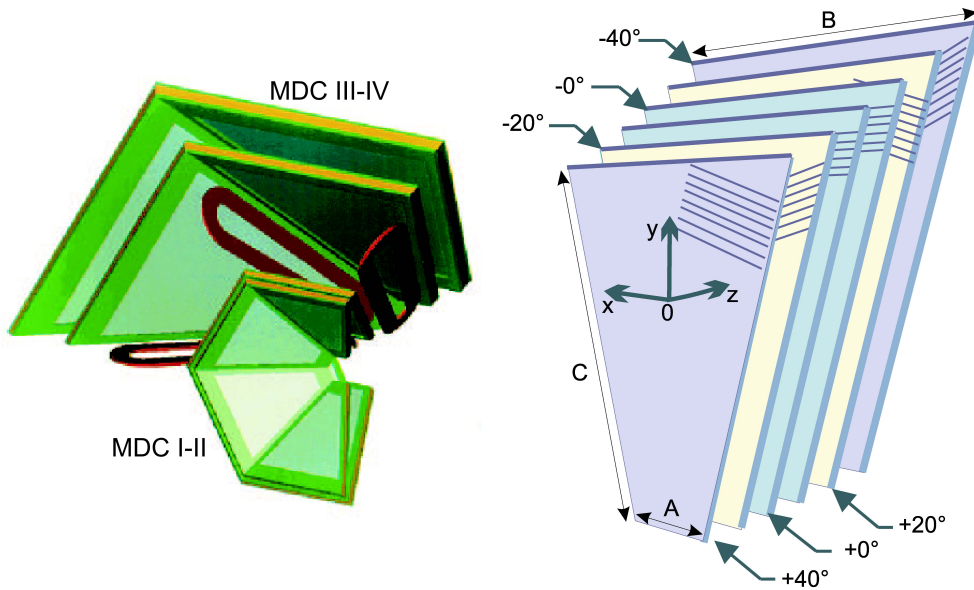


Figure 3.4.: Multiwire Drift Chambers.

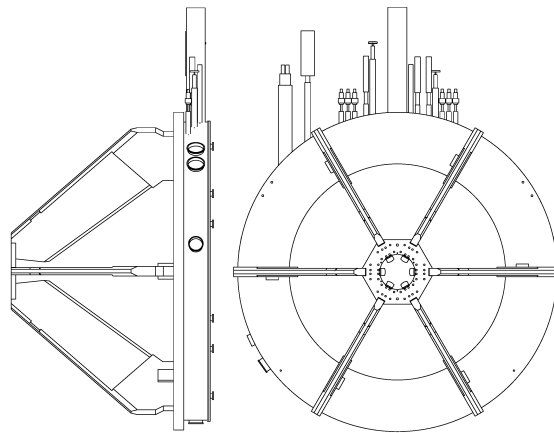


Figure 3.5.: Coils of the magnet. The support ring has the outer diameter of 3.56 m.

#### 3.2.2. Magnet

HADES was designed as a non-focusing spectrometer with a transverse impulse kick (between 50 and 100 MeV/ $c$ ) transmitted to charged particles. The spectrometer is equipped with a superconducting toroidal magnet, see Figure 3.5. This magnet has six coils placed in separate vacuum chambers. The region around the target and in the RICH active volume is field free. In the first approximation, charged particles are bended only in polar direction. Azimuthal deflections in trajectories are getting

more important only close to borders of sectors, where the magnetic field suffers from inhomogeneities.

### 3.3. Time of flight wall

Time of flight measurements are provided by means of a scintillator detector wall. This wall has two parts called TOF<sub>ino</sub> and TOF which are placed behind the tracking system. Besides the time of flight measurements, both detectors play a crucial role as a part of the first level trigger. Furthermore, signal from TOF is also used in the second level trigger. The HADES trigger system will be described in more detail in Section 3.6.

#### 3.3.1. TOF

The TOF detector was build up by our Řež group in collaboration with Italian colleagues from INFN at Catania. Therefore, during several experiments, I actively participated in maintenance, calibration, and operation of the TOF detector.

TOF has a hexagonal symmetry and covers the polar angle between 44–88 deg. It consists of 384 scintillator rods. Each rod is terminated with two bended light-guides which transport scintillation light to photomultipliers. Each of the six sectors contains 64 rods arranged into 8 modules. Since HADES is a fixed target experiment, the flux of particles increases with the declining polar angle. In order to achieve reasonable space resolution at smaller polar angles, cross-section of the first 32 rods closest to the beam in each sector is only  $20 \times 20 \text{ mm}^2$ . At larger  $\theta$ , rods have a cross-section of  $30 \times 30 \text{ mm}^2$ . TOF uses photomultipliers which provide an analogue and a timing signal at the same time.



Figure 3.6.: TOF.

A flow chart of the timing and the amplitude electronic chain is shown in Figure 3.7. A beam particle passes through the START detector, enters to the target, reacts, and creates new particles. If they hit a TOF scintillator rod, light is transmitted to photomultipliers on both sides. Each of them then provides two signals

on the output. The negative signal from the last dynode is used for the amplitude measurement. The positive anode signal is employed for the purposes of timing. The amplitude chain further proceeds through a shaper and an amplitude to digital converter (ADC). The timing signal has to pass through a constant fraction discriminator (CFD) and subsequently, it is split into two branches. The first branch goes via a logic active delay (LAD) to a time to digital converter (TDC). The second branch enters to the first level trigger, where an analogue sum of timing signals from all photomultipliers is made. In this way, the reaction multiplicity is estimated. Afterwards, the first level trigger makes a logic AND of the multiplicity signal with the START signal.

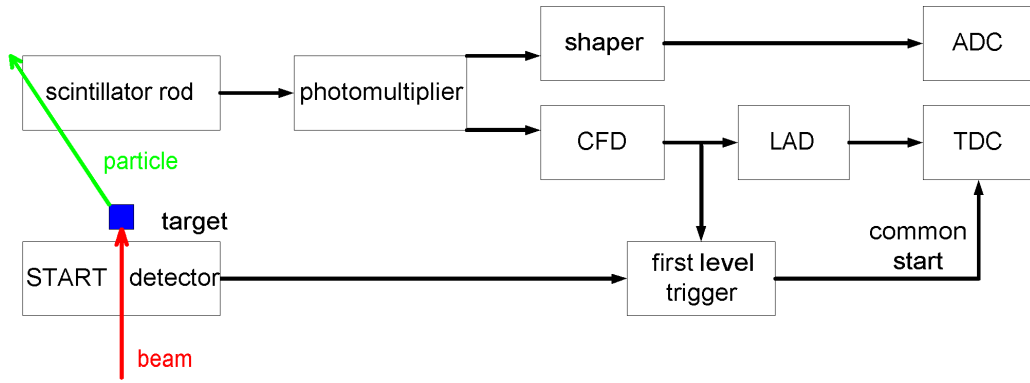


Figure 3.7.: Schematic chart of the TOF electronics chain. See the text for comments to this figure.

If a charged particle passes through a scintillator rod, its left and right photomultipliers give us time ( $t_{left}$ ,  $t_{right}$ ) and amplitude ( $a_{left}$ ,  $a_{right}$ ) signals. For the time of flight ( $tof$ ), position of the hit ( $x$ ,  $x_a$ ), and energy loss in the scintillator ( $\Delta E$ ), we may write

$$tof = \frac{1}{2} \left( t_{right} + t_{left} - \frac{L}{v_g} \right), \quad (3.1)$$

$$x = \frac{v_g}{2} (t_{right} - t_{left}), \quad (3.2)$$

$$\Delta E = k \sqrt{a_{right} a_{left} \exp \frac{L}{\lambda_{at}}},$$

$$x_a = \frac{\lambda_{at}}{2} \ln \left( \frac{a_{left}}{a_{right}} \right).$$

Here  $L$  is a length of the rod. The symbols  $v_g$  and  $\lambda_{at}$  denote a group velocity and an attenuation length of light in the scintillator, respectively. A careful reader noticed that there are two independent ways how to determine the  $x$  position of a hit. One can employ either the information from time signals or amplitude signals. In reality, only the first possibility is used. A typical time resolution ( $\sigma$ ) achieved by TOF is about 150 ps. A typical uncertainty in the position  $x$  reaches cca 3 cm.

### 3.3.2. TOFino

TOFino covers polar angle 18–45 deg. Each of its six sectors has four scintillator trapezoidal paddles oriented radially with respect to the beam axis. Their thickness is 1 cm and the height is about 130 cm. At the perimeter, bended, “fish tail” shaped lightguide connects each TOFino paddle with one photomultiplier. The photomultipliers provide both, amplitude and timing signals which then enter to an electronic chain similar to that of TOF.

TOFino is mounted directly on the front of the Pre-Shower detector. Since TOFino is not able to measure position of a hit, hit coordinates are provided by the Pre-Shower chamber. For the time of flight (*tof*), it follows

$$tof = t - \frac{x}{v_g},$$

where  $t$  denotes the time interval between the START signal and the instant when light arrives to a photomultiplier,  $x$  is the distance between the hit in the Pre-Shower chamber and the photomultiplier, and  $v_g$  is the group velocity of light in the scintillator. TOFino has rather poor time resolution (about 420 ps) and suffers from low granularity.

## 3.4. Shower

Shower detector provides additional identification of  $e^+/e^-$  at low polar angles (18–45 deg). In this region, hadronic background becomes to be more significant. Velocity of light hadrons, especially pions, emitted into small polar angles may be very high. Their time of flight then does not differ too much from that of electrons and positrons. Moreover, during a nucleus-nucleus collision many fragments and particles are produced. The identification based on TOFino time of flight measurement then often fails, as there is a large probability to have more than one hit in a TOFino paddle.

Shower measures electromagnetic showers induced by electrons and positrons in high  $Z$  material. The detector is divided into six trapezoidal sectors, covering the full azimuthal angle. Each sector consists of three planes of Multi Wire Proportional Chambers, separated by two inset layers of lead converters. A converter plate has a thickness of cca 1 cm corresponding to about 2 radiation lengths. Each proportional chamber has one anode wire plane and two cathodes. One cathode is segmented into  $3 \times 3$  cm<sup>2</sup> pads. Chambers are filled with a mixture of argon and isobutane gas. These quenching gases absorb photons produced during the secondary ionization. Therefore, the charge collected at the anode wire does not depend on the energy deposited but only on the number of particles traversing the chamber.

## 3.5. START and VETO detectors

START and VETO are two identical 8-strip diamond detectors, see Figure 3.8. They are placed in the beam line 75 cm in front of and 75 cm behind the target. A beam particle passing through the START detector initiates data acquisition and time counting. If no reaction occurred in the target, the beam particle hits VETO which then sends a signal to stop the data taking. Signals from START and VETO enter to the first level trigger box. The START detector is also used as a beam diagnostic tool.

Both detectors have an octagonal shape with outer dimensions ( $25 \times 15 \text{ mm}^2$ ) ensuring that all beam particles will pass through the detector. The diamond strips are made only  $100 \mu\text{m}$  thick, to suppress multiple scattering and secondary reactions of beam particles. Time resolution of the START detector is about 30 ps.



Figure 3.8.: START diamond strip detector.

## 3.6. Trigger and data acquisition system

Production of a vector meson followed by its di-electron decay is a rare process. Therefore, intensive beams of the order of  $10^6$  particles/s are needed to collect sufficient statistics of such events. However, the vast number of reactions are not interesting for HADES. Archiving all of them without any pre-selection would require enormous disc space capacity and a data storage velocity of several Gbyte/s. Hence, HADES is equipped with a two level on-line trigger system. The first level trigger (LVL1) selects more central events. The second level trigger (LVL2) looks for lepton candidates in LVL1 events. HADES has also a subsequent off-line third level trigger based on software. It uses tracking information from MDCs to reduce the number of fake leptons. Independently on the trigger system, minimum bias events are collected. These events are stored without regarding the LVL1 trigger decision.

HADES has a distributed system of the VME crates with a specific detector electronics. In the heart of the LVL1 and LVL2 trigger system, there is the Central

Trigger Unit (CTU). It reacts on several trigger input sources, makes decision, and forwards it via LVL1 and LVL2 Trigger Bus to the Detector Trigger Units (DTUs). Here, the trigger decision is converted to an instruction which tells to a detector which action to perform. Readout process is running on the VME-CPU's. The scheme can be seen in Figure 3.9.

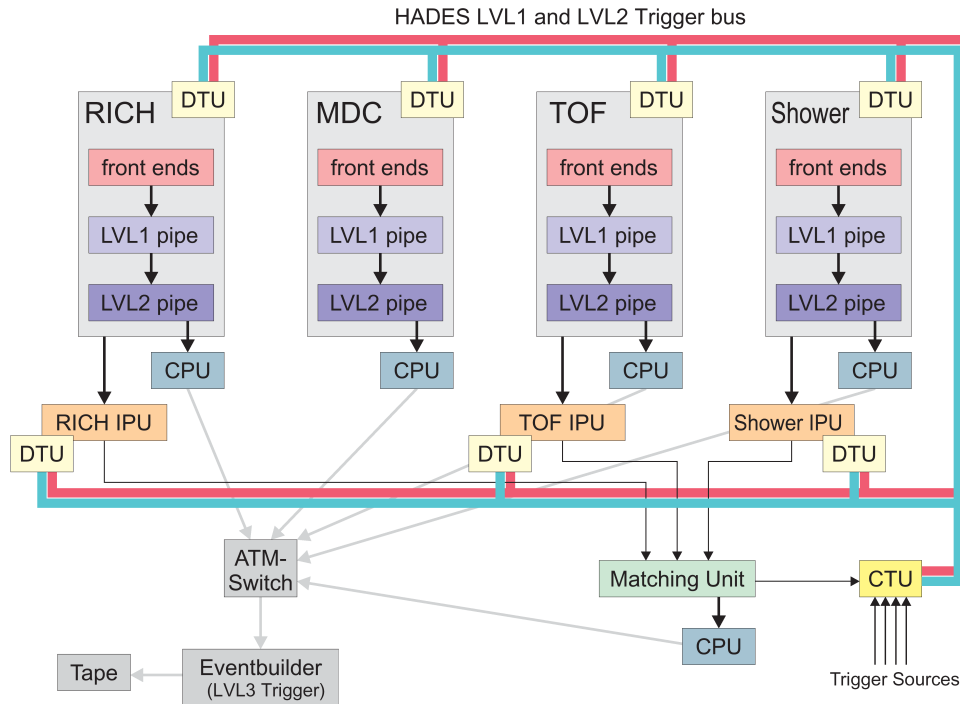


Figure 3.9.: Trigger and data acquisition scheme. The chart is explained in the text. The figure is taken from [72].

While waiting for a trigger decision, data are stored in pipes (buffers). Depending on the trigger instruction they are discarded or sent to the following pipe or to the central Event Builder.

### 3.6.1. First level trigger

Possible medium modifications of vector meson properties should be more pronounced in central collisions as there larger volume of hot and dense matter is produced. Hence, the LVL1 trigger of HADES is designed in the way to select preferentially more central reactions.

An event is recognized as the LVL1 trigger event if there is the positive signal from the START detector in coincidence with the positive multiplicity signal from the Time of flight wall and the negative signal from the VETO detector. The positive multiplicity signal from the Time of flight wall is provided when the sum of analogue signals from TOF and TOF<sub>ino</sub> exceeds a certain threshold. This condition can be written as follows

$$(M_{TOFL} + M_{TOFR} + 2M_{TOFino})/2 \geq M_{thr}.$$

Here  $M_{TOFL}$  and  $M_{TOFR}$  are the numbers of hits detected by left and right TOF photomultipliers, respectively,  $M_{TOFino}$  is the number of fired TOFino paddles, and  $M_{thr}$  is a LVL1 trigger threshold.

The LVL1 trigger provides common start or stop signals for time measurements as well as gate signals for charge collection. A typical LVL1 trigger reaction rate reductions are about one order of magnitude. A LVL1 trigger decision is available for any detector within the HADES set-up in 500–600 ns.

#### 3.6.2. Second level trigger

If an event was marked positively by the LVL1 trigger, the Image Processing Units (IPU) in RICH, TOF, and Shower search for lepton signatures in the collected data, see Figure 3.9. Angular coordinates of Cherenkov rings in RICH, fast particles in TOF, and centres of electromagnetic showers in Shower are then provided to the Matching Unit (MU). The Matching Unit checks whether the angular positions of hits in RICH and Meta detectors (TOF, Shower) are within certain windows. The decision is then delivered to the Central Trigger Unit, which sends it via the LVL2 trigger bus to the Data Trigger Units.

### 3.7. Software tools

On-line and off-line data load provided by the HADES spectrometer is processed and analyzed using the HYDRA software. HYDRA (*Hades sYstem for Data Reduction and Analysis*) [63] is an object-oriented modular framework based on ROOT C++ classes. It contains libraries with methods which can be used for a real experiment as well as for a simulation analysis. Parameters concerning geometry, set-up, and calibration are retrieved from the Oracle data base or ROOT files.

The CERN software ROOT [64] is one of the most frequently used tools used for data analysis in high energy physics. Based on object oriented programming, it enables to effectively treat large data samples.

The HGeant code was developed to simulate propagation of reaction products through the body of the HADES spectrometer. It is based on the Geant 3 code [65].

Pluto [66, 67] is a Monte Carlo based event generator which simulates lepton production in heavy ion collisions and elementary reactions. Inputs to the code are experimentally measured particle multiplicities, their decay schemes, branching ratios, fireball temperatures, and coefficients describing angular anisotropies in particle emission.

The algorithm used for tracking is based on the fourth-order Runge-Kutta method of Nystom [68]. It is used to solve equations of motion in a known field region. Initial track parameters for the algorithm are provided by more simple methods, kick plane and spline, discussed elsewhere [60]. The tracking algorithm iteratively optimizes the track parameters to achieve better fit to measured hit positions in MDCs. It does not take into account energy losses and multiple scattering of particles in the material (A typical material budget is below 3 % of the radiation length).

## 4 Ar+KCl @ 1.756 A GeV

Starting from this chapter, I will concentrate on the analysis of  $e^+e^-$  pair production in Ar+KCl collisions at 1.756 A GeV which was measured by the HADES collaboration in September and October 2005. The experiment was carried out with my active participation. I was responsible for maintenance and calibration of the TOF detector. Further, I was one of the persons that were involved in the pair analysis of this run.

The KCl target was chosen in order to get closer to isospin symmetric projectile-target system. The energy of the argon beam was sufficient to excite many different di-lepton sources. Let us mention two experiments from the past which studied particle production in similar systems and can be used as a reference to our measurement. The first one is the Bevalac experiment which measured pion production in Ar+KCl at 1.8 A GeV [76]. The second experiment is the TAPS measurement of  $\eta$  meson production in Ar+Ca at 1.5 A GeV [77].

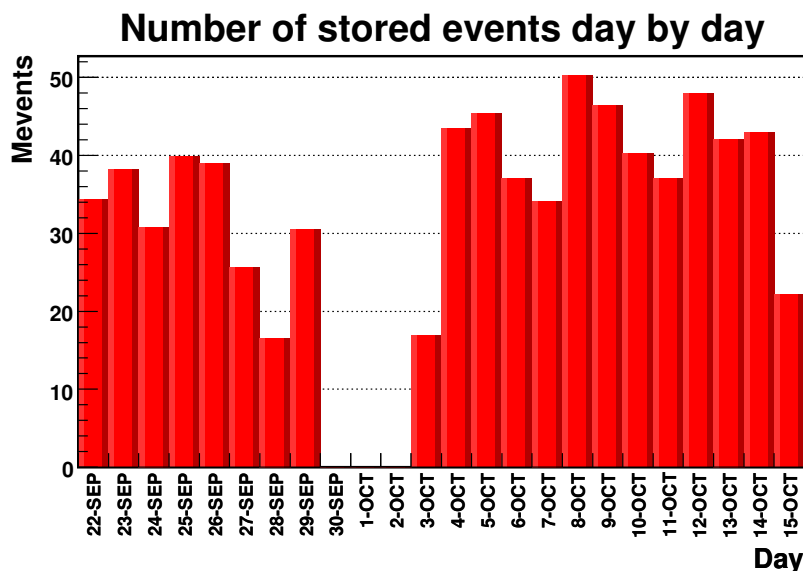


Figure 4.1.: Amount of collected data viewed day by day.

Figure 4.1 shows a course of data taking during the Ar+KCl experiment. There was one longer interruption at the end of the September when the beam time was given to parasites. Even though the collaboration managed to collect around 841 millions of events. This number includes also the events which were taken under modified experimental conditions, e.g., the run with an empty target, the run with a calcium target, downscaled trigger events, or the data measured without the magnetic field. Altogether I analyzed about 570 millions events. This statistics corresponds to about  $2.25 \times 10^9$  first level trigger events on the input to the trigger box which were stored with the downscaling 1:10. In September 2005, the HADES spectrometer was not completed yet. The MDC chambers in the plane 4 on the sectors 2 and 5 were missing.

## 4.1. Target and beam

We used target made of natural KCl. It had four identical cylindrical segments, with a radius of 1.5 mm and a thickness of 1.25 mm, see Figure 4.2. The distance between two neighbouring segments was 9 mm. The density of KCl is 1988 kg/m<sup>3</sup>. The target had an interaction length of about 3.05 %.



Figure 4.2.: KCl target.

The <sup>40</sup>Ar beam had a kinetic energy of 1.756 A GeV. A typical beam intensity was cca  $6 \times 10^6$  particles per spill. One spill took about 10 s. Other properties of K, Cl, and Ar are listed in Table 4.1.

Element	Relative atom mass	Proton number	Isotopes
K	39.098	19	<sup>39</sup> K (93.26 %), <sup>41</sup> K (6.73 %)
Cl	35.453	17	<sup>35</sup> Cl (75.77 %), <sup>37</sup> Cl (24.23 %)
<sup>40</sup> Ar	39.962	18	

Table 4.1.: Properties of K, Cl, and <sup>40</sup>Ar.

## 4.2. Calibration of the TOF detector

One of my duties was to calibrate the TOF detector. In a TDC device, the time signal from a photomultiplier is corrected on the START time and converted to channels. The relation between the time in nanoseconds ( $t_R, t_L$ ) and channels ( $t_R^{ch}, t_L^{ch}$ )

is assumed to be linear

$$\begin{aligned}t_R &= k_R t_R^{ch} + C_R, \\t_L &= k_L t_L^{ch} + C_L.\end{aligned}$$

Here  $k_R$ ,  $k_L$  are slope parameters and  $C_R$ ,  $C_L$  are constants. The indices  $R$  and  $L$  label quantities which are connected to the right-hand side and the left-hand side of TOF, respectively. Inserting the above equations into (3.1) and (3.2), according to which a position and time of flight are calculated in TOF, it can be seen that

$$x = \frac{v_g}{2} (k_R t_R^{ch} - k_L t_L^{ch}) + x_0$$

and

$$tof = \frac{1}{2} (k_R t_R^{ch} + k_L t_L^{ch}) + t_0.$$

Here  $t_0$  and  $x_0$  are time and position offsets. The parameters  $k_R$ ,  $k_L$ ,  $t_0$ , and  $x_0$  have to be determined from a calibration.

The calibration of the slope parameters  $k_R$  and  $k_L$  is done in the following way. First, a time spectrum with a pulser is measured. Subsequently, the signal path is prolonged by means of a cable with a known delay, e.g., 50 ns. In the time spectrum, we should then observe a shift of the time peak position which corresponds to the known delay in ns. The ratio of the cable delay and the peak shift gives us the unknown slope parameter.

The calibration of the position offset  $x_0$  is based on a more precise position measurement provided by MDCs. According to the hit position in MDCs, tracking procedure calculates the corresponding position in TOF ( $x_{\text{MDC}}$ ). The value of  $x_0$  is then for each rod set so that the mean of the distribution  $D = x - x_{\text{MDC}}$  equals zero, see Figure 4.3.

To calibrate the time offset  $t_0$ , electron candidate tracks are used. These tracks are assigned to some RICH ring. Since all leptons have velocity close to the speed of light they manage to get from the target to the TOF detector in approximately 7 ns. The measured time is normalized to a constant path length of about 210 cm. In the time spectrum, the mean of the lepton peak is then set to 7 ns, see Figure 4.4.

The group velocity  $v_g$  and the attenuation length were known from previous runs.

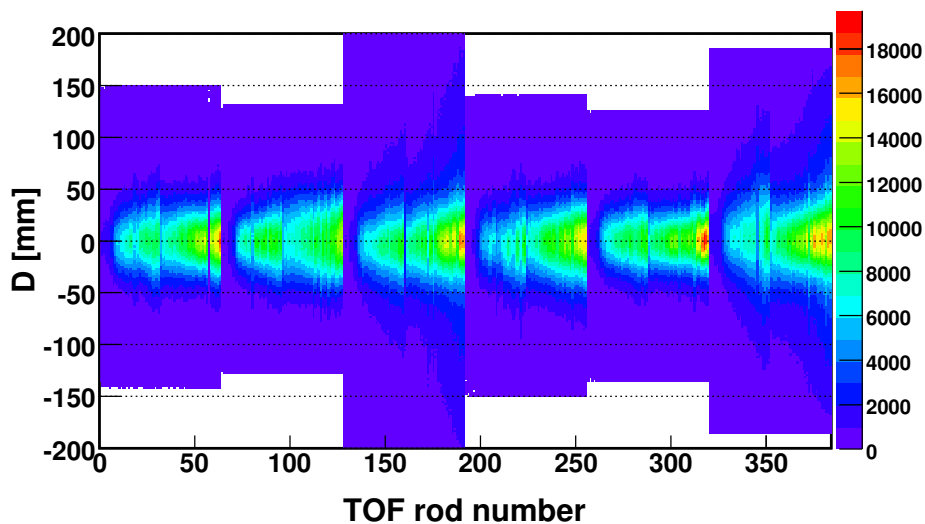


Figure 4.3.: Position calibration of TOF. The plot shows  $D = x - x_{\text{MDC}}$  versus a consecutive number of a TOF rod.

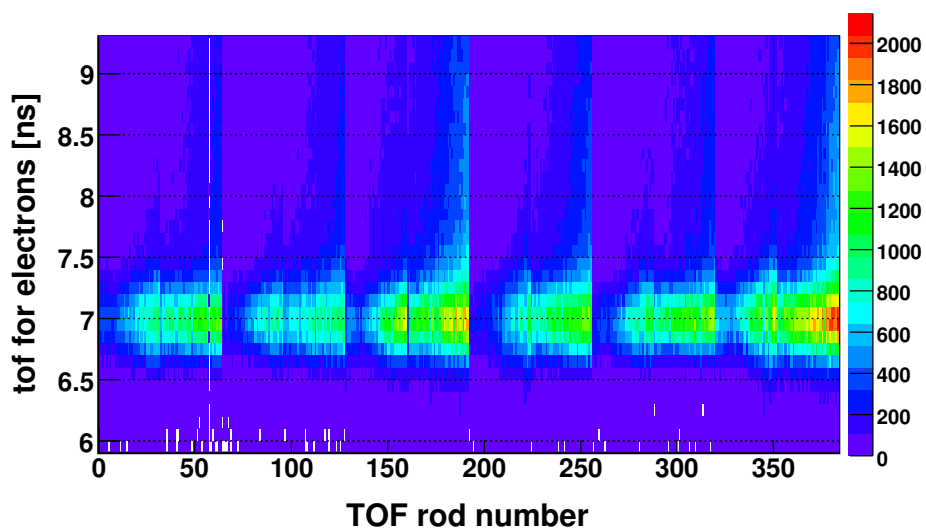


Figure 4.4.: Time calibration of TOF. The plot shows time of flight of lepton candidates versus a consecutive number of a TOF rod.

## 5 Trigger studies

Let us shortly recall that HADES uses two level on-line trigger. The first level trigger (LVL1) is the multiplicity trigger selecting more central collisions. Subsequently, the second level trigger (LVL2) searches for lepton candidates in LVL1 events. For more details see Section 3.6. In this chapter, I will show how both triggers worked in case of the Ar+KCl run.

### 5.1. Empty target run

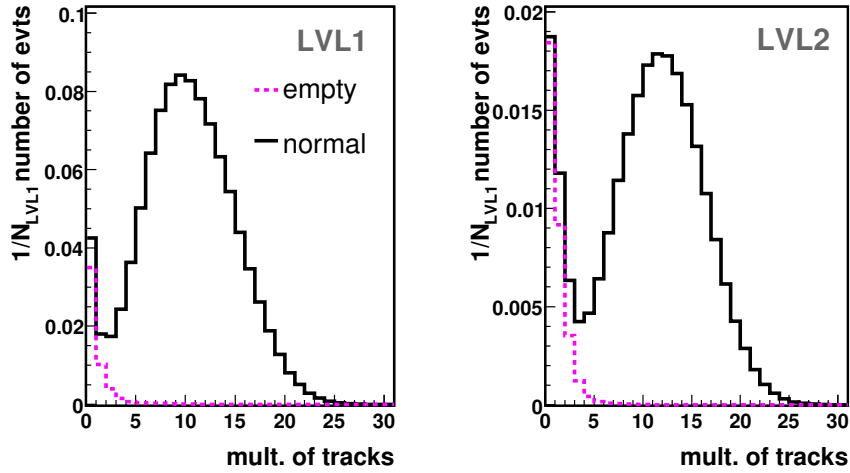


Figure 5.1.: Multiplicity distribution of tracks. Comparison of the normal (black histogram) and the empty target (pink histogram) run. **Left:** Events with the positive LVL1 trigger decision. **Right:** Events with the positive LVL2 trigger decision. All distributions are normalized on LVL1 trigger event.

A registered LVL1 trigger event does not need to originate from a reaction which occurred in the target. Bad focusing of the beam or halo particles may cause interactions outside of the target, e.g., in the beam pipe tube, the beam pipe exit window, or the START detector. To estimate frequency of this kind of events a dedicated empty target measurement was carried out. In Figure 5.1, two plots, illustrating the portion of empty target events in positively triggered LVL1 and LVL2 events of the normal run, are shown. Different experimental conditions during the normal and the empty target measurements I took into account by scaling the empty target distributions with a factor

$$\frac{\mathcal{T}_{\text{Normal}} \mathcal{N}_{\text{Normal}}^{\text{START}}}{\mathcal{T}_{\text{Empty}} \mathcal{N}_{\text{Empty}}^{\text{START}}}.$$

Here  $\mathcal{N}_{\text{Normal}}^{\text{START}}$  and  $\mathcal{N}_{\text{Empty}}^{\text{START}}$  are the numbers of START signals in the normal and the empty target run, respectively. Further,  $\mathcal{T}_{\text{Normal}}$  and  $\mathcal{T}_{\text{Empty}}$  denote dead time corrections. They were estimated as the ratio of the number of LVL1 events on the

input to the trigger box and the number of LVL1 events stored on the tape in the normal and in the empty target measurements, respectively. Contrasting both sides in Figure 5.1, we may conclude that the LVL2 trigger enhances the portion of empty target events in the normal run sample. In all registered LVL1 events, the fraction of empty target events is about 5 % while in case of LVL2 events, this fraction reaches cca 14 %. Moreover, Figure 5.1 suggests that the empty target events create a peak at low track multiplicities. This results from the fact that our tracking algorithm reconstructs only particle trajectories originating from the target region.

## 5.2. Event vertex cut

In order to effectively suppress the contribution of empty target events in our data sample, I applied several constraints on a reconstructed event vertex position. The selected target region was

$$\begin{aligned} -2.46 \text{ mm} < V_x < 2.46 \text{ mm}, \\ -2.46 \text{ mm} < V_y < 2.46 \text{ mm}, \\ -52.0 \text{ mm} < V_z < -9.0 \text{ mm}, \end{aligned}$$

see Figure 5.2. This corresponds to a cut on 4 standard deviations, roughly.

I checked that this cut on a reconstructed event vertex position rejected all events from the empty target run. Moreover, if we contrast the track multiplicity distribution of the LVL2 events, which did not pass the event vertex cut in the normal run, with the track multiplicity distribution of LVL2 events in the empty target run, both distribution nicely agree, see Figure 5.3. Thus, we may conclude that after the cut on a reconstructed event vertex position, the admixture of empty target events is negligible in our data sample. In addition, Figure 5.3 suggests that the cut is not restrictive too much and does not suppress reactions which occurred in the target.

## 5.3. Simulation of the LVL1 trigger

In order to have a deeper insight into the procedure of event selection, which is trigger doing in an experiment, it is necessary to employ a realistic simulation. I produced simulated events in four steps. First, Ar+KCl collisions at 1.756 A GeV were generated using the transport code UrQMD [69, 70, 71]. Second, output events from the UrQMD were filtered with the so-called converter macro. This macro removed from a reaction spectator particles not going to the HADES spectrometer. Third, the filtered events were processed with the program HGeant, which calculated energy losses and interactions of reaction products in the HADES spectrometer. Finally, response of individual sub-detectors on an incoming signal was modelled with the so-called *digitizers* which are a part of the HYDRA framework.

Our simulation produces only reactions which take place in the target. Hence, experimental data from the normal run have to be corrected on the empty target

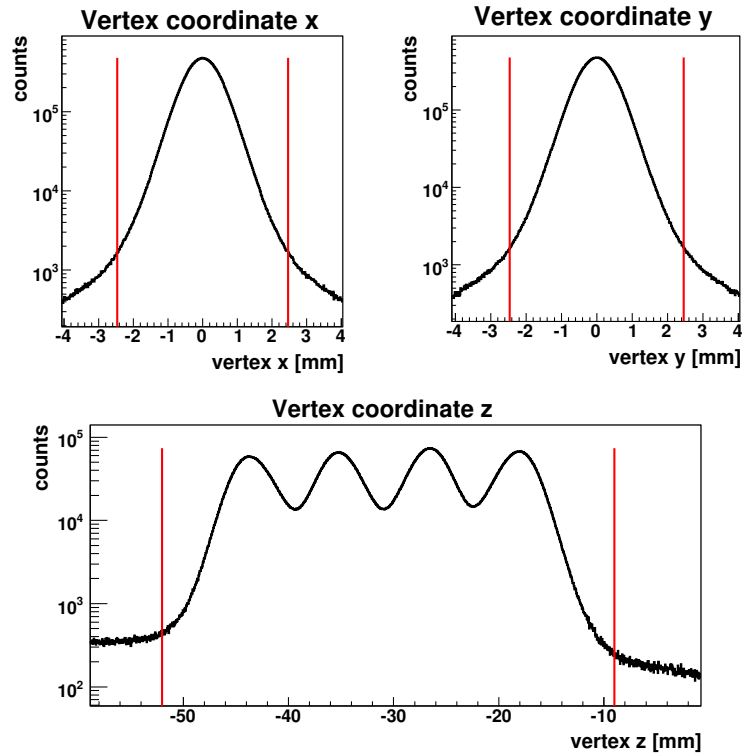


Figure 5.2.: Reconstructed  $x$ ,  $y$ , and  $z$  coordinates of reaction vertices. We may clearly see the arrangement of the four-segmented KCl target. The red lines show the limits which were applied on a reconstructed event vertex position.

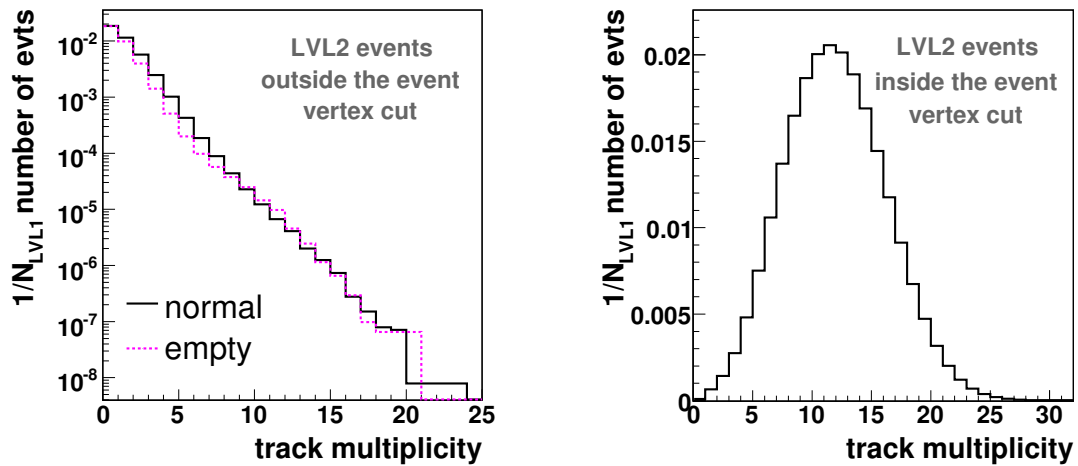


Figure 5.3.: **Left:** The black histogram shows a track multiplicity distribution in the LVL2 events, which did not passed the event vertex cut in the normal run. The violet dashed histogram depicts a track multiplicity distribution in empty target run LVL2 events. Both histograms are normalized on LVL1 event. **Right:** Distribution of track multiplicity in the LVL2 events which passed the event vertex cut in the normal run. Histogram is normalized on LVL1 pure target event.

contribution. This can be done either with the event vertex cut or by subtracting properly scaled empty target distributions from the corresponding normal run histograms. Both ways give us an estimate of a yield coming out of the *pure target*.

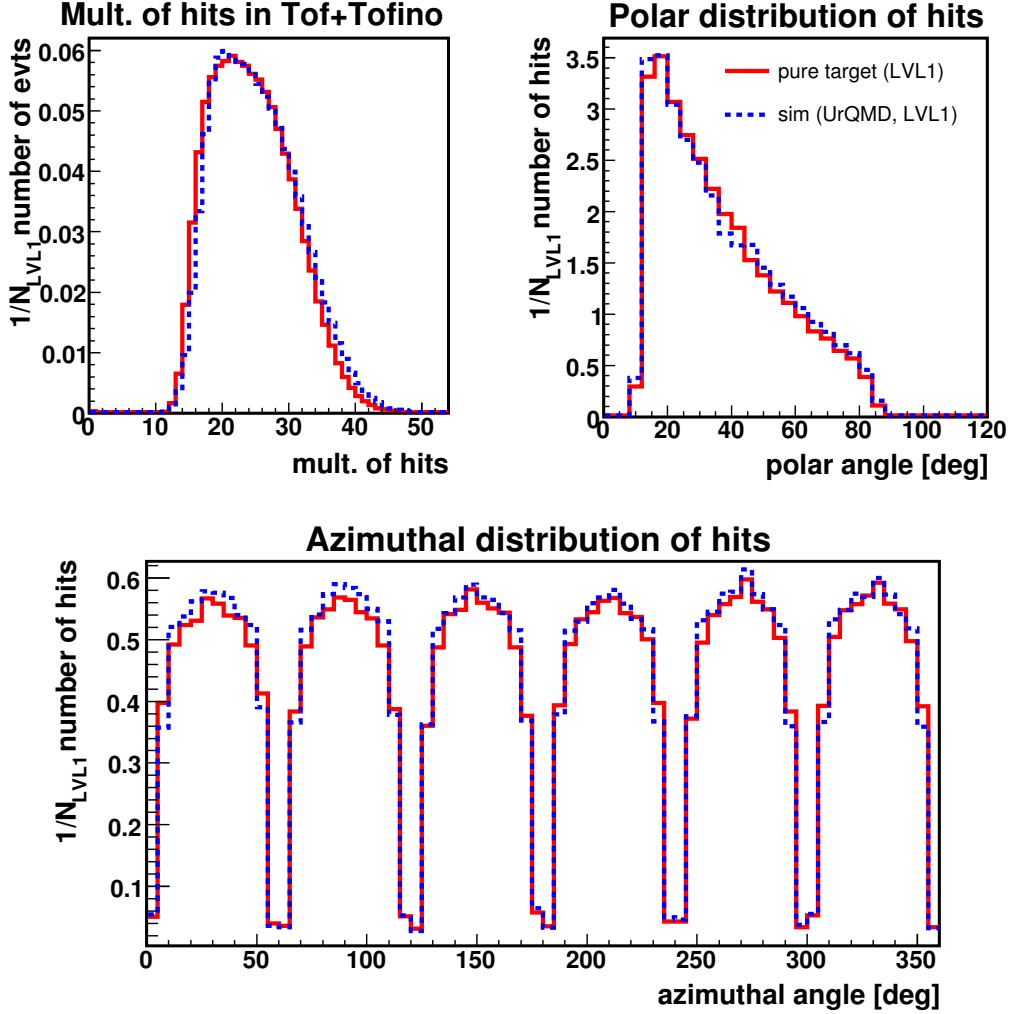


Figure 5.4.: **Top left:** Multiplicity of hits in TOF+TOFino in events with the positive LVL1 trigger decision. **Top right:** Distribution of hits in polar angle. **Bottom:** Distribution of hits in azimuthal angle. Comparison of the experiment (red solid line histograms) and the UrQMD simulation (blue dashed line histograms). All distributions are normalized on LVL1 pure target event.

I modified the HYDRA LVL1 trigger emulator to achieve a better agreement of the UrQMD simulation with the experiment. In the proposed version, only the particles, which hit the Time of flight wall within 40 ns after the initial reaction occurred, are taken into account. This time cut reduces an influence of the slow secondary particles which would otherwise contributed to the simulated reaction multiplicity signal. Let us point out that the applied constraint is not much restrictive. For passing the distance from the target to the Time of flight wall, relativistic leptons need typically 7 ns and primary participant protons need about 15 ns. Also in experiment, similar

time limitation is applied. Analogue signals from TOF and TOFino have to overlap with the START signal within the 40 ns gate window otherwise the data acquisition is not initiated. Further, for each simulated event, the hit multiplicity threshold was randomly sampled from the Normal distribution. The mean number of hits in TOF+TOFino was set to 16 and the standard deviation to 1.8. The introduced smearing should simulate inefficiencies in summing of the analogue signals from TOF+TOFino. In Figure 5.4, we compare multiplicity and angular distributions of hits corresponding to the experimental pure target reactions and our UrQMD simulation.

## 5.4. Simulation of the LVL2 trigger

A large part of the positive LVL2 trigger events is initiated by an electron or a positron coming from a  $\pi^0$  decay. As the pion multiplicity increases approximately linearly with the number of participants, it is interesting to study whether the LVL2 trigger introduces some centrality bias on the sample of events selected by the LVL1 trigger.

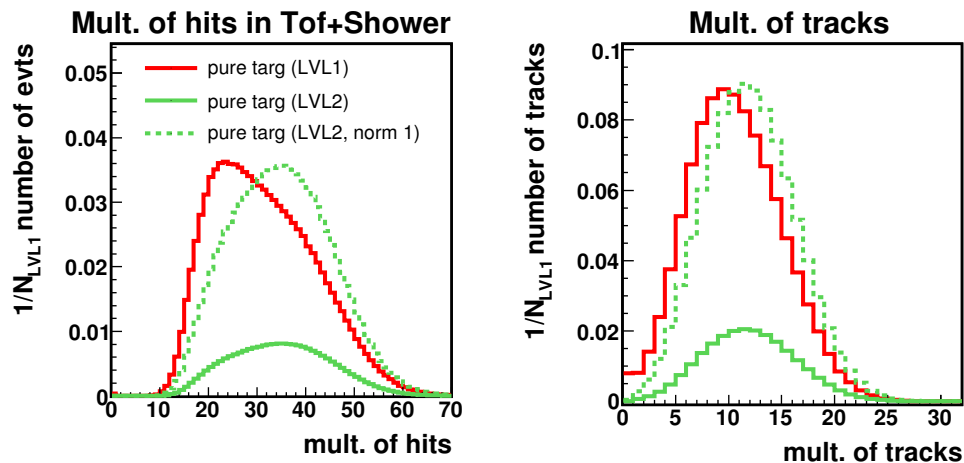


Figure 5.5.: **Left:** Experimental multiplicity distributions of hits in TOF+Shower in pure target events with the positive LVL1 (red histogram) and the positive LVL2 (green histogram) trigger decision. **Right:** Charged particle track multiplicity distributions in LVL1 and in LVL2 pure target events. All histograms are normalized on LVL1 event.

In Figure 5.5, I contrast pure target hit and track multiplicity distributions from events with the positive LVL1 and the positive LVL2 trigger decision. To see the shape of the LVL2 histograms better they are also sketched normalized to a unit surface (green dashed line). Both plots suggest that LVL2 events have a slight tendency towards larger hit and track multiplicities when compared to LVL1 events. Some small bias of the LVL2 trigger on the selected impact parameter region can be thus awaited.

The HYDRA software does not assign the second level trigger decision to simulated events. Therefore, I wrote a dedicated macro to imitate the LVL2 trigger

decision procedure. The simulation correctly shifts the distributions of LVL2 trigger events towards higher hit and track multiplicities, see Figure 5.6. Moreover, it predicts quantitatively correctly also the portion of positively triggered LVL2 events in LVL1 event sample. This portion reaches in the experiment (pure target) 21.4 % and in our simulation 23.9 %.

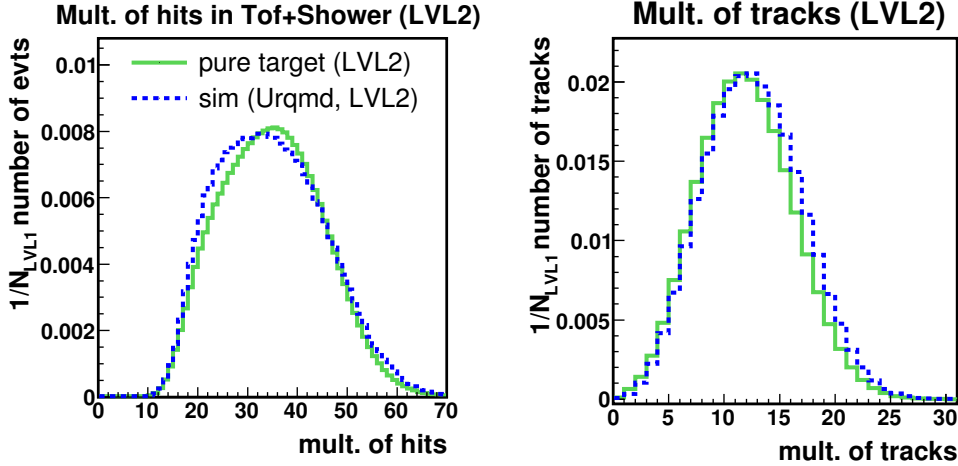


Figure 5.6.: **Left:** Distribution of multiplicity of hits in TOF+Shower for positively triggered LVL2 events in experiment (green histogram) and in simulation (blue dashed histogram). **Right:** Charged particle track multiplicity distributions in simulated and in experimental pure target LVL2 events. The normalization was done on LVL1 event.

## 5.5. Impact parameter distribution

Now let us deal with the question which region of impact parameters was selected by the LVL1 and the LVL2 trigger. Unfortunately, a collision impact parameter cannot be experimentally directly measured. Thus, we have to rely on our simulation – which gives us quantitatively correct predictions for hit and track distributions as we have shown.

Trigger	Mean impact parameter [fm]	Portion in MB events [%]	Pion mult. enhancement with respect to MB
LVL1	3.54	34.4	2.0
LVL2	3.18	8.2	2.2

Table 5.1.: Characteristics of events selected by the LVL1 and the LVL2 trigger. Abbreviation MB stands for minimum bias reactions. All quoted numbers were determined from the UrQMD simulation.

Our UrQMD simulation produces minimum bias reactions. Each simulated event carries information about its collision impact parameter. If we process UrQMD collisions with our analysis chain (HGeant, digitizers, etc.), we end up with a sample

events, marked with the LVL1 and the LVL2 trigger, with known impact parameters. The selected impact parameter distributions are shown in Figure 5.7. The UrQMD simulation suggests that the second level trigger prefers a little bit more central collisions when compared to first level trigger events. In Table 5.1, I quote some numbers characterizing the LVL1 and the LVL2 trigger event selection, i.e., the mean selected centrality, the portion of events picked out from the minimum bias reactions, and the enhancement of the mean pion multiplicity in triggered events with respect to minimum bias events.

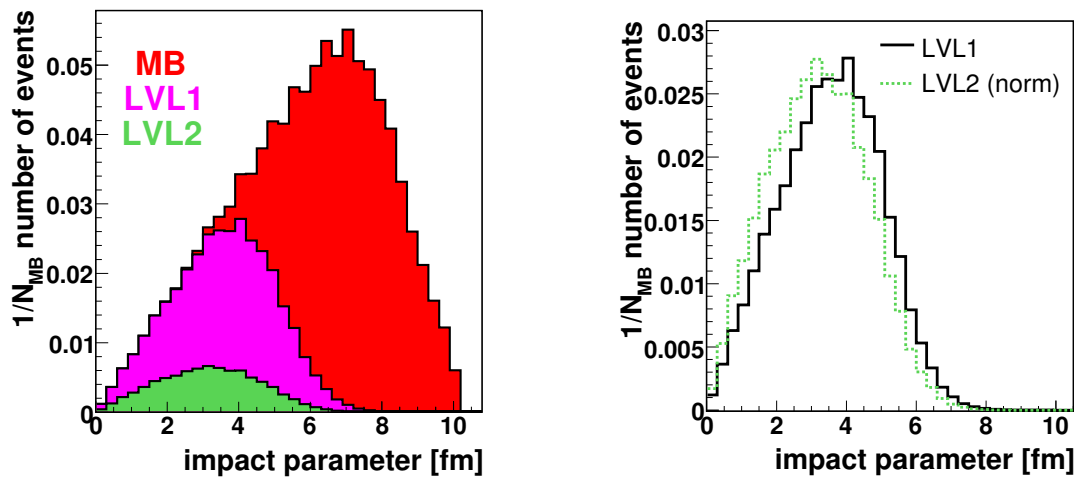


Figure 5.7.: Impact parameter distribution of Ar+KCl collisions at 1.756 A GeV. **Left:** Comparison between minimum bias reactions (red histogram), LVL1 trigger events (magenta histogram), and LVL2 trigger events (green histogram). **Right:** The solid black line represents the LVL1 impact parameter distribution. The green dotted line shows the LVL2 distribution normalized to the same integral as the LVL1 histogram. Data are based on the UrQMD simulation. All distributions are normalized on minimum bias event.

## 5.6. Summary of this chapter

The cut on a reconstructed event vertex position can efficiently reject empty target events without suffering from substantial losses of the pure target reactions. After the cut, the amount of empty target events in our data sample is negligible. Based on the UrQMD simulation, I determined the region of reaction impact parameters selected by our LVL1 trigger, see Figure 5.7. In our positively triggered LVL1 events, the mean multiplicity of pions is approximately two times larger when compared to minimum bias reactions. The simulation, further, suggests that the bias of the LVL2 trigger on the selected centrality is on the level of 10 %.



## 6 Lepton analysis

HADES has to efficiently identify a weak electron/positron signal in hadronic background, which is many orders of magnitude more intensive. Particle identification algorithms have to combine information from several sub-detectors in order to assign a given track to a lepton. It is requisite to select the lepton sample carefully, because this shall be an input to the subsequent pair analysis.

For the purpose of lepton identification, I used the so-called *hard-cut* approach. The idea of this method is quite simple. By imposing sharp limits on measured continuous quantities (like velocity or collected charge) sample of reconstructed tracks is enriched with real leptons. In the framework of the statistical pattern recognition one would call this method thresholding. The hard-cut lepton analysis proceeds as follows. Electron and positron candidates are selected out of the tracks which are assigned to some Cherenkov ring candidate in RICH. Each ring has to satisfy several quality constraints. Further, a lepton candidate has to pass the limits on velocity which are given by the time resolution of the Time of flight wall. In addition, at low polar angles, an electron/positron candidate has to have the positive lepton signature in the Shower detector. In the following sections, I will refer in more detail on lepton identification in the HADES sub-detectors. The just mentioned hard-cuts can be applied in an arbitrary order. The only constraint is that my ntuples with lepton candidates contained only the tracks which were assigned to a ring. Therefore, the spatial matching between a ring candidate in RICH and a track segment in inner MDCs is considered as the first cut.

### 6.1. Lepton identification in RICH

In the past, two algorithms were developed for ring searching in the RICH pad plane. The first of them is based on the so-called Hough transform and the second one employs template matching. Positive decision from both algorithms is required when a ring is to be recognized in RICH.

The *Hough transform* is a well-known method frequently used in the domain of the statistical pattern recognition. Its adaptation for the purpose of a ring recognition in RICH is done in the following way. First, all possible combinations of three different fired pads are created. Algorithm then attempts to circumscribe to each triplet a ring with a known diameter. If it succeeds, it increases a counter at the position of the ring centre in an imaginary position plane. After processing all triplets, the ring centre is found as a local maximum in the imaginary position plane. A schematic of the algorithm is shown in Figure 6.1.

In the second approach, a template of a ring (*pattern matrix*), represented by a  $11 \times 11$  table of weights, is used. During the ring searching procedure, the template is shifted along the RICH pad plane, pad by pad. In each position, algorithm adds together charges of the fired pads ( $q_{ij}$ ) weighted by the corresponding numbers from

## 6. Lepton analysis

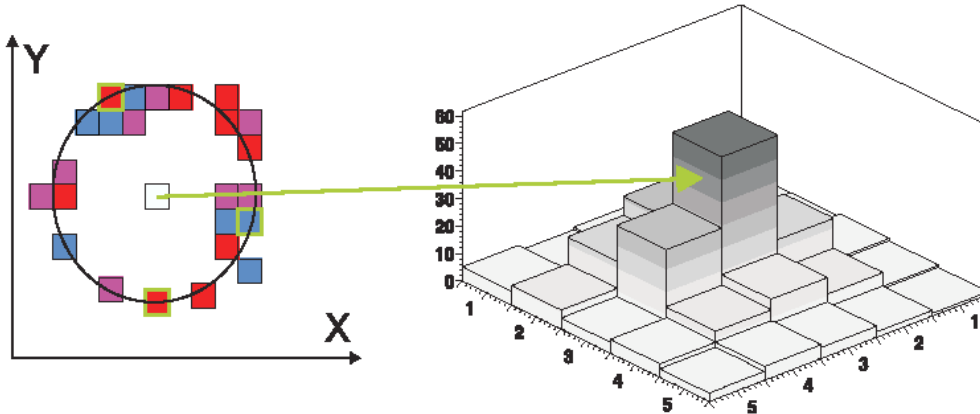


Figure 6.1.: Ring recognition algorithm based on the Hough transform. The figure is taken from [72].

the table  $(w_{ij})$ ,

$$Q_{PM} = \sum_{i=1}^{11} \sum_{j=1}^{11} q_{ij} w_{ij}.$$

Here the indices  $i$  and  $j$  run over rows and columns of the pattern matrix. The quantity  $Q_{PM}$  is called *pattern matrix quality*. For the true rings, it has larger values than for noise. Weights in the matrix are chosen in such a way to mask a ring. The pattern matrix has positive values on the borders of a ring, where we expect charge to be deposited in pads. On the other hand, in its corners and in the ring centre, values are chosen to be negative as there should be no fired pad, see Figure 6.2.

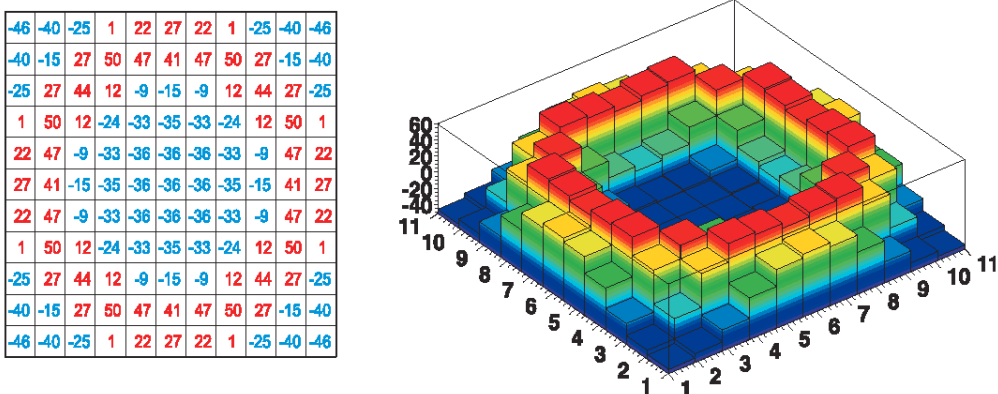


Figure 6.2.: The pattern matrix which is used for ring masking. **Left:** Table with weights. **Right:** Graphical representation. The figure is taken from [72].

### 6.1.1. RICH-inner MDC matching

When a lepton is produced, it usually arouses a ring in RICH and a connected ionization trace along its track in inner MDCs. Both objects, i.e., the ring and the track segment, are located in similar direction with respect to the target. In order to decide, which track could be assigned to a ring, we have to evaluate

$$\Delta\theta = \theta_{\text{RICH}} - \theta_{\text{MDC}},$$

$$\Delta\Phi \sin(\theta_{\text{MDC}}) = (\Phi_{\text{RICH}} - \Phi_{\text{MDC}}) \sin(\theta_{\text{MDC}}).$$

Here  $\theta_{\text{RICH}}$  and  $\Phi_{\text{RICH}}$  are polar and azimuthal coordinates of a ring in RICH, respectively, and  $\theta_{\text{MDC}}$  and  $\Phi_{\text{MDC}}$  stand for polar and azimuthal angles of a track segment in the target region provided by the tracking algorithm. The difference  $\Phi_{\text{RICH}} - \Phi_{\text{MDC}}$  is multiplied by the  $\sin(\theta_{\text{MDC}})$  in order to compensate for varying size of the  $\Delta\Phi$  window as a function of polar angle.

By imposing sharp limits on  $\Delta\theta$  and  $\Delta\Phi \sin(\theta_{\text{MDC}})$ , we can efficiently select lepton candidates. In the first step, the algorithm assigns to a ring all tracks within broad matching windows of  $\pm 10$  deg in  $\Delta\theta$  and  $\Delta\Phi \sin(\theta_{\text{MDC}})$ . In the next step, each combination of a track and a ring has to survive much more narrower matching windows, which are momentum dependent.

$$-2\sigma_{\theta}(p) \leq \Delta\theta \leq 2\sigma_{\theta}(p),$$

$$-2\sigma_{\Phi}(p) \leq \Delta\Phi \sin(\theta_{\text{MDC}}) \leq 2\sigma_{\Phi}(p),$$

where  $2\sigma_{\theta}(p)$  and  $2\sigma_{\Phi}(p)$  are the momentum dependent windows, see Figure 6.3.

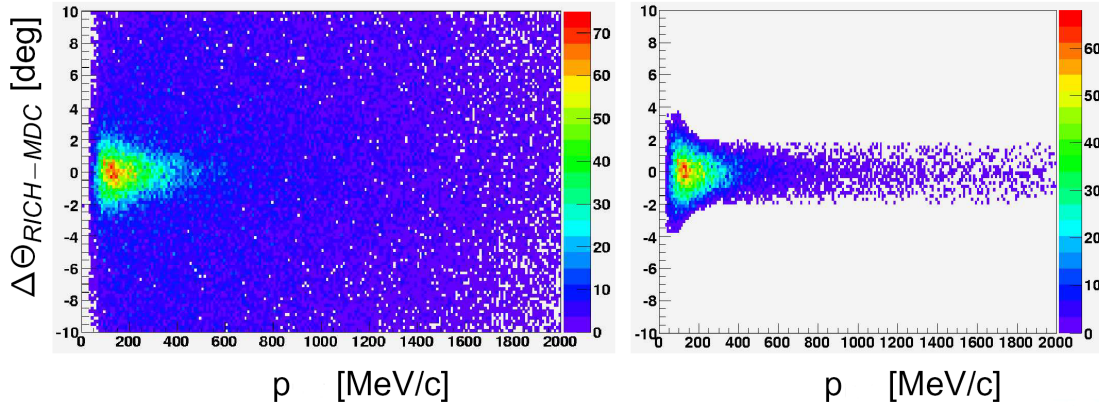


Figure 6.3.: Distribution of  $\Delta\theta$  versus track momentum. **Left:** Ring-track combinations which passed the broad 10 deg windows. **Right:** After momentum dependent  $\Delta\theta$  and  $\Delta\Phi \sin(\theta_{\text{MDC}})$  matching windows were applied. Data are from the Ar+KCl experiment. The figure is taken from [73].

Size of the these windows is influenced by an angular resolution of the RICH detector. Further, at low lepton momenta, the windows have to be broader due to the multiple scattering. In the Ar+KCl run, the RICH-inner MDC matching windows were produced by our RICH experts.

### 6.1.2. Ring quality parameters

Further, lepton candidates have to meet several ring quality constraints. The pattern matrix quality, the number of fired pads forming a ring, and the average charge per fired pad have to exceed certain thresholds. In addition, it is required that the distance between a position of the gravity centre<sup>1</sup> of a ring and its fitted geometrical centre has to be smaller than a certain value. The constraints are chosen not very much restrictive and 93 % of lepton rings fulfills them. Distributions of the ring quality parameters for lepton and hadron candidates are shown together with the applied cuts in Figure 6.4. Presented data are from the Ar+KCl experiment. Lepton candidates had to survive limits on RICH-inner MDC matching and velocity. In addition, at low polar angles, they had to fulfill the Shower condition. Hadron candidates are represented with tracks without any RICH-inner MDC matching.

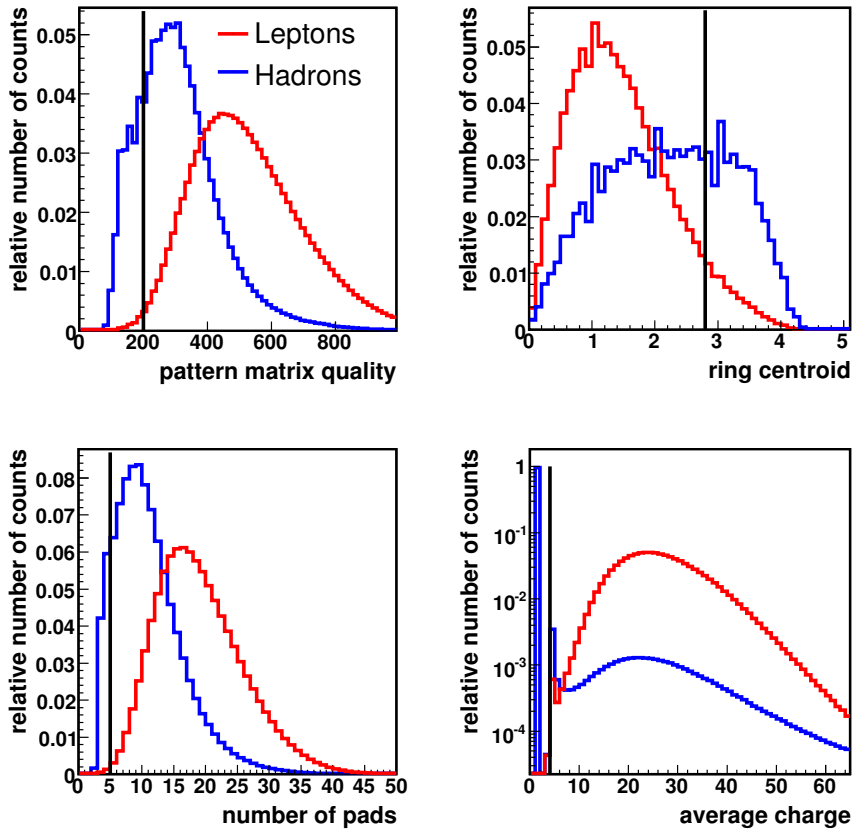


Figure 6.4.: Distributions of ring quality parameters for lepton (red solid line) and hadron (blue solid line) candidates. **Top left:** Pattern matrix quality. **Top right:** Ring centroid, i.e., the distance between a position of a ring centre of gravity and its fitted geometrical centre. **Bottom left:** The number of ring pads. **Bottom right:** Average charge per one fired pad. The black vertical solid lines represent the applied cuts. Data are from the Ar+KCl experiment.

<sup>1</sup>Ring centre of gravity is deduced from the charge deposition in pads.

## 6.2. Lepton identification in the Time of flight wall

Electrons and positrons which are produced in a heavy ion collision have velocities close to the speed of light. By means of measuring time of flight we may separate fast leptons from somewhat slower hadrons. Our particle identification algorithm requires that an electron/positron candidate has to have its velocity within certain limits given by the time resolution of TOF and TOFino, see Figure 6.5.

In TOF, I set the velocity limits at  $\pm 3$  standard deviations around the mean of the lepton peak. Lepton identification based on time of flight measured by TOFino had to take into account that due to a high hadron flux, individual TOFino paddles were often hit with more than one particle. In this case, TOFino provides for all hits going to the same paddle only one time measurement. Nevertheless, this time signal does not need to be induced by the fastest particle. We have to keep in mind that TOFino measures the time of flight plus some time interval, which scintillation light needs to propagate from the hit position to a photomultiplier, see Section 3.3.2. Thus, in the TOFino region, velocity could be constrained by the 3 sigma cut only from below. The velocity windows, which I applied, are shown in Figure 6.5.

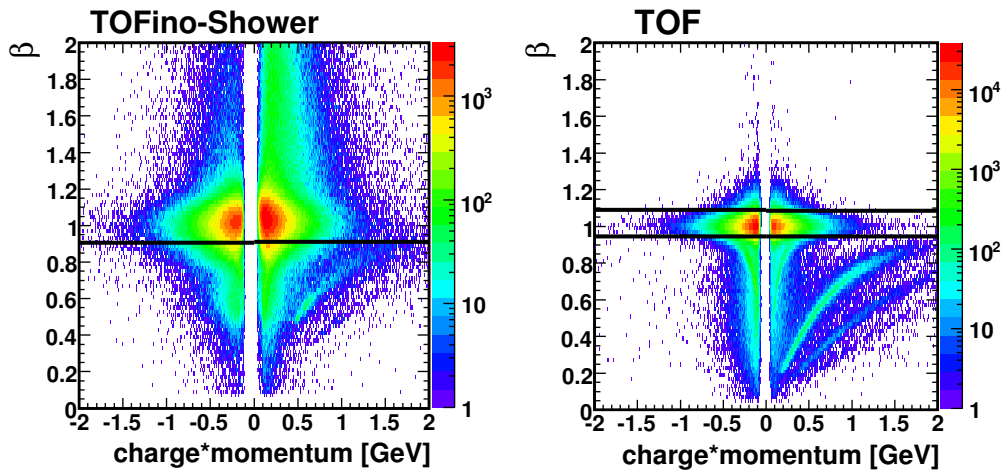


Figure 6.5.: Velocity ( $\beta = v/c$ ) versus charge times momentum distributions depicted for tracks which passed the constraints on RICH-inner MDC angular matching and ring quality. In the TOFino-Shower region, I required positive lepton signature in the Shower detector. **Left:** TOFino-Shower region. **Right:** TOF region. The black solid lines represent the applied cuts. Data are from the Ar+KCl experiment.

## 6.3. Lepton identification in Shower

The Shower detector improves lepton identification at low polar angles. An electron/positron penetrating through the two lead converter layers induces an electromagnetic shower. The Shower detector then measures charge amplification behind each layer. The number of the charged particles, which participate in showers initi-

## 6. Lepton analysis

ated by hadrons, is usually much smaller. Hence, charge amplification for hadrons is not as large as for electrons and positrons, see Figure 6.6.

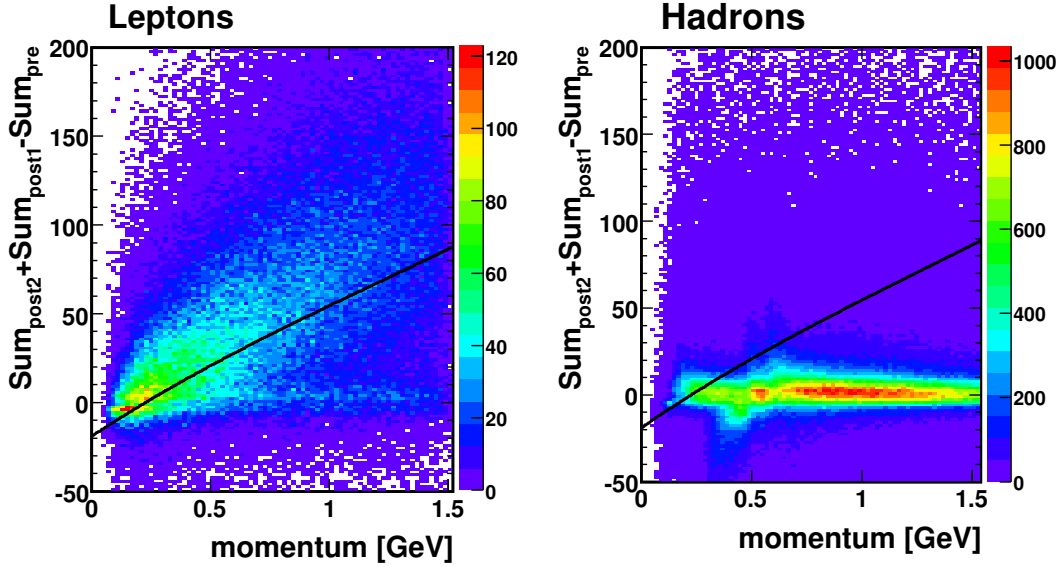


Figure 6.6.: Particle identification in the Shower detector. Figure shows a distribution of  $Sum_{post2} + Sum_{post1} - Sum_{pre}$  versus particle momentum for true leptons (**Left**) and for hadrons (**Right**). Data are from simulation. The black solid lines represent the momentum dependent Shower cut  $F_{thr} = F_{thr}(p)$  separating leptons from hadrons. See the text for further details.

Lepton identification in Shower is based on charges deposited in the pre-, post1-, and post2-converter chambers, see Section 3.4.

1. The algorithm searches for local maxima of collected charge in pre-converter chamber pads.
2. These pads are then considered to be in the centre of a larger  $3 \times 3$  pad area from where the charge is integrated, see Figure 6.7. Subsequently, charge integration is done also in post1- and in post2-converter pads at the same positions as in the pre-converter chamber.
3. Denoting the obtained values of collected charge from one  $3 \times 3$  pad area in the pre-, post1-, and post2-converter chambers by  $Sum_{pre}$ ,  $Sum_{post1}$ , and  $Sum_{post2}$ , respectively, a particle has the positive lepton signature in Shower when

$$Sum_{post2} + Sum_{post1} - Sum_{pre} \geq F_{thr}(p).$$

Here  $F_{thr}(p)$  is the momentum dependent threshold. Based on a simulation,  $F_{thr}(p)$  is parametrized by the third order polynomial in momentum

$$F_{thr}(p) = k_0 + k_1p + k_2p^2 + k_3p^3.$$

The constants  $k_i$  were tuned by our Shower experts in such a way that 80 % of leptons from a flat momentum generator should survive the Shower cut.

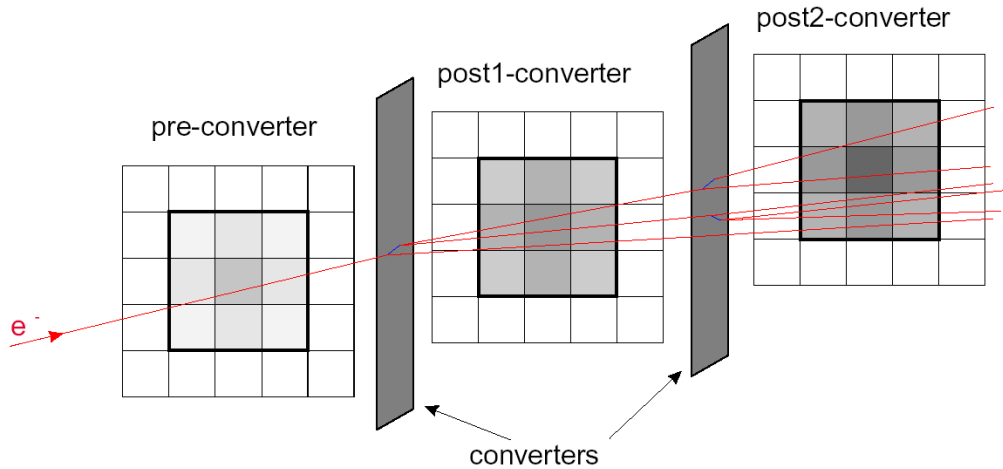


Figure 6.7.: Schema of  $e^-$  propagation through the Shower detector [72].

## 6.4. Track selection

The spectrometer does not measure the full trajectory of a particle. Tracks are assembled together from several pieces. For example, a hadron track candidate consists of an inner MDC track segment, an outer MDC track segment, and some corresponding hit in the Meta region. In addition to that, electron/positron candidates have assigned some ring candidate in RICH. The quality of matching between an inner and an outer MDC track segment is characterized by the so-called *Runge-Kutta quality parameter*  $\chi_{RK}^2$ . In my analysis, I used not much restrictive cut on  $\chi_{RK}^2 < 10000$ , which removes about 5 % of all tracks.

During the Ar+KCl run, the HADES set-up was not completed yet. In the sector 2 and 5, the last layer of MDCs was missing. Thus, in these two sections, our tracking algorithm had only one point behind the magnetic field at its disposal for a trajectory reconstruction. The number of trajectories which were reconstructed in these two sectors was, therefore, more sensitive to noise in MDCs. In the result, the sector 2 and 5 exhibited an enhanced multiplicity of identified lepton tracks with respect to other parts of the spectrometer.

In order to reduce the number of tracking fakes, I employed a constraint on matching of a lepton track with the Meta detectors, i.e., with TOF and Shower. Let us denote  $\Delta x$ ,  $\Delta y$ , and  $\Delta z$  distances in  $x$ ,  $y$ , and  $z$  directions between a lepton track extrapolated to the Meta region and a measured position of the corresponding hit in Meta. Distributions of  $\Delta x$ ,  $\Delta y$ , and  $\Delta z$  have a bell-like shape, see Figure 6.8 and Figure 6.9. For each combination of a sector, system (TOF, Shower), and coordinate  $(x, y, z)$ , the main peak of the distribution was fitted with a Gaussian. I set the limits of the cut windows at  $\pm 3$  standard deviations around the mean.

After I applied the cut on matching with the Meta detectors, the number of identified lepton tracks in the sector 2 and 5 reduced by about 20 %. In other sectors, the multiplicity of reconstructed trajectories stayed nearly unchanged, see

## 6. Lepton analysis

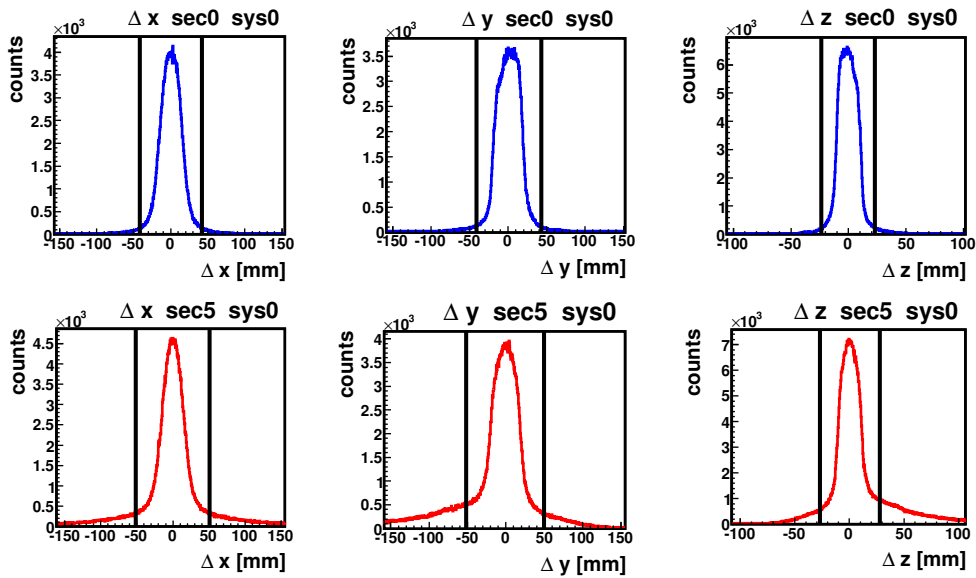


Figure 6.8.: Track matching to Shower (sys0). Distributions of  $\Delta x$ ,  $\Delta y$ , and  $\Delta z$  in a sector with four MDC layers (**Upper plots**) and in a sector with three MDC layers (**Lower plots**). The black vertical lines indicate my cuts. Data are from the experiment.

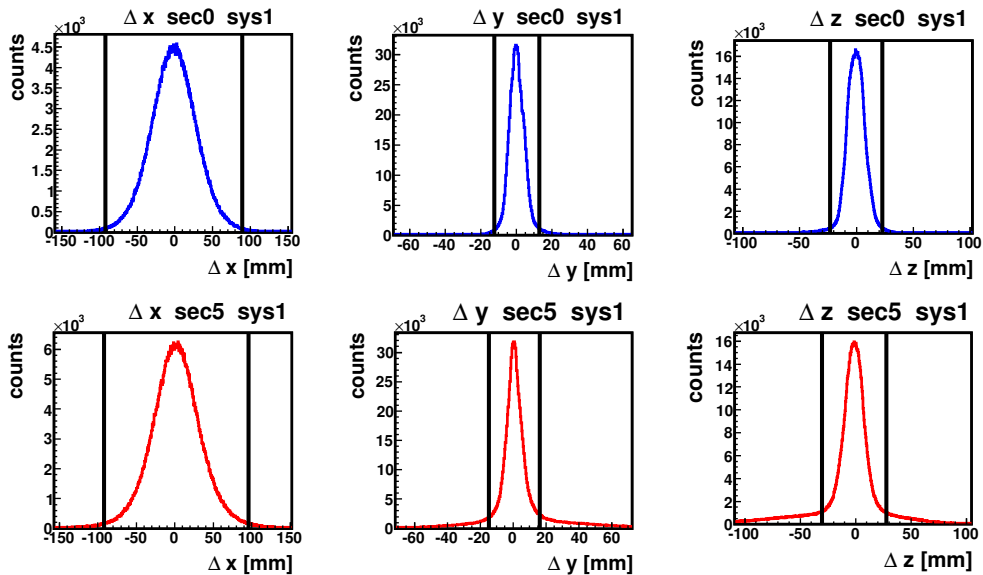


Figure 6.9.: Track matching to TOF (sys1). Distributions of  $\Delta x$ ,  $\Delta y$ , and  $\Delta z$  in a sector with four MDC layers (**Upper plots**) and in a sector with three MDC layers (**Lower plots**). The black vertical lines indicate my cuts. Data are from the experiment.

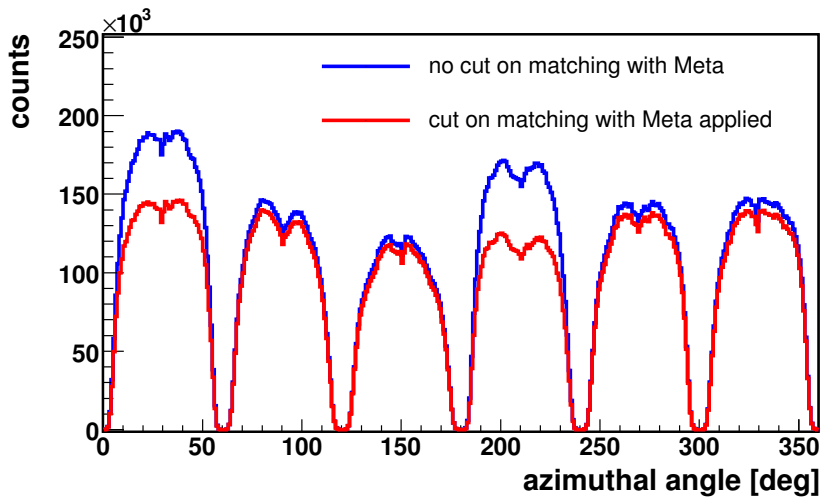


Figure 6.10.: Azimuthal angle distribution of identified leptons. The blue solid line corresponds to the original situation when no constraint on matching with the Meta detectors was applied. The red solid line shows the state after I employed the cut on matching to the Meta detectors. Data are from the experiment.

Figure 6.10. Altogether the cut removed cca 10 % of lepton tracks. Note that under this constraint the track multiplicity distribution in azimuthal angle symmetrizes. Remaining differences between individual sectors can be attributed to inefficiencies of our tracking system; namely to some dead MDC mother boards.

Finally, I had to remove ghost tracks which from time to time emerged in the events containing at least two identified leptons of the same polarity. Like-sign pairs appear in events quite rarely<sup>2</sup>, therefore the procedure, which I am going to describe, did not influence much distributions of single leptons. On the other hand, it affected the sample of the di-electrons with the same polarity emerging in the same event. These pairs are very important in the subsequent pair analysis, where they are used to estimate combinatorial background, see Section 7.2. If we would not remove the ghost tracks out of the sample of identified leptons, the combinatorial background would be probably determined incorrectly.

Recognition of a ghost track and its removing proceeds as follows. Our tracking algorithm can easily interpret a large hit cluster in MDC as two nearby segments and make two, or even more tracks out of it (ghost tracks). It happens quite frequently that real track and the corresponding ghost track have the same polarity, almost the same direction and size of a momentum, and that they share a hit in one or more HADES sub-detectors. The incidence histogram of different common hit combinations for like-sign lepton tracks appearing in the same event is depicted in Figure 6.11.

Strong correlation between momenta of same-event like-sign leptons was observed

<sup>2</sup>Before the ghost track cleaning procedure, about 8 % of events, which contained at least one identified lepton, contained also at least one identified like-sign pair. After the ghost tracks are removed, the share of events containing a like-sign pair reduces to about 0.83 %, see Figure 6.16.

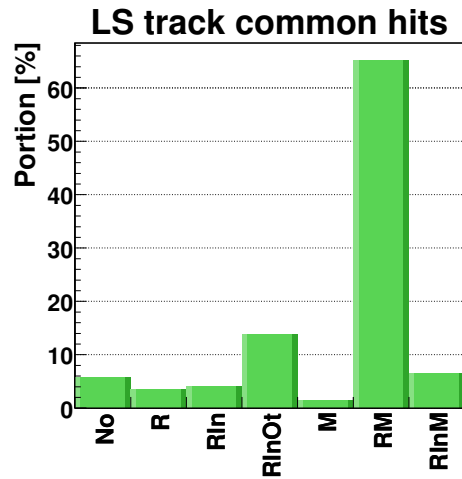


Figure 6.11.: Incidence histogram of common hits for reconstructed same-event like-sign lepton tracks. The group of like-sign tracks without any common hit is labelled “No”. Abbreviations “R”, “In”, “Ot”, and “M” denote a common hit in RICH, inner MDCs, outer MDCs, and the Meta region, respectively. Two tracks can share common hits in several sub-detectors at the same time, e.g., in the group named “RM”, like-sign lepton tracks have common hits in RICH and some Meta detector. Data are from the experiment.

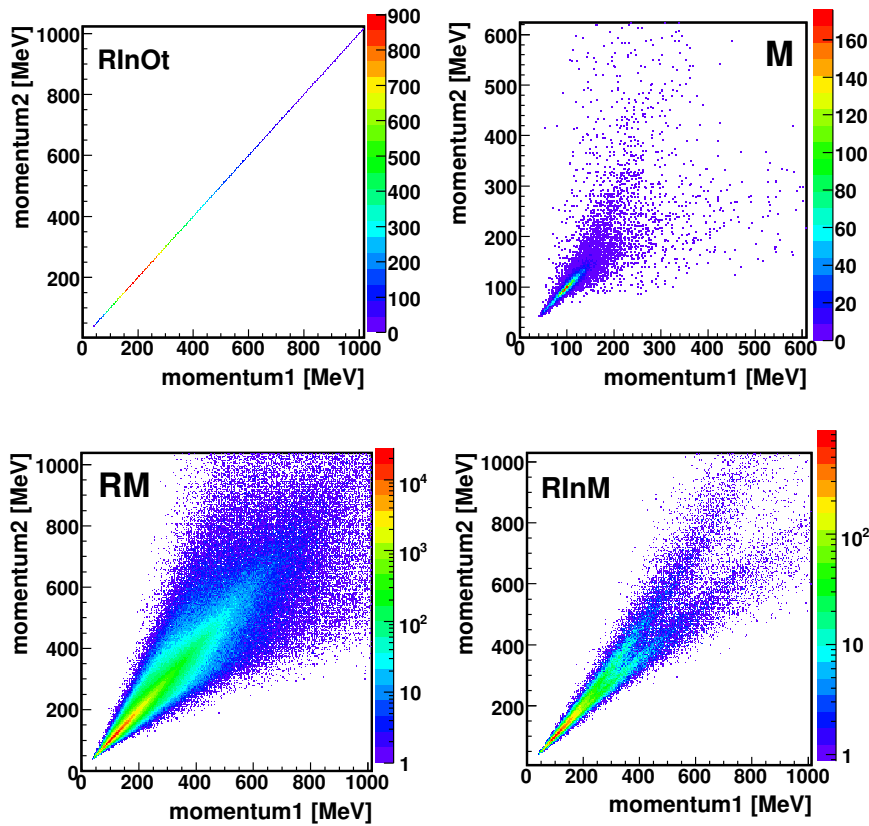


Figure 6.12.: Correlations between momentum sizes for the like-sign lepton tracks which share a hit in RICH “R”, inner MDCs “In”, outer MDCs “Ot”, or the Meta region “M”.

if the corresponding tracks shared a common hit

- in RICH, inner MDCs, and outer MDCs at the same time, or
- in some Meta detector (Shower or TOF). This common hit was eventually combined with other common hits in other sub-detectors at the same time.

In Figure 6.12, we may see correlations between momenta of the same-event like-sign leptons belonging to the groups mentioned above.

It was desirable to exclude the ghost tracks out of the analysis. Therefore, whenever I found that some same-event like-sign lepton tracks shared a common hit and belonged to one of the two groups mentioned above, I used in the analysis only the track which had the lowest value of the parameter

$$Q = \chi_{RK}^2 \sqrt{\frac{\Delta x^2}{\sigma_x^2} + \frac{\Delta y^2}{\sigma_y^2} + \frac{\Delta z^2}{\sigma_z^2}}.$$

Here  $\chi_{RK}^2$  stands for the Runge-Kutta quality parameter and  $\Delta i$ ,  $i = x, y, z$ , are distances between a hit position in some Meta detector and the corresponding extrapolated track crossing point with the Meta region. The variances of  $\Delta i$  distributions are denoted  $\sigma_i^2$ . This cut removed about 8 % of all lepton tracks.

## 6.5. Single lepton spectra

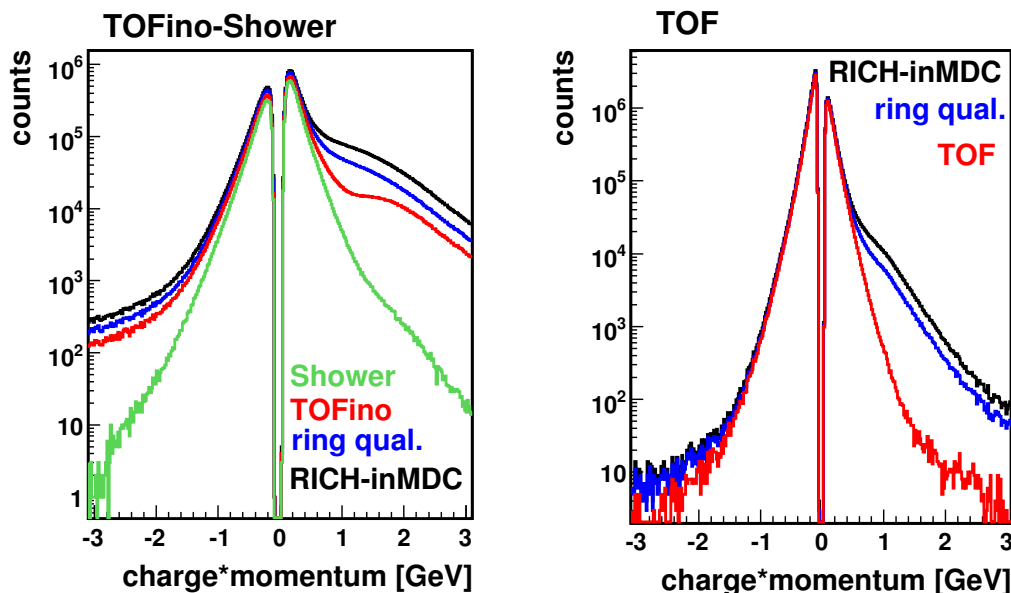


Figure 6.13.: Changes in charge times momentum distribution of lepton candidates under successive application of the hard cuts. **Left:** TOFino-Shower region. **Right:** TOF region. Data from the Ar+KCl experiment.

In Figure 6.13, I show how charge times momentum distribution of lepton candidates changes when the hard-cut constraints are applied one after another. Notice that after each cut the distribution gradually symmetrizes. Such behaviour indicates that fake leptons originating from protons are getting more and more suppressed. Yet for momenta above cca 1.1 GeV, hadron contamination of our lepton sample causes deviations from the steep exponential decrease of the spectrum. This is apparent mainly in the distribution of positrons in the TOFino-Shower region. Further suppression of this residual hadron contamination will be done in the subsequent pair analysis, see Section 7.3.

Cut	Positron candidates	Electron candidates
RICH-inner MDC matching	100 %	100 %
ring quality	85 %	93 %
velocity	70 %	84 %
Shower constraint	60 %	80 %

Table 6.1.: Percentage of lepton candidates which survived the hard-cut in question in the experiment. The starting point was the total number of the tracks which had matching between a RICH ring and an inner MDC track segment. On this sample of tracks I successively applied the hard-cuts.

Relative reduction of the initial number of lepton candidates under consecutive application of the hard-cuts can be seen in Table 6.1. The starting point was the number of the tracks which were assigned to a ring (tracks with RICH-inner MDC matching). The hard-cuts cause larger relative reduction in the positron sample than in the electron sample. We have to keep in mind that at the beginning, the positron sample was significantly contaminated by protons and deuterons. In addition to that, the magnetic field of the spectrometer has such a polarity that it bends positively charged particles towards the beam axis and negatively charged particles are curved away from this axis. Hence, electrons will end more probably in the TOF region, where we use efficient identification based on time of flight, while positrons will be more likely bended to the TOFino-Shower region, where they have to satisfy much more stiff Shower cut.

Now, let us compare how our UrQMD simulation reproduces shape of momentum and polar emission angle distributions of the identified leptons, see Figures 6.14 and 6.15. For this purpose, I generated and analyzed about 10 millions of LVL1 UrQMD events. While the shape of simulated and experimental distributions are the same, I have to scale down the result of the simulation by a constant factor. The reason is that in our simulation, the digitizers, which produce hits in corresponding detectors, overestimate internal efficiency of detectors for registering minimum ionizing particles, e.g., our electrons and positrons. Quality of the detector description in simulations was independently checked also by means of an analysis of charged pions and other hadrons. This analysis provided results which are consistent with the known experimental data [74].

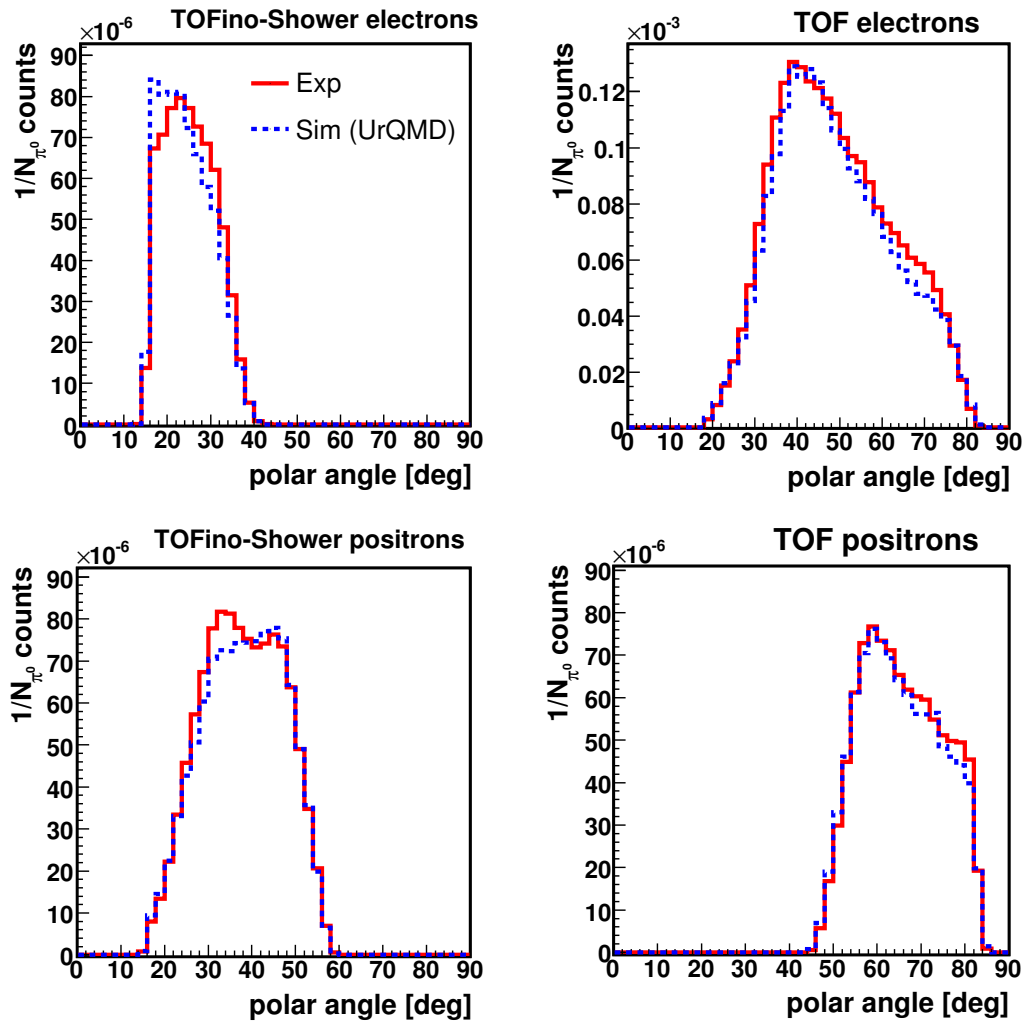


Figure 6.14.: Polar angle distribution of identified leptons within the momentum range 100–1100 MeV. Comparison between our experiment (red solid line) and the UrQMD simulation (blue dashed line). Distributions are normalized per one  $\pi^0$ . Simulated distributions were scaled down to sit on top of the experimental data.

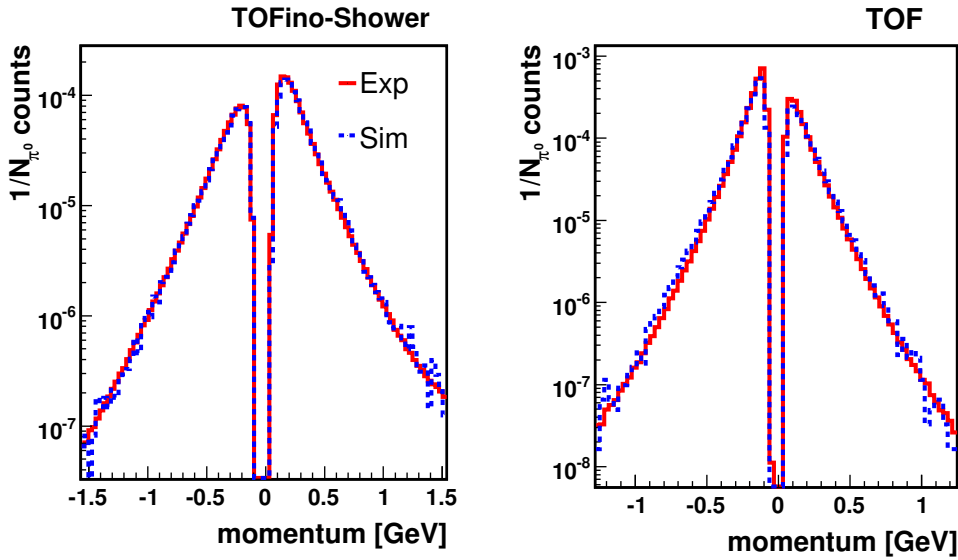


Figure 6.15.: Charge times momentum distribution of identified leptons. Comparison between the experiment (red solid line) and the UrQMD simulation (blue dashed line) is shown in the TOFino-Shower region (**Left**) and the TOF region (**Right**). Distributions are normalized per one  $\pi^0$ . Simulated distributions were scaled down to sit on top of the experimental data.

electron multiplicity			
2	<b>0.37 %</b>	<b>0.11 %</b>	<b>0.01 %</b>
1	<b>50.98 %</b>	<b>8.98 %</b>	<b>0.1 %</b>
0		<b>39.2 %</b>	<b>0.25 %</b>
	0	1	2
	positron multiplicity		

Figure 6.16.: Multiplicity of electrons versus multiplicity of positrons emerging in the same LVL1 event with the positive LVL2 trigger decision. It was required that each event should contain at least one identified lepton. The quoted numbers indicate the percentage of cases in which such events occurred.

In the Ar+KCl experiment, leptons were searched only in LVL1 events with the positive LVL2 trigger decision. About 81 % of these events contained at least one identified lepton, for more details see Section 6.7. This lepton was in cca 90.2 % of cases alone, see Figure 6.16. Only approximately 9.8 % of events had more than one identified lepton inside and, hence, they could be used in our pair analysis. Let

us also point out that a like-sign pair was produced only in about 0.83 % of cases. The transition from a single lepton to a pair analysis was, therefore, connected with a large reduction of event statistics.

## 6.6. Purity of the selected lepton sample

A usual way, how to check purity of a selected lepton sample, is based on simulations. This approach has the advantage that we know exactly which tracks identified as leptons are true leptons and which of them are misidentified hadrons. However, we have to be sure that our simulation is properly done and that the detector response to an incoming signal is as realistic as possible. This can be a problem if we have, e.g., some noisy channels in several sub-detectors. Fortunately, in our case, purity of the sample of identified leptons can be tested also with an alternative approach which I developed. Its main idea is based on event mixing of experimental data and I am going to discuss it in the next paragraph 6.6.1. In addition, results coming from simulations are shown and I will make a comparison of both approaches.

### 6.6.1. Fake ring-track matchings

I examined what portion of tracks identified as an electron/positron arises from an accidental combination of a good hadron track with a RICH ring. A hadron track which passes close enough to some ring can be matched to it creating thus a fake lepton candidate.

To see how frequent are fake ring-hadron track combinations in our sample of identified leptons, it is not necessary to rely on simulation, but we can employ directly experimental data. This approach has the unique advantage that all bad features of the HADES spectrometer, such as noisy pads in RICH, or missing wires in MDCs, will contribute realistically.

The following scenario was investigated. Fake ring-track combinations were created by merging RICH ring candidates from one LVL1 event with the positive LVL2 trigger decision with hadron tracks from several randomly selected LVL1 events with the negative LVL2 trigger decision. In order to combine only two comparable events, it was requested to have a similar number of tracks in both of them. Constraints on quality of a ring candidate were not strict at this step<sup>3</sup>. A ring candidate and a track were combined together if they fulfilled the same criteria which are applied in the usual HYDRA analysis, i.e., for each track, I selected the closest ring candidate within a broad, 10 deg wide, RICH-inner MDC matching windows. Afterwards, it was tested whether this combination of a track and a ring candidate survives the much more narrower momentum dependent RICH-inner MDC matching windows. The obtained sample of fake lepton candidates was then processed with the hard-cut analysis.

In Figure 6.17, it is shown how momentum times charge distributions of the created fake ring-track combinations change when our hard-cuts are applied on them.

<sup>3</sup>Algorithm required that the candidate should have its pattern matrix quality greater than 200.

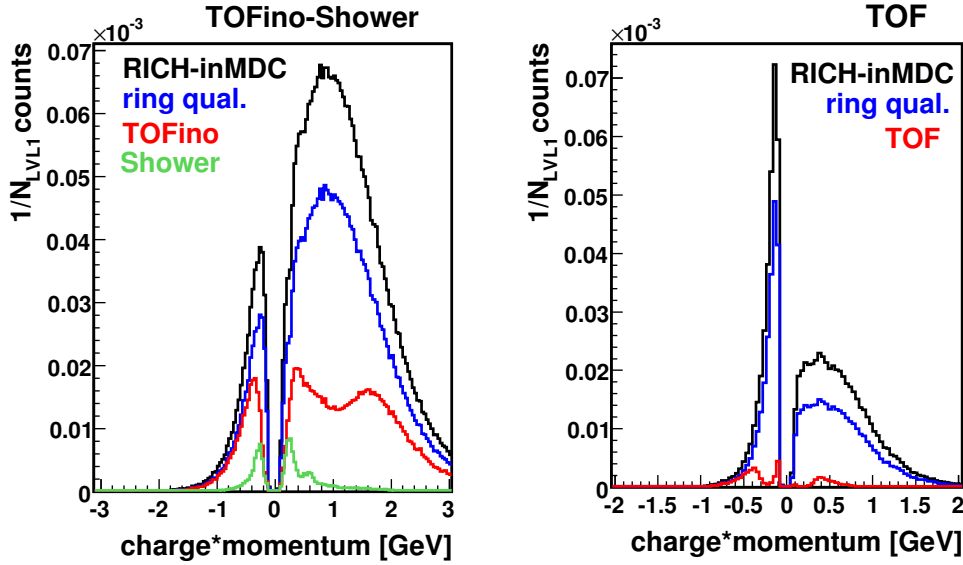


Figure 6.17.: Momentum times charge distribution of fake ring-track combinations. **Left:** TOFino-Shower region. **Right:** TOF region. Distributions are normalized per one LVL1 trigger event.

Situation in the TOFino-Shower and the TOF region is drawn separately. The major source of fakes at low momenta are charged pions. In the TOFino-Shower region, positively charged fakes create a long high momentum tail originating mainly from proton contamination. Momentum, at which protons start to be the dominant source of positron fakes in the TOFino-Shower region, is signaled by a small hump in the distribution. After all lepton hard-cuts are applied, the number of fake ring-hadron track combinations is reduced significantly, in the TOFino-Shower region by the factor 28.6 and in the TOF region by the factor 18.3.

To see what share of the identified leptons corresponds to fake ring-hadron track matchings, we have to contrast their charge times momentum distributions after all hard-cuts on lepton selection were applied. This is done in Figure 6.18. Both distributions are normalized per one LVL1 trigger event. Now, it is clearly visible that proton contamination is a significant problem in the TOFino-Shower region. Therefore, some upper cut on momentum size should be applied in the pair analysis. The lower plots show a ratio of both distributions. The presented plots suggest that up to the momentum 1.1 GeV, contamination with fake ring-hadron track combinations stays below 20 %.

Let us add two more remarks to the way how the absolute normalization of the obtained spectra of fakes was done. First, in the real experiment and in our event mixing procedure as well, lepton/ring candidates were searched only in LVL1 events with the positive LVL2 trigger decision. Therefore, it was possible to make the absolute normalization of the obtained spectra to one LVL1 trigger event in both cases in the same way. Second, as we combined each event with ring candidates with  $n$  other events together, the weight of each created fake was equal to  $1/n$ .

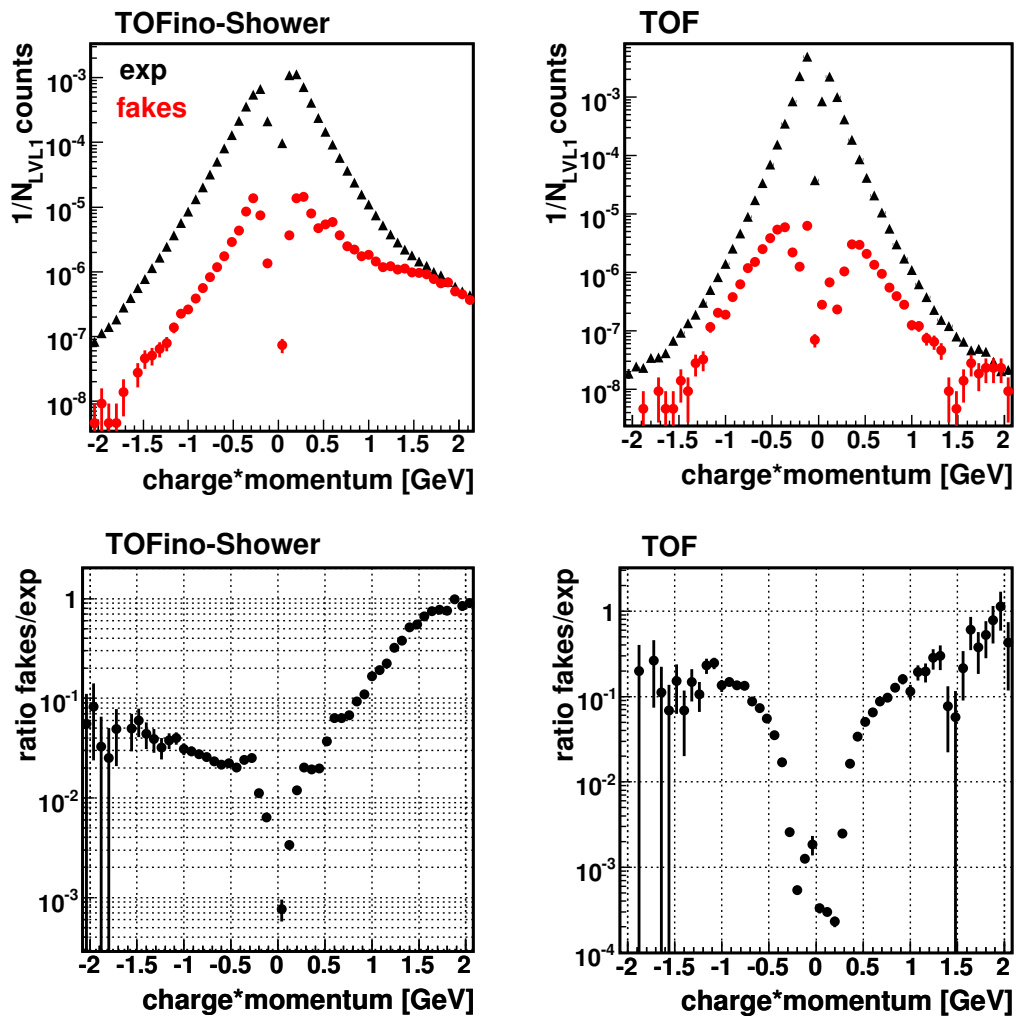


Figure 6.18.: **Upper plots:** Charge times momentum distribution of the identified leptons and the fake ring-hadron track combinations after all lepton hard-cuts were applied. Histograms are normalized per one LVL1 event. **Lower plots:** Share of fake ring-hadron track combinations in the sample of identified leptons. Situation in the TOFino-Shower region and in the TOF region is shown separately.

### 6.6.2. Purity of lepton sample in simulations

In the approach based on simulations, quality of the sample of identified leptons is usually expressed by means of two quantities, *purity* and *efficiency*. The purity  $\mathcal{P}$  is defined as the ratio of the number of true correctly identified leptons  $L_{cut}^{true}$  to the number of all identified leptons  $L_{cut}^{rec}$ ,

$$\mathcal{P} = \frac{L_{cut}^{true}}{L_{cut}^{rec}}.$$

Thus, the purity gives us the portion of properly identified leptons in our reconstructed lepton sample. The other quantity, the efficiency  $\mathcal{E}$ , tells us how effective our reconstruction algorithm is, i.e., what fraction of the original true leptons  $L_{cut0}^{true}$  will survive the applied hard-cuts, therefore

$$\mathcal{E} = \frac{L_{cut}^{true}}{L_{cut0}^{true}}. \quad (6.1)$$

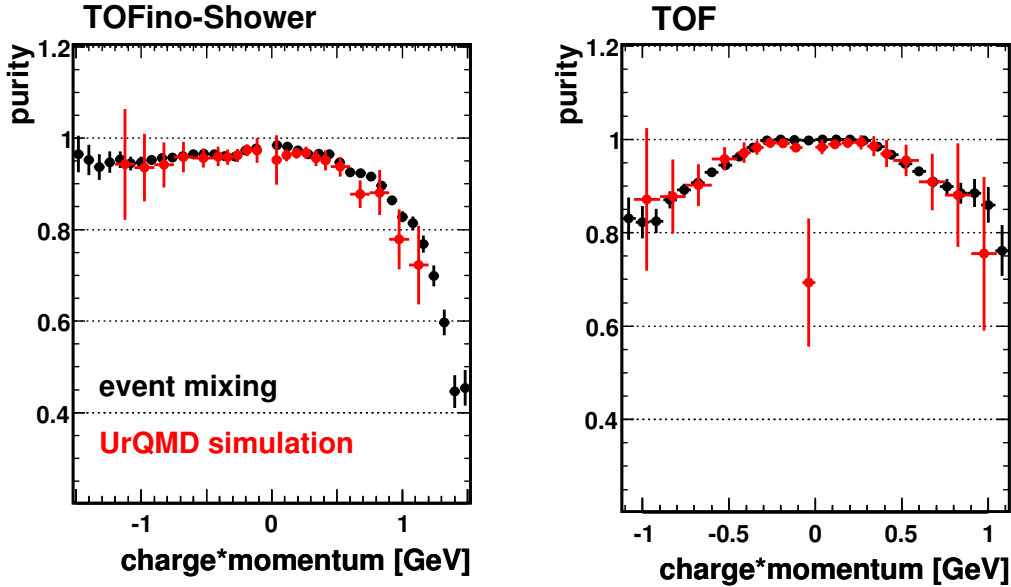


Figure 6.19.: Purity of the sample of identified leptons deduced from the UrQMD simulation (red points) and from the approach based on event mixing of experimental data (black points). **Left:** TOFino-Shower region. **Right:** TOF region.

The purity of our sample of identified leptons as a function of momentum is depicted in Figure 6.19. In the plot, I contrast the purity determined from simulations with the purity deduced from the event mixing method. In the latter case, the purity was estimated in the following way

$$\mathcal{P}_{exp} = \frac{L_{cut}^{rec} - L_{cut}^{fake}}{L_{cut}^{rec}},$$

where  $L_{cut}^{fake}$  is the number of fake ring-track matchings after all hard-cuts were applied. It can be seen that our simple experimental scenario provides predictions which are consistent with the results of the UrQMD simulation. Especially for higher momenta, mixing of a hadron track with a ring should be the main mechanism responsible for fake lepton production. Based on the UrQMD simulation, I deduced that the average purity of lepton sample in the TOFino-Shower region was about 95 % and in the TOF region approximately 98 %.

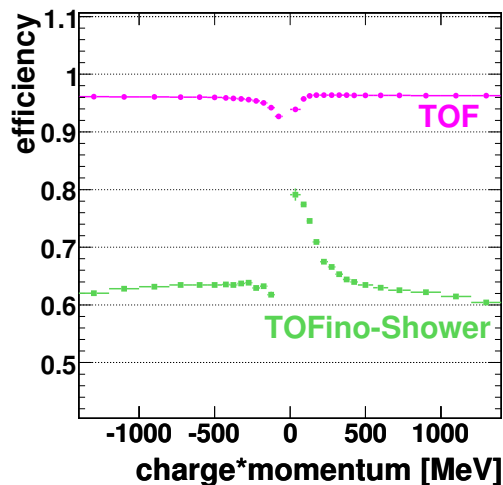


Figure 6.20.: Efficiency of lepton identification algorithm (hard-cut) deduced from simulation. Leptons were sampled from a uniform momentum and angular distribution and they were embedded into real events. Efficiency is shown separately for the TOFino-Shower and the TOF region.

The efficiency of the hard-cut lepton identification was estimated using simulated leptons (generated with a uniform momentum and angular generator) embedded into the real LVL1 events. LVL2 trigger decision was not regarded. Each event contained six embedded leptons, one per sector. Thus, the real events, which could possibly include also some admixture of real leptons, were considered just as a background for the simulated true electrons and positrons. In Equation (6.1), we defined the efficiency as the ratio of the number of true leptons after and before application of the hard-cuts. In our case,  $L_{cut0}^{true}$  denotes the number of the true embedded leptons, which survived the momentum dependent RICH-inner MDC matching windows, and  $L_{cut}^{true}$  stands for the number of the true embedded leptons, which passed through all the hard-cuts. In Figure 6.20, the efficiency is drawn as a function of lepton momentum. The average efficiency of lepton identification was about 65 % in the TOFino-Shower region and cca 95 % in the TOF region.

## 6.7. Single lepton LVL2 trigger efficiency

Ideally, a decision of the LVL2 trigger, which searches for lepton signatures in the HADES spectrometer, should not be dependent on lepton polarity and momentum. Selection efficiency of the LVL2 trigger can be examined by comparing a sample of leptons identified in the LVL1 events, which were stored without requiring the positive LVL2 trigger decision, and a sample of leptons recognized in the events with the positive LVL2 trigger decision. Electrons and positron were identified using the standard hard-cuts described above. The LVL2 trigger efficiency for selecting events with a lepton inside is then defined as

$$\varepsilon_{LVL2}^{lep} = \frac{n_{LVL2}^{lep}}{n_{LVL1}^{lep}(f_{DS} - 1)}.$$

Here  $n_{LVL2}^{lep}$  and  $n_{LVL1}^{lep}$  are the numbers of leptons identified in LVL2 events and in downsampled LVL1 events, respectively. As the number of events with the positive LVL1 trigger decision is downsampled and only every tenth event is stored,  $n_{LVL1}^{lep}$  has to be multiplied by a factor  $f_{DS} - 1$ , where  $f_{DS} = 10$ . Thus, we compare the proper number of leptons which are on the input to and on the output of the LVL2 trigger box. In Figure 6.21, I depicted efficiency of the LVL2 trigger as a function of lepton momentum and polar angle. The average LVL2 efficiency was about 0.81.

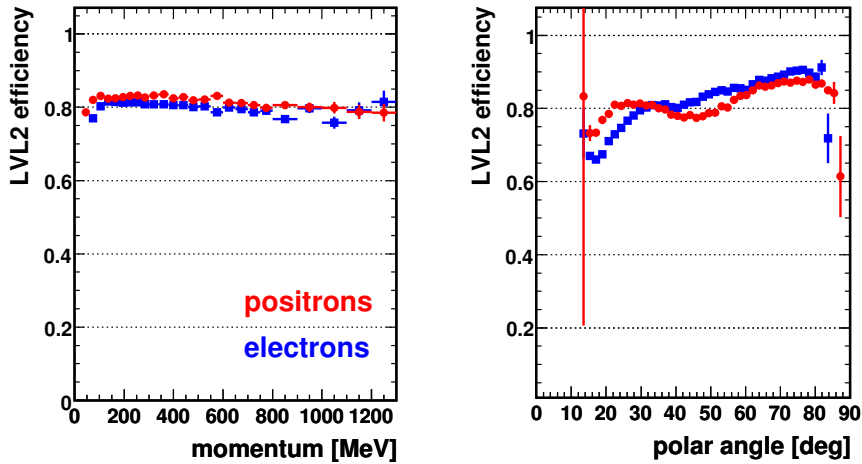


Figure 6.21.: Efficiency of the second level trigger for picking out events containing electrons and positrons. **Left:** LVL2 efficiency as a function of lepton momentum. **Right:** LVL2 efficiency as a function of polar angle. The blue and the red points correspond to identified electrons and positrons, respectively.

## 7 Pair analysis

The main goal of HADES is to measure invariant mass, transverse momentum, and rapidity spectra of electron-positron pairs produced in nucleus-nucleus collisions or elementary reactions. The invariant mass  $M_{12}$  of two particles is defined as follows

$$M_{12} = \sqrt{(P_1 + P_2)^2},$$

where  $P_i = (E_i, \vec{p}_i)$  denotes the four-momentum of the  $i$ -th particle. The Lorentz indices were not explicitly written down. In case of highly relativistic (anti)electron-(anti)electron pair, the electron rest mass can be neglected and the formula above simplifies to

$$M_{12} = 2\sqrt{p_1 p_2} \sin \frac{\alpha_{12}}{2}.$$

Here  $p_1$  and  $p_2$  are sizes of three-momentum vectors of the first and the second particle, respectively, and  $\alpha_{12}$  denotes their opening angle.

The dominant sources of electron-positron pairs in nucleus-nucleus collisions are

- $\gamma$  photon conversion and
- the Dalitz decay of the  $\pi^0$  meson, i.e.,  $\pi^0 \longrightarrow \gamma e^+ e^-$ .

These sources contribute mainly to the region of invariant masses below 150 MeV. Pairs with higher invariant masses originate from other processes, e.g.,

- the Dalitz decays  $\eta \longrightarrow \gamma e^+ e^-$ ,  $\omega \longrightarrow \pi^0 e^+ e^-$ ,  $\phi \longrightarrow \eta e^+ e^-$ ,
- the Dalitz decays of baryonic resonances  $\Delta$ ,  $N^* \longrightarrow N e^+ e^-$ ,
- direct decay of vector mesons  $\omega$ ,  $\rho$ ,  $\phi \longrightarrow e^+ e^-$ , and
- NN Bremsstrahlung.

In a real experiment, it is not possible to distinguish whether the reconstructed  $e^+ e^-$  pair originates from the same primary vertex or whether it is just an accidental combination of leptons from two separate processes. Combinations of leptons from different vertices form the so-called *combinatorial background*. The number of all different unlike-sign pairs from one event  $N_{+-}^{tot}$  can be decomposed into a *signal*<sup>1</sup>  $S_{+-}$  and a combinatorial background<sup>2</sup>  $B_{+-}$ ,

$$N_{+-}^{tot} = S_{+-} + B_{+-}.$$

In order to extract the signal component from the measured pair spectra, we have to assess the contribution of the combinatorial background. Fortunately, there are well established analysis methods which enable us to do this. These methods use

<sup>1</sup>Electron-positron pairs coming from the same primary decay vertex, carrying thus physically interesting information.

<sup>2</sup>Accidental unlike-sign lepton combinations without any physical content.

either like-sign pairs emerging from the same event or unlike-sign pairs obtained from event mixing. We will refer to these approaches in more detail in Section 7.2.

The main problem of the pair analysis lies in a rapid growth of the combinatorial background with the increasing number of electrons and positrons in one event. Distributions corresponding to the signal are then obtained as a difference of two close distributions  $N_{+-}^{tot}$  and  $B_{+-}$ . The presence of a strong trivial source in our pair sample such as conversion would immensely increase the combinatorial background and thus smear the shape of invariant mass spectrum in the physically interesting region of high invariant masses. Therefore, one of the key tasks of the pair analysis is to suppress the contribution coming from photon conversion. In the vast number of cases, photons originate from  $\pi^0$  decay. They may convert in the target, the RICH radiator, or the RICH carbon shell. Fortunately, conversion pairs have usually small opening angles, so cut on a pair opening angle can reduce this contribution significantly.

### 7.1. Pair Background

In a real experiment, composition of the background is a little bit more complicated. We have to keep in mind that besides the true identified electrons and positrons, the lepton sample contains also misidentified hadrons and tracking fakes. Thus, pairs forming our background can be divided into two groups:

1. *true combinatorial background pairs*, i.e., both particles are true leptons, and
2. *fake pairs* - pairs, where one or both particles are fake leptons.

The group of the true combinatorial background pairs can be further split into:

- *true uncorrelated combinatorial background pairs* - electron and positron emerge from different vertices and have different initial sources, and
- *true correlated combinatorial background pairs* - though electron and positron come from different vertices they still originate from a decay of the same grandmother particle. Due to the laws of energy and momentum conservation they are not completely independent.

Fake pairs emerge from:

- *misidentified hadrons*, and
- *tracking fakes* - fake leptons arising from accidental combinations of parts of tracks created by different particles.

### 7.2. Reconstruction of combinatorial background

There are two methods which allow us to reconstruct contribution of the true combinatorial background. And as it is natural, each of them has its advantages and

disadvantages. However, the best result is obtained when they are combined together.

The first method is based on creating *same-event like-sign pairs*. These pairs cannot originate from the same vertex. Assuming that a probability to detect some number of leptons has a character of a binomial distribution and that multiplicities of electrons and positrons in one event are Poisson-like distributed, it can be shown [75] that

$$B_{+-}^{same} = 2\sqrt{N_{++}N_{--}}.$$

Here  $N_{++}$  and  $N_{--}$  are the numbers of  $e^+e^+$  and  $e^-e^-$  pairs which emerged from the same event, respectively. The formula above assumes the same efficiency for electron and positron detection, but it can be generalized even for the case when they are non-equal, for further details see [75]. In my analysis, the non-equal electron and positron detection efficiencies are incorporated by means of the efficiency correction discussed in Section 7.5. The background obtained from the same-event like-sign pairs is properly normalized and it can even reproduce the correlated background. Nevertheless, a significant disadvantage of this method lies in a limited number of events, where two leptons with the same polarity appear.

Contribution of the combinatorial background can be also assessed using the *event mixing* technique. It makes unlike-sign pair combinations from electrons and positrons coming from two different events. These pairs are not correlated by definition. As this approach merges two events into one event, it is desirable to mix only two similar reactions, e.g., with comparable centrality and with leptons originating from the same target region. This method is able to provide big statistics of combinatorial background pairs, because a large number of events, which can be combined together, is available. However, it misses the natural normalization and it is not able to reconstruct the correlated combinatorial background at low invariant masses.

Both methods are thus often merged together. The same-event like-sign background is used at low invariant mass region, where contribution from the correlated background is more pronounced and where the number of like-sign pairs is sufficient. In high invariant mass region, combinatorial background is estimated with the event mixing method which has to be normalized to the same-event like-sign background in some interval.

## 7.3. Background rejection

Before I started with combinatorial background and signal reconstruction, it was requisite to suppress contributions coming from conversion and fake pairs. The goal is to achieve a signal with the best physical significance. The background rejection thus represents one of the important points of the whole di-lepton analysis.

The conversion contribution is suppressed by the *opening angle cut*. The left-hand side plot in Figure 7.1 shows opening angle distributions of electron-positron pairs coming from a decay of different sources. Di-leptons originating from conversion of a photon have typically very small opening angles. Our Pluto simulation suggests

## 7. Pair analysis

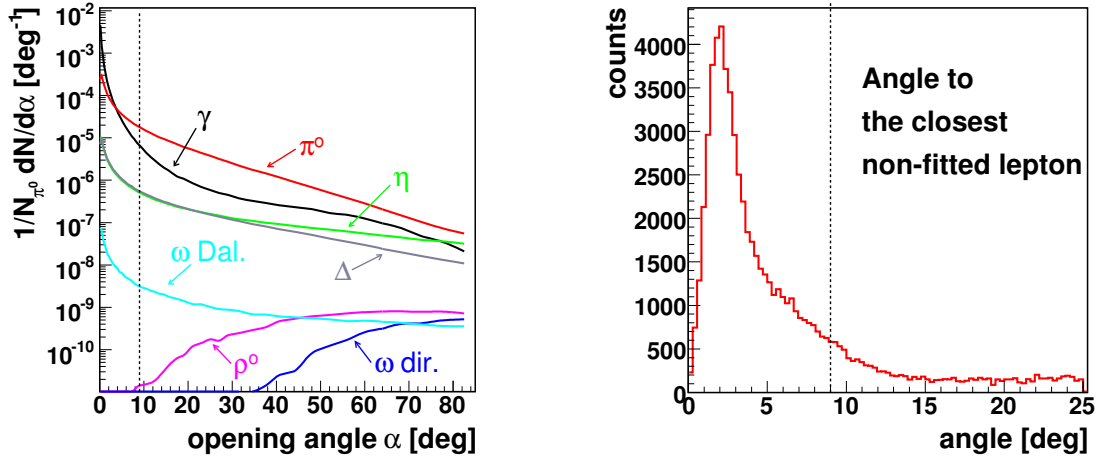


Figure 7.1.: **Left:** Opening angle of  $e^+e^-$  pairs coming from various sources. Data are based on our Pluto simulation. The dotted vertical black line indicates the opening angle of 9 deg. **Right:** Angle to the closest non-fitted lepton. The vertical line represents our cut on 9 deg.

that the conversion contribution will be significantly suppressed when we select only the pairs with opening angles larger than 9 deg. If a pair did not survive the 9 deg opening angle cut in my analysis, then both legs forming the pair were removed from the lepton sample. This means that all pairs which contained one of these legs were also not used in the further analysis. Unfortunately, the opening angle cut affects also yields from other sources, e.g.,  $\pi^0$ ,  $\eta$ , or  $\omega$  Dalitz decays. Based on the Pluto simulation, I estimated losses of their contribution to the signal, see Table 7.1.

Cut	$\gamma_{conv}$		$\pi_{Dalitz}^0$		$\eta_{Dalitz}$		$\Delta_{Dalitz}$		$\omega_{Dalitz}$	
		[%]		[%]		[%]		[%]		[%]
No cut	73200	100	35300	100	2020	100	1660	100	16.8	100
OA cut	405	0.55	8870	25	934	46	644	39	8.50	51

Table 7.1.: The number of pairs coming from various Dalitz sources. The row “No cut” corresponds to the situation when no pair cut was applied. The number of pairs, after the 9 deg opening angle cut was used, is shown in the row “OA cut”. Data based on our Pluto.

It often happens that one of the legs of a conversion pair has a small momentum and the strong magnetic field bends it out of the spectrometer. In this case, the lepton leaves a ring in RICH and a connected track segment only in inner MDCs. However, the second leg of such a pair can be a well-defined lepton track which will be used for pairing. To exclude these tracks from the sample, I also checked, if an opening angle between each leg of a pair and track segments from inner MDC, pointing to some RICH ring, is greater than 9 deg, see the right-hand side plot in Figure 7.1. This cut is called *cut on angle with the closest non-fitted lepton*. In principle, the cut removes from the lepton sample single tracks which have some non-fitted lepton closer than 9 deg.

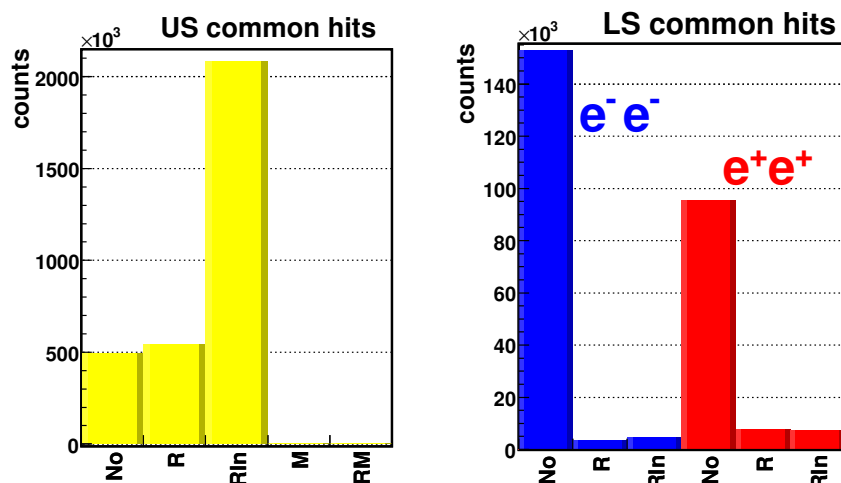


Figure 7.2.: Incidence of common hits for unlike-sign pairs (**Left**) and like-sign pairs (**Right**). Both plots show the situation before any cut on the pair level was applied. The number of pairs which do not share any common hit is written in the column “No”. The column “R” corresponds to the case when pair legs had a common hit in RICH, the column “RIn” to the case when leptons had common hits in RICH and inner MDCs at the same time, and the column “M” to the case when leptons shared a common hit in TOF or in Shower. Unlike-sign pairs are dominated by the close pairs from conversion and Dalitz decays. Since the region of RICH and inner MDCs is free of magnetic field, close pairs have a large probability to have a common hit in RICH or inner MDCs. Hence, unlike-sign pairs mostly belong to the group “RIn” or “R”. On the other hand, like-sign pairs should be produced spatially uncorrelated with a minimum of common hits. The like-sign tracks sharing a hit in inner MDCs, outer MDCs, and in the Meta region at the same time, or a Meta hit eventually combined with some other common hits at the same time, were already removed by the procedure discussed in Section 6.4.

Further, I applied the so-called *no double hit cut*. It removes those pairs which share a common hit in any of the sub-detectors (RICH, MDC, Meta). This cut should suppress contributions of tracking fakes and close conversion pairs. Incidences of different common hit combinations are shown in Figure 7.2. In Section 6.4, we pointed out that for certain classes of common hit combinations, same-event like-sign leptons exhibited correlation in their momenta (ghost tracks). This feature is still manifest for the like-sign tracks which have a common hit in RICH and, to somewhat lesser extent, it is apparent also for tracks sharing a common hit in RICH and in inner MDCs at the same time, see Figure 7.3. Nevertheless, apart from the correlated component both plots prove also a strong uncorrelated ingredient, which may come from, e.g., accidental matching of a ring with a hadron track. Separation of both components would require more detail information about the number of MDC wires which were used for track reconstruction. As this piece of information was not available in our ntuple, I decided to remove all such tracks with this cut. Like in the case of the 9 deg opening angle cut, when a pair does not survive the *no double hit cut* then both legs forming the pair are removed from the lepton sample

and they cannot be contained in other pairs.

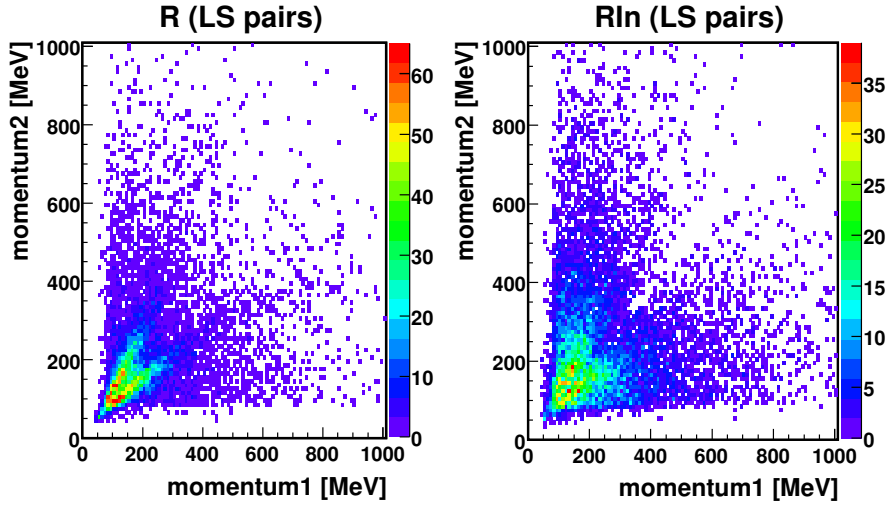


Figure 7.3.: Momentum of the first leg versus momentum of the second leg of a like-sign pair. **Left:** A common hit was only in RICH. **Right:** Common hits were in RICH and in inner MDCs at the same time. Both plots show the situation before any cut on the pair level was applied.

As it was shown in Section 6.6.2, hadron contamination of our lepton sample grows significantly with increasing momentum. It exceeds tolerable level above 1100 MeV. Hence, in my analysis, I required that both particles forming a pair have to have their momentum size smaller than 1100 MeV. Our Pluto simulation predicts that this cut causes 9 % loss in the yield from the direct  $\omega$  decay.

The last cut which I used was the 100 MeV cut on momentum size of leptons from below. The cut further reduces the contribution coming from conversion. The Pluto simulation suggests that conversion pairs should be suppressed by this constraint 2 times and the yield from the  $\pi^0$  Dalitz decay should lower by 30 %. Other sources are effected by this cut on a level of 10–20 %.

Figure 7.4 shows how the pair cuts, when successively applied, change the invariant mass distribution of the all same-event unlike-sign pairs, the combinatorial background, the signal, and the signal to background ratio. The order in which the pair cuts were employed was the following:

1. pair opening angle  $> 9$  deg,
2. cut on no double hit + cut 1,
3. lepton momentum size is in the range  $100 < p < 1100$  MeV + cut 2,
4. angle with the closest non-fitted lepton  $> 9$  deg + cut 3.

Let us point out that the sequence of the pair cuts affects strongly the invariant mass distributions of the all same-event unlike-sign pairs and the combinatorial background. On the other hand, the applied constraints do not change much the high mass tail of the signal, see also Table 7.2. In the region of small invariant

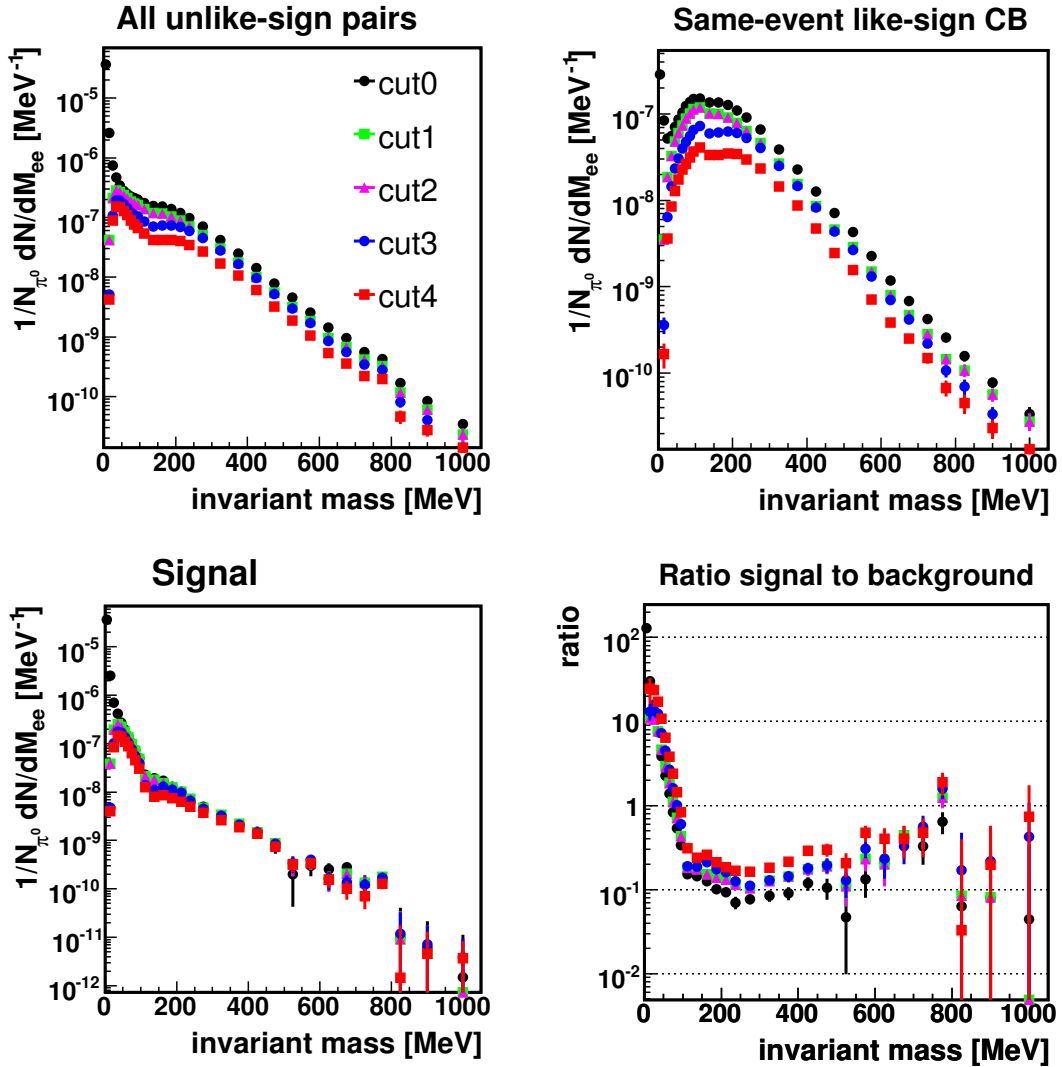


Figure 7.4.: Invariant mass distributions of all same-event unlike-sign pairs (**Top left**), same-event like-sign combinatorial background (**Top right**), signal (**Bottom left**), and signal to background ratio (**Bottom right**). It is shown how these distributions modify when pair cuts are applied one after another. cut0 - no cut was applied, cut1 - pair opening angle is larger than 9 deg, cut2 - pair legs do not share a common hit + cut1, cut3 - size of lepton momentum is limited from 100 to 1100 MeV + cut2, and cut4 - opening angle with the closest non-fitted lepton is larger than 9 deg + cut3. Let us point out that just below the mass 800 MeV, the signal exhibits a hint of the  $\omega$  peak. All invariant mass distributions were normalized per one  $\pi^0$ .

## 7. Pair analysis

Signal pairs:

Cut	Low masses		Medium masses		High masses	
	$[\times 10^4]$	[%]	$[\times 10^4]$	[%]	$[\times 10^2]$	[%]
0	284	100	1.24	100	3.9	100
1	9.21	3.2	1.23	99	3.5	90
2	9.13	3.2	1.23	99	3.5	90
3	6.40	2.2	1.12	90	3.5	90
4	5.24	1.8	0.84	67	2.8	71

Combinatorial background pairs:

Cut	Low masses		Medium masses		High masses	
	$[\times 10^4]$	[%]	$[\times 10^4]$	[%]	$[\times 10^2]$	[%]
0	12.8	100	13.2	100	17.9	100
1	7.52	58	9.36	71	12.0	67
2	7.52	58	9.36	71	12.0	67
3	4.23	32	7.37	55	10.0	56
4	2.38	18	4.18	31	5.7	32

Table 7.2.: Reduction of the number of signal and combinatorial background pairs when the pair cuts are applied successively. The invariant mass spectrum is divided into three regions: low pair masses ( $M_{ee} < 150$  MeV), medium pair masses ( $150 < M_{ee} < 550$  MeV), and high pair masses ( $550 \text{ MeV} < M_{ee}$ ). Ordering of the cuts used in tables follows the convention employed in the text. The cut 0 means that no pair cut was applied. Data are from the experiment.

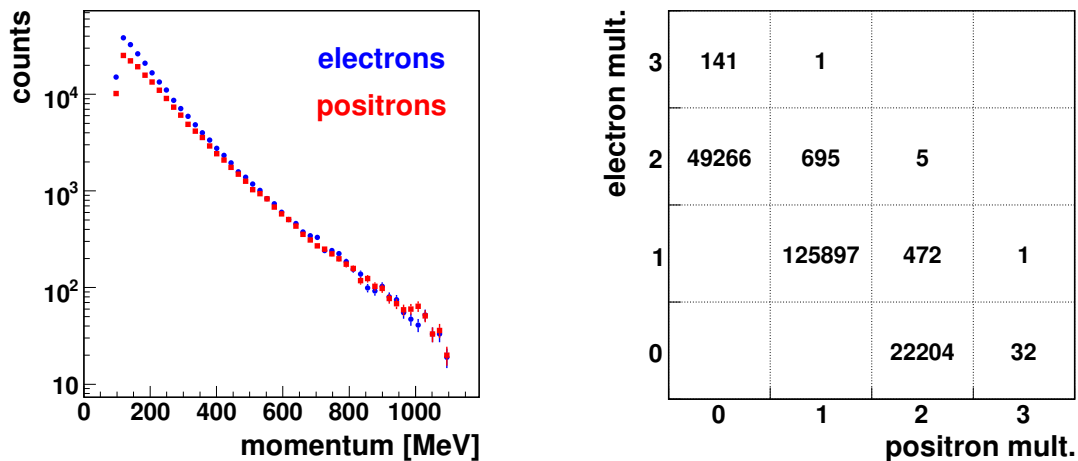


Figure 7.5.: **Left:** Momentum distribution of electrons and positrons after all pair cuts were applied. **Right:** Multiplicities of electrons and positrons in events containing at least one identified pair after all pair cuts were applied.

masses, the signal is reduced mainly by the opening angle cut which removes close pairs. Cut by cut, the signal to background ratio increases gradually and, finally, it reaches a value of about two in the  $\omega$  pole mass region.

Electrons and positrons, which survived all pair cuts, have symmetric high momentum tails of their momentum distributions, not revealing any proton contamination of the positron sample, see the left-hand side plot in Figure 7.5. The multiplicity distribution of electrons and positrons in events containing at least one identified pair is shown in the right-hand side plot in Figure 7.5.

## 7.4. Mixed-event background

The event mixing technique is able to provide a reliable shape of the combinatorial background only when leptons, which are combined together, originate from two similar reactions. Therefore, I divided my sample of the events, containing at least one identified lepton pair after all pair cuts, into eight reaction classes. The events were sorted according to position of their target  $z$ -vertex coordinate (4 bins) and track multiplicity (2 bins), see Figure 7.6. The reaction classes which I used for construction of the mixed-event background are specified in Table 7.3. Statistics of events in all the classes was more or less the same.

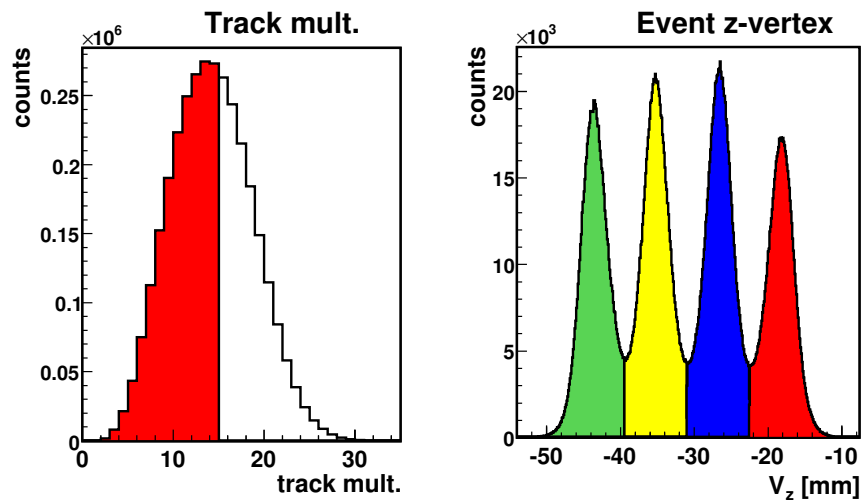


Figure 7.6.: Binning which was used for mixed-event background reconstruction. **Left:** Distribution of track multiplicity. **Right:** Distribution of event  $z$ -vertex coordinate. Individual bins are indicated by different colours.

By way of illustration, in Figure 7.7, I contrast the same-event like-sign background and the mixed-event background in each of the eight reaction classes. Scaling of the mixed-event to the like-sign background was done on the interval 150–650 MeV. The small hump, which appears at around 100 MeV in the same-event like-sign background, originates from the correlated combinatorial background. This structure is not reproduced with the event mixing technique.

## 7. Pair analysis

Class	0	1	2	3	4	5	6	7
$M_{trk}^L$	0	0	0	0	14	14	14	14
$M_{trk}^U$	14	14	14	14	100	100	100	100
$V_z^L$ [mm]	-52.0	-39.5	-31.0	-22.5	-52.0	-39.5	-31.0	-22.5
$V_z^U$ [mm]	-39.5	-31.0	-22.5	-9.0	-39.5	-31.0	-22.5	-9.0

Table 7.3.: Reaction classes which were used for creation of the mixed-event combinatorial background.  $M_{trk}^L$  and  $M_{trk}^U$  stand for the lower and the upper limit of track multiplicity, respectively,  $M_{trk}^L < \text{track mult.} \leq M_{trk}^U$ .  $V_z^L$  and  $V_z^U$  are the lower and the upper boundary of the event  $z$ -vertex coordinate,  $V_z^L \leq V_z < V_z^U$ .

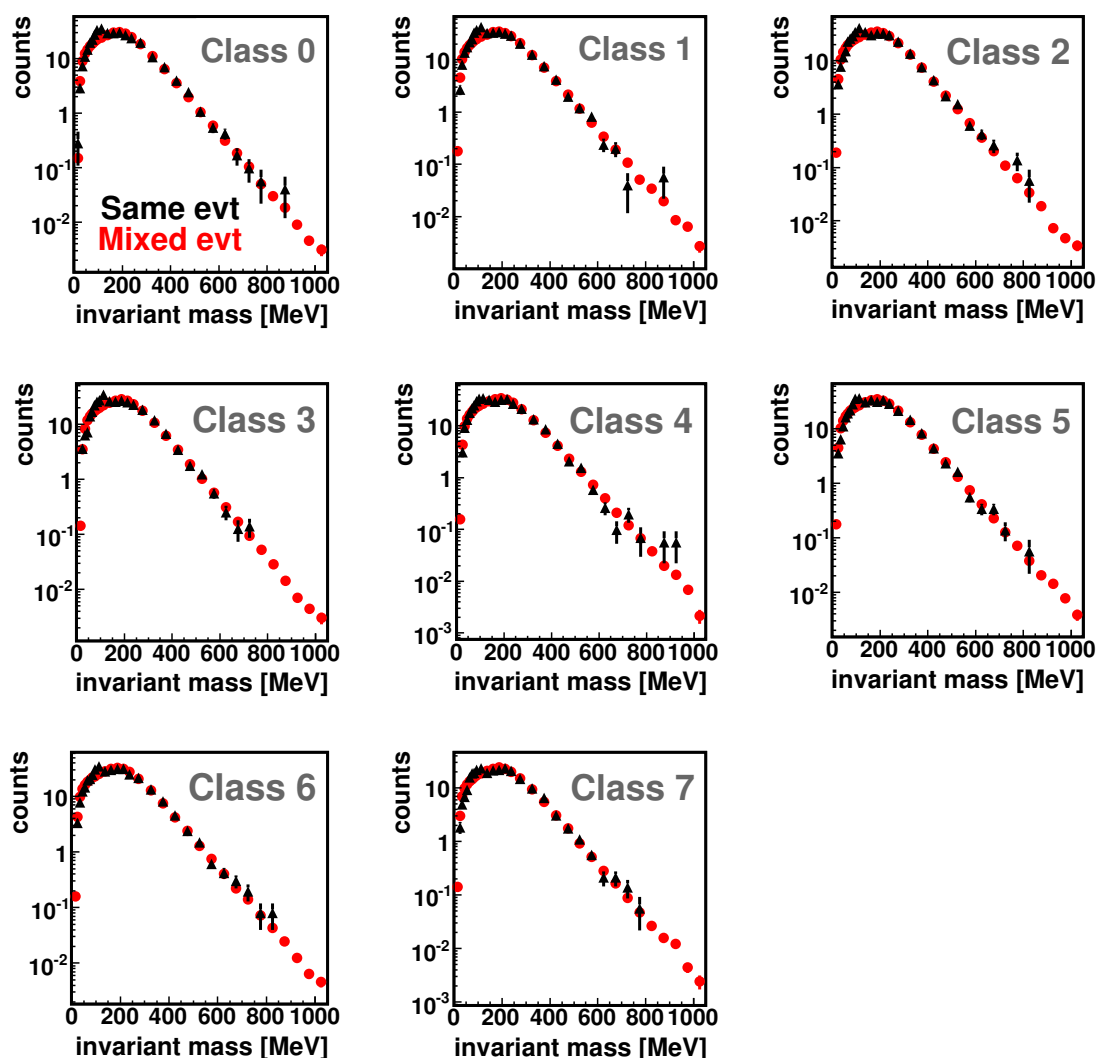


Figure 7.7.: Comparison of the same-event like-sign background (black points) and the properly scaled mixed-event background (red points) in each of the eight reaction classes.

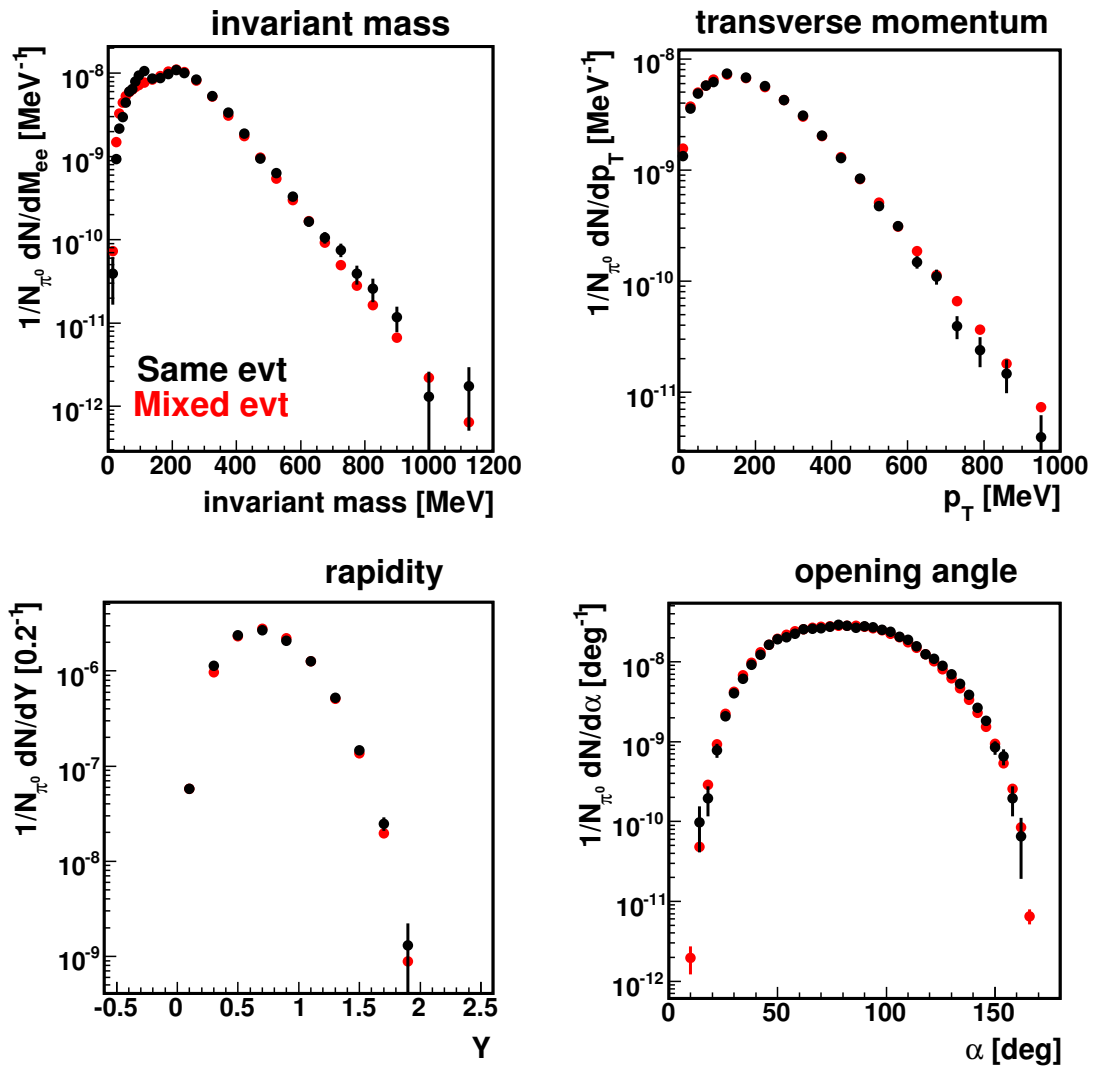


Figure 7.8.: Comparison of the same-event (black points) and the mixed-event (red points) invariant mass, transverse momentum, rapidity, and opening angle spectra of  $e^+e^+$  pairs. All distributions are normalized per one neutral pion.

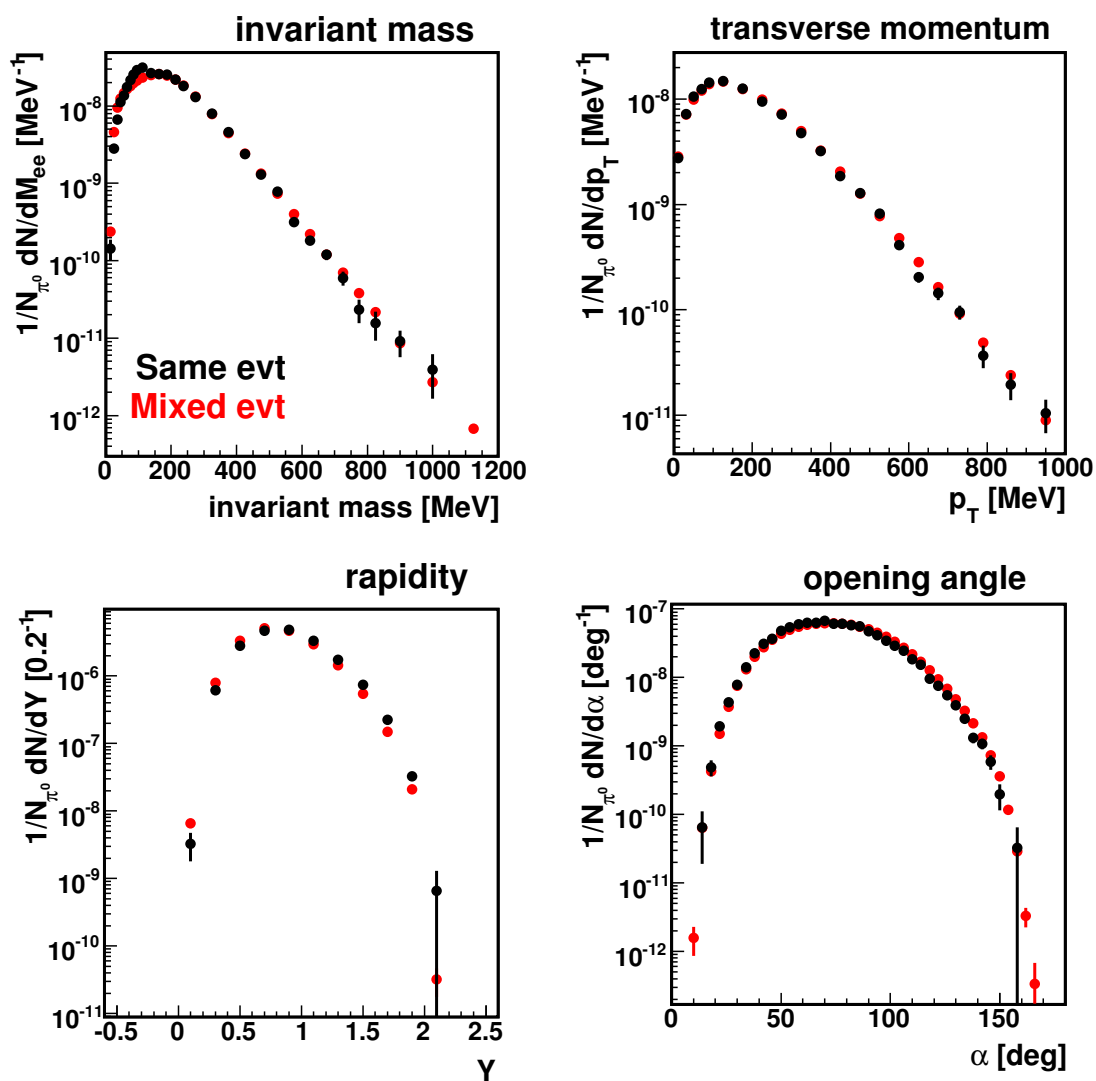


Figure 7.9.: Comparison of the same-event (black points) and the mixed-event (red points) invariant mass, transverse momentum, rapidity, and opening angle spectra of  $e^-e^-$  pairs. All distributions are normalized per one neutral pion.

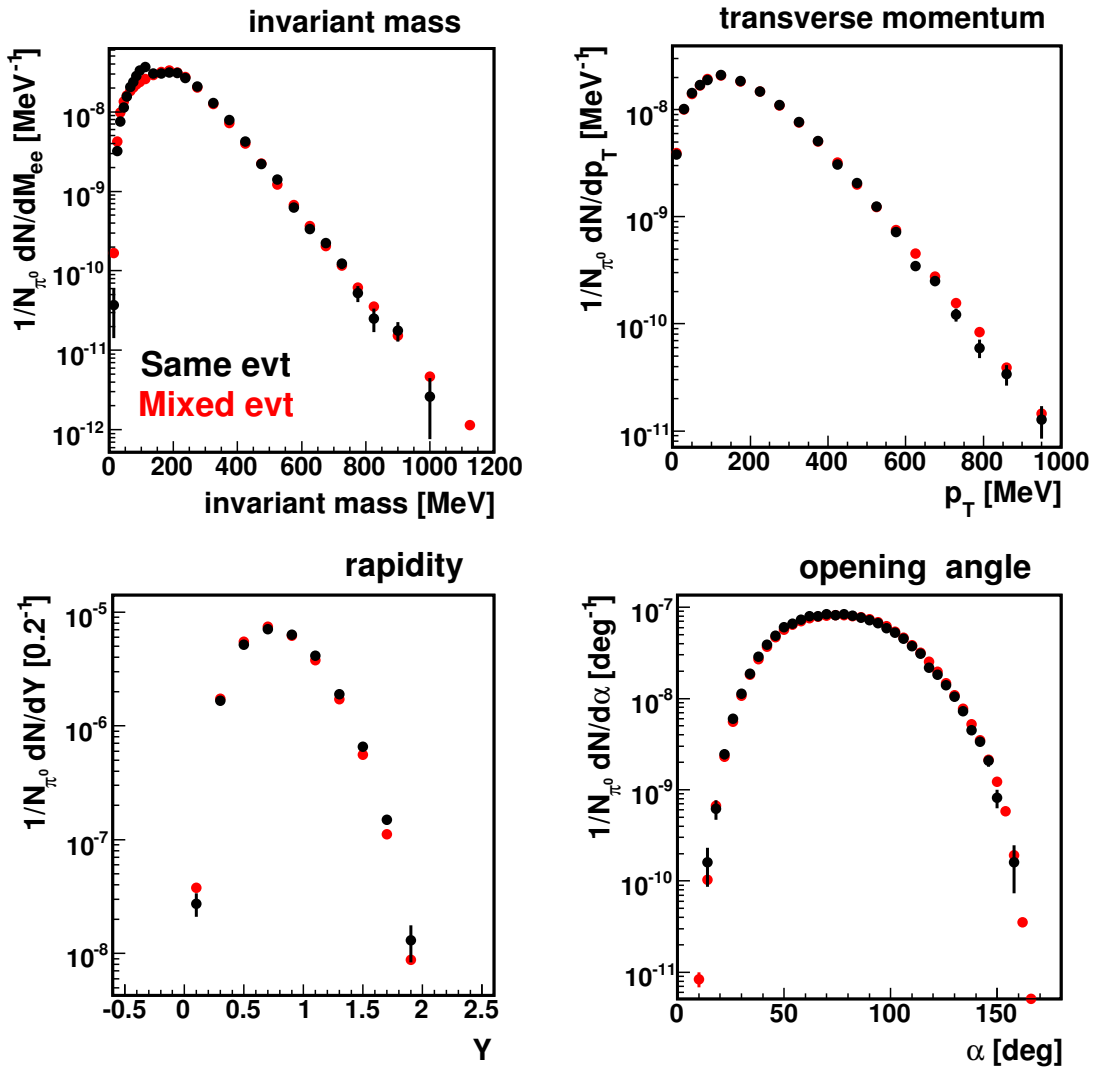


Figure 7.10.: Invariant mass, transverse momentum, rapidity, and opening angle combinatorial background distributions. Comparison between the same-event like-sign background (black points) and the mixed-event  $e^-e^+$  background (red points). All distributions are normalized per one neutral pion.

## 7. Pair analysis

From now on, all mixed-event spectra will be presented only summed up over all reaction classes after they were scaled to the corresponding same-event like-sign pair distributions in each of the reaction classes first. In Figures 7.8, 7.9, and 7.10, we show how the utilized mixed-event technique reproduces invariant mass, rapidity, transverse momentum, and opening angle spectra of the same-event  $e^+e^+$  and  $e^-e^-$  pairs and the same-event like-sign background. The rapidity, transverse momentum, and opening angle distributions were constructed only for the pairs having invariant masses greater than 150 MeV.

The same-event like-sign and the mixed-event background were combined together as follows. Below the invariant mass 450 MeV, I used the same-event like-sign background. Above this invariant mass, it is employed properly scaled mixed-event background. Uncertainty in determining the scaling constant was quadratically added to the statistical error of the mixed-event background points. This combined background was finally used to obtain the raw, i.e., reconstruction efficiency uncorrected, signal, see Figure 7.11.

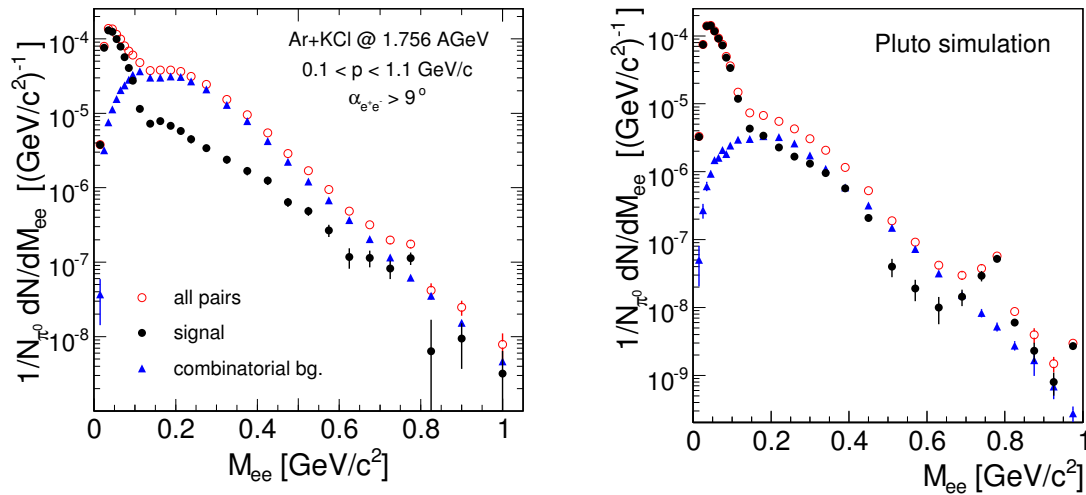


Figure 7.11.: Invariant mass spectrum of the raw signal (black points), the combinatorial background (blue triangles), and all electron-positron pairs (red circles). **Left:** Experiment. **Right:** Pluto simulation. In both cases, combinatorial background is composed from same-event like-sign pairs (below pair mass 450 MeV) and properly scaled mixed event background (above pair mass 450 MeV). All distributions are normalized per one neutral pion. In addition, spectra from Pluto were scaled down by a factor  $1.69 \times 1.69$ , which takes into account the difference between simulations and experiment, see Section 6.5 and Appendix A.

Now, let us deal with the question to what extent our analysis is able to reconstruct the true shape of the combinatorial background and the signal. To study this issue, I employed the Pluto simulation. Pluto events were processed with the HGeant code, digitizers, and further I analyzed them as the usual experimental data. According to information provided by the Pluto, it can be judged which lepton pairs originate from the same primary vertex and which of them are just accidental combinations. The reconstructed and the true signal and combinatorial background are

contrasted in Figure 7.12. The simulation suggests that we can expect a fairly good agreement between the true and the reconstructed shapes over the whole invariant mass range. The largest discrepancies between them can be seen only in the region 150–300 MeV, where the combinatorial background reaches its maximum. Nevertheless, these discrepancies do not exceed 20 %.

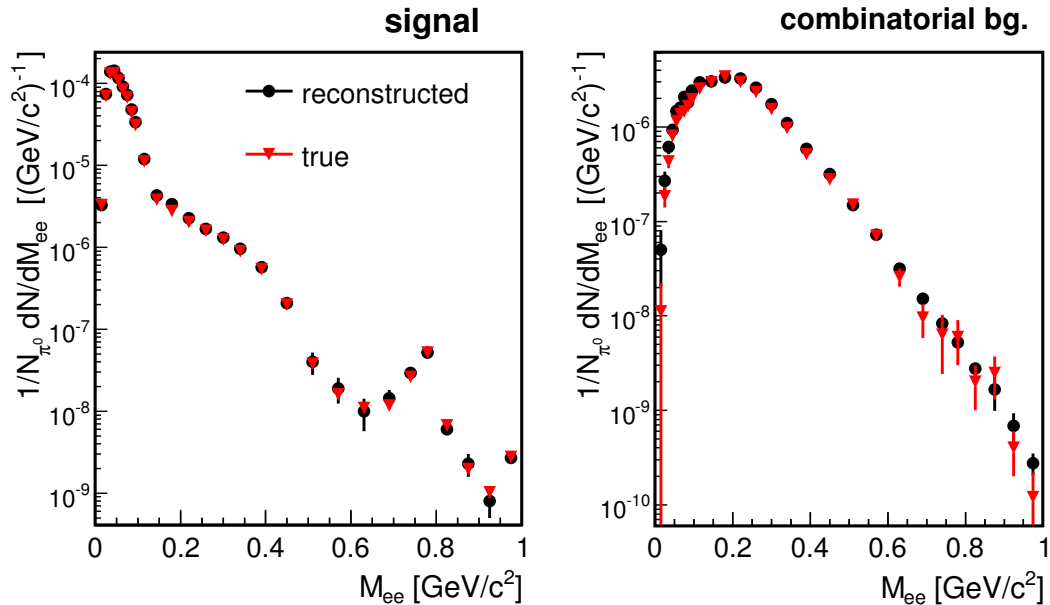


Figure 7.12.: True (red triangles) and reconstructed (black circles) raw signal and combinatorial background. The reconstructed combinatorial background is composed from same-event like-sign pairs (below pair mass 450 MeV) and properly scaled mixed event background (above mass 450 MeV). Data are based on the Pluto simulation. The distributions are normalized per one neutral pion.

## 7.5. Efficiency correction

The final goal of the whole di-lepton analysis is to provide pair spectra for testing predictions of proposed theoretical models. Usually, the HADES collaboration publishes the pair yield which was corrected on the reconstruction efficiency in the geometrical acceptance of the spectrometer. Experimental distributions are then contrasted to a theoretical di-lepton cocktail processed with the HADES acceptance filter and smeared with a realistic momentum and angular detector resolution.

The efficiency correction should take into account tracking and lepton identification inefficiencies, i.e., inefficiencies of the used hard-cut method, as well as losses caused by some of the pair cuts. As the correction can change significantly the shape of a pair spectrum, correct handling of this procedure represents a quite delicate operation. In my analysis, I assumed that the pair reconstruction efficiency can be factorized as a product of a single electron and a single positron reconstruction

efficiencies. This presumption can be justified by the large 9 deg pair opening angle cut which was employed.

A single lepton efficiency matrix is represented by a three-dimensional table of probabilities. The probabilities tell us how likely it is that a lepton emitted within certain momentum times polar angle times azimuthal angle range is going to be properly reconstructed and that it survives all successive hard-cuts. The determination of our single electron/positron efficiency matrix proceeded in the following steps. Simulated “white” electrons/positrons were embedded into real events. The adjective white means that electrons/positrons were generated randomly with a uniform distribution in momentum ( $p \in (0, 1500)$  MeV), polar angle ( $\theta \in (0, 90)$  deg), and azimuthal angle ( $\Phi \in (0, 360)$  deg). Nevertheless, it was ensured that the pairs created out of the white leptons have always an opening angle larger than 9 deg and that they do not share a common hit in any sub-detector. Embedding to real events should properly take into account an influence of the surrounding hadronic environment.

All events with embedded white leptons were processed through our usual single lepton and pair analysis. The efficiency  $\epsilon = \epsilon(p, \theta, \Phi)$  was then estimated as the ratio

$$\epsilon(p, \theta, \Phi) = \frac{\sum_{i=1}^{N_{rec}} w(p_i)}{\sum_{j=1}^{N_{init}} w(p_j)}. \quad (7.1)$$

The upper sum runs over the embedded electrons/positrons, which survived all cuts applied on the single lepton and the pair level of the analysis, inside the interval  $(p, p + \Delta p) \times (\theta, \theta + \Delta\theta) \times (\Phi, \Phi + \Delta\Phi)$ . Here  $\Delta p$ ,  $\Delta\theta$ , and  $\Delta\Phi$  denote discretization parameters in momentum, polar angle, and azimuthal angle coordinates, respectively. Each electron/positron is weighted with a, generally momentum dependent, weight  $w = w(p_i)$ . This weighting takes into account the fact that in real experiment, the momentum spectrum of leptons steeply drops. The sum in the denominator runs over all initial white tracks that were in geometrical acceptance of the spectrometer in the interval  $(p, p + \Delta p) \times (\theta, \theta + \Delta\theta) \times (\Phi, \Phi + \Delta\Phi)$ . The weighting of leptons in the denominator was done in the same way as in the numerator.

Concerning the choice of the weighting, I used two sets of efficiency matrices. For pairs with the invariant mass below 0.09 GeV, I used efficiency matrices which assumed weighting according to the formula

$$w(p_i) = C_1 \exp(-\zeta_1 p_i) + C_2 \exp(-\zeta_2 p_i).$$

Here  $C_1$  and  $C_2$  are constants,  $p_i$  denotes a particle momentum, and  $\zeta_1$  and  $\zeta_2$  stand for slope factors of the momentum distribution deduced from the experiment. This dependence should parametrize the measured momentum distribution of single leptons, originating mainly from the  $\pi^0$  source. For pairs having masses above 0.09 GeV, I used efficiency matrices which were weighted with a uniform distribution. Sources, contributing to this invariant mass region, have less steep momentum distribution than the  $\pi^0$  Dalitz decay.

This combination of efficiency matrices turned out to provide the best result in the self-consistency check (to be explained later). Just for illustration, in Figure 7.13,

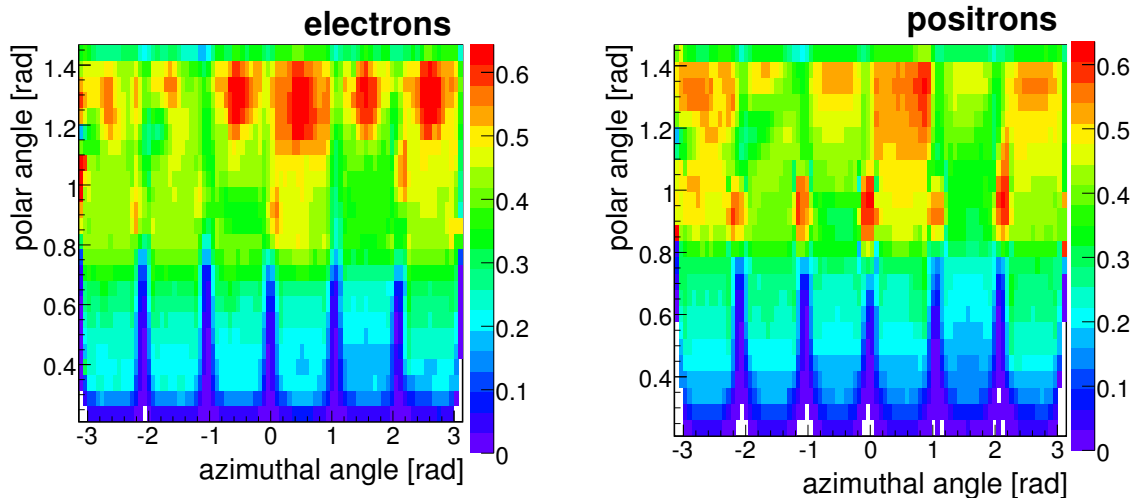


Figure 7.13.: Momentum averaged efficiency matrix for electrons (**Left**) and positrons (**Right**).

we show the exponentially weighted momentum averaged efficiency matrices for electrons and positrons. Each matrix cell had a size of  $\Delta p \times \Delta\theta \times \Delta\Phi = 15 \text{ MeV} \times 3 \text{ deg} \times 4 \text{ deg}$ .

Weight of a pair, resulting from the efficiency correction, equals  $1/(\epsilon_1\epsilon_2)$ . The pairs which have too low efficiency, and consequently large efficiency correction, can easily spoil the shape of the final spectrum. Hence, the signal was reconstructed only from those pairs, where each leg had efficiency above 0.05. In Section 6.5, we pointed out that shape of simulated and experimental distributions of single leptons is the same. However, after normalization per one neutral pion, simulated data are above experiment. Our efficiency matrices, which were obtained from simulation, do not take this fact into account. Therefore, whenever I corrected experimental pair spectra on the efficiency of reconstruction and identification, it was necessary also to scale the spectra up with a factor  $1.69 \times 1.69$ . A comparison of the experimental efficiency uncorrected and the corrected invariant mass spectrum can be seen in Figure 7.14.

In order to estimate to what extent are the results of the efficiency correction under control, I made the so-called “self-consistency check”. The check has the undermentioned steps. First of all, di-lepton cocktail was produced using the Pluto event generator. On top of this cocktail I made two independent analyses:

1. In the first branch, the Pluto cocktail was processed with our standard analysis chain, i.e., simulation of particle interactions and energy losses in the spectrometer with the HGeant code and modelling detector responds with the digitizers. Then the leptons, which were identified using the hard-cut method, were used to build pairs. The proper pairs were selected using our pair cuts. Finally, raw spectra of pairs were corrected on reconstruction efficiency.
2. In the second branch, the same Pluto cocktail was filtered through the geo-

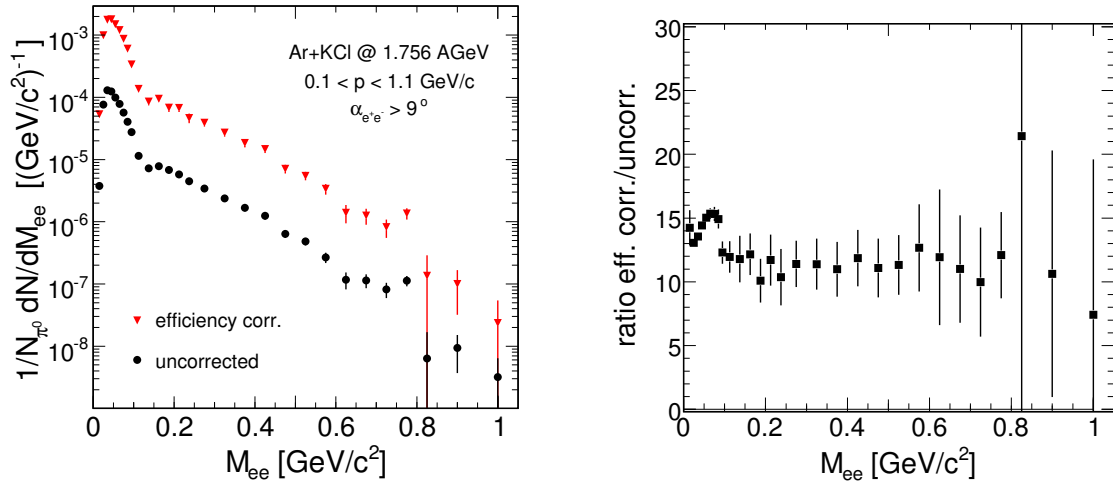


Figure 7.14.: **Left:** Efficiency uncorrected (black circles) and efficiency corrected (red triangles) pair invariant mass spectrum. Both distributions were normalized per one neutral pion. **Right:** Ratio of the efficiency corrected to the efficiency uncorrected spectrum.

metrical acceptance of the spectrometer<sup>3</sup>. A direction and a size of each lepton momentum was realistically smeared. Leptons had to pass our cut on momentum size  $100 < p < 1100$  MeV. Then I selected pairs originating from the decay of the same mother particle having an opening angle larger than 9 deg. These pairs were used to reconstruct the signal.

After the normalization on LVL1 event, results of 1. and 2. should overly, for illustration see Figure 7.15. The self-consistency check suggests that the systematic error of the efficiency correction should be below 25 %. The results of the self-consistency check are discussed in more detail in Appendix A.

## 7.6. Normalization

The HADES collaboration presents their pair spectra normalized to  $N_{\pi^0}$ , the total number of neutral pions, which were produced to the full solid angle in the amount of LVL1 events corresponding to the obtained pair statistics. Like this we compensate to first order the bias caused by the implicit centrality selection of our trigger. Signal distributions are then normalized according to the pattern:

$$\frac{1}{N_{\pi^0}} \frac{dN}{dX_{ee}} = \frac{1}{\varepsilon_{LVL2}^{ee} N_{LVL1} k_{LVL1}^{\pi^0}} \frac{dn}{dX_{ee}}. \quad (7.2)$$

Here  $X_{ee}$  denotes a pair observable (invariant mass, transverse momentum, rapidity, or opening angle),  $dn/dX_{ee}$  stays for a distribution of the measured pair yield with respect to the quantity  $X_{ee}$  normalized per one unit of  $X_{ee}$ . The factors, which

<sup>3</sup>In addition, I have also required that each lepton has to have efficiency  $\epsilon > 0.05$ .

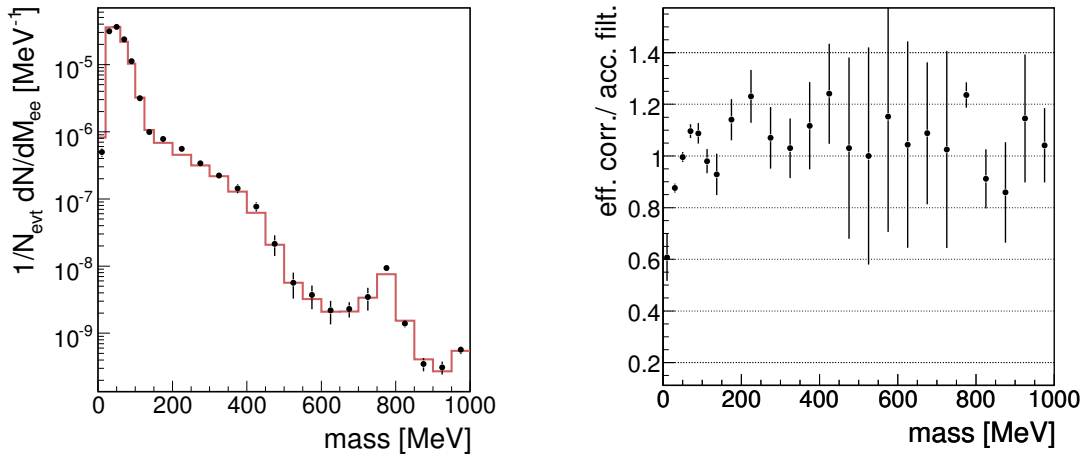


Figure 7.15.: Results of the self-consistency check. **Left:** Invariant mass spectrum of signal pairs from the full Pluto cocktail. The “reconstructed+efficiency corrected data” are marked with the black points. The brown histograms show the “acceptance filtered+momentum smeared cocktail”. Spectra are normalized per one event. **Right:** Ratio of the reconstructed+efficiency corrected data and the corresponding acceptance filtered+momentum smeared cocktail.

are placed in front of  $dn/dX_{ee}$ , take into account the LVL2 trigger pair efficiency ( $\varepsilon_{LVL2}^{ee}$ ), the total number of LVL1 pure target events ( $N_{LVL1}$ ), and the number of neutral pions in the full solid angle per one LVL1 event ( $k_{LVL1}^{\pi^0}$ ).

Some numbers concerning the pion production in the Ar+KCl run are shown in Table 7.4. The HADES spectrometer is able to measure only charged pion production, hence the value of  $k_{LVL1}^{\pi^0}$  has to be estimated. Table 7.4 suggests that the UrQMD simulation reproduces well the value of the ratio of charged pion multiplicities from the experiment. So, if we believe that the simulation reproduces correctly also the ratio between charged and neutral pion multiplicities then the experimental value of  $k_{LVL1}^{\pi^0}$  should be  $k_{LVL1}^{\pi^0} = (3.6 \pm 0.4)$ . The errors quoted in Table 7.4 are systematic. They result from an extrapolation of the pion yield to the full solid angle and an efficiency correction. The statistical errors are negligible.

	Exp		UrQMD		
	LVL1 HADES	LVL1 $4\pi$	LVL1 HADES	LVL1 $4\pi$	MB $4\pi$
$\pi^+$	1.9	$3.2 \pm 0.3$	2.12	3.51	1.74
$\pi^-$	2.3	$3.7 \pm 0.4$	2.57	4.16	2.05
$\pi^0$	-	-	-	4.07	2.07

Table 7.4.: Pion production in the Ar+KCl run. The column “LVL1 HADES” quotes pion multiplicities measured in LVL1 events in the geometrical acceptance of the HADES spectrometer. The column “LVL1  $4\pi$ ” contains pion multiplicities extrapolated to the full solid angle. In case of the UrQMD simulation, we show also pion multiplicities in minimum bias events in the full solid angle. Numbers stated in this table were provided by HADES pion experts.

## 7. Pair analysis

The total number of the LVL1 pure target events  $N_{LVL1}$  was deduced from the total number of LVL1 events  $n_{LVL1} = 2.25 \times 10^9$  and the portion of empty target LVL1 events  $f_{ET} = (0.05 \pm 0.01)$ , see Section 5.1. For  $N_{LVL1}$ , it follows

$$N_{LVL1} = (1 - f_{ET})n_{LVL1}.$$

The second level trigger efficiency  $\varepsilon_{LVL2}^{ee}$  for positive marking events, where an identified lepton pair emerges, is estimated similarly to what was already discussed in Section 6.7,

$$\varepsilon_{LVL2}^{ee} = \frac{n_{LVL2}^{ee}}{n_{LVL1}^{ee}(f_{DS} - 1)}.$$

Here  $n_{LVL2}^{ee}$  stands for the number of pairs identified in the positively triggered LVL2 events which were not downscaled. The symbol  $n_{LVL1}^{ee}$  denotes the number of pairs identified in the LVL1 events which were stored without the second level trigger decision being regarded. The meaning of the factor  $f_{DS} - 1$  was explained in Section 6.7. The efficiency  $\varepsilon_{LVL2}^{ee}$  should not depend on pair observables like the total charge, invariant mass, or rapidity. We illustrate this in Figure 7.16.

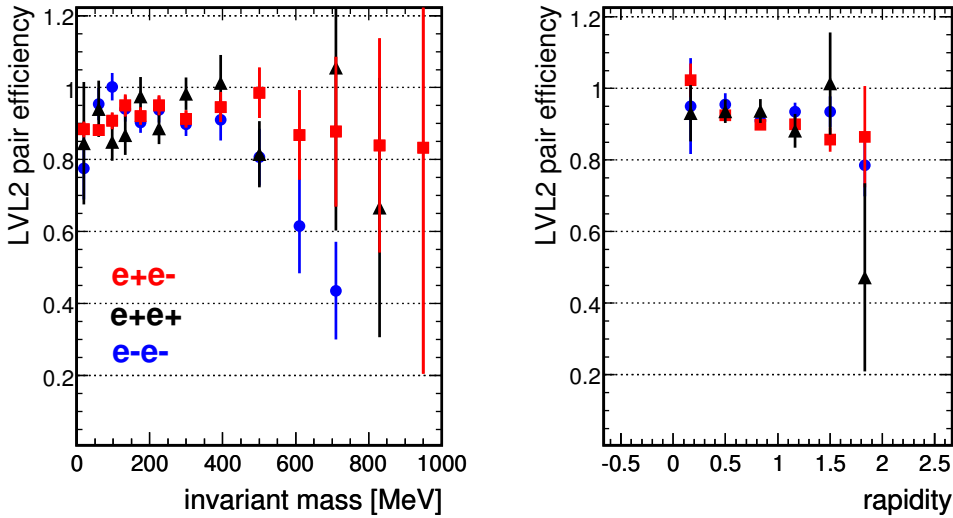


Figure 7.16.: The LVL2 trigger efficiency for recognizing an event containing a pair as a function of pair invariant mass (**Left**) and pair rapidity (**Right**).

Unfortunately, the sample of like-sign pairs suffers from lack of statistics in the regions of high invariant mass and rapidity. The average value of the second level trigger efficiency was for unlike-sign pairs estimated to be  $\approx 0.90$ , for like-sign pairs  $\approx 0.92$ , and for signal pairs  $\approx 0.89$ . Thus, the true value of the second level trigger efficiency is most probably located in the range  $\varepsilon_{LVL2}^{ee} = (0.90 \pm 0.02)$ .

## 7.7. Estimation of systematic error

The total systematic error of our efficiency corrected spectra originates mainly from the three sources:

1. The systematic error of the overall normalization factor  $N_{\pi^0}$  in Equation (7.2). This error consists of systematic uncertainties of the mean  $\pi^0$  multiplicity extrapolated to the full solid angle  $k_{LVL1}^{\pi^0}$ , the empty target fraction  $f_{ET}$ , and the LVL2 trigger efficiency  $\varepsilon_{LVL2}^{ee}$ . Assuming that these quantities behave independently we may conclude that the systematic error of the  $N_{\pi^0}$  is about 11 %.
2. The systematic error resulting from the method used to determine the combinatorial background. When we compared the reconstructed and the true shape of our signal in our Pluto+Geant simulations, see Figure 7.12, the maximal differences reached about 20 %.
3. The 25% uncertainty following from the correction on the reconstruction and identification efficiency.

Supposing that these three contributions are independent, squares of errors are summed up under a square root. The total systematic error of the normalized efficiency corrected spectra is then about 35 %.



## 8 Discussion of results

In this chapter, I will compare the efficiency corrected pair spectra with predictions of the Pluto generator and the much more sophisticated HSD transport code. Possible signals of “in-medium” modification of the  $\rho^0$  meson will be discussed. Finally, I will contrast the invariant mass distribution of pairs from the Ar+KCl run with results of the predecessor C+C at 1 and 2 A GeV HADES measurements.

### 8.1. Comparison with Pluto

Pluto [66, 67] is a thermal model based Monte Carlo event generator. It populates phase space with hadrons ( $\pi^0$ ,  $\eta$ , etc.) like if they would be emitted from a thermalized source. Parameters of the fireball after the freeze-out point (e.g., mean meson multiplicities, angular anisotropy, or temperature slopes) are taken or estimated from the known experimental data. Di-leptons are produced from decays of hadrons regarding the corresponding branching ratio and angular particle distribution. The free partial decay widths are assumed. Finally, the Pluto event generator provides a pair cocktail which is an incoherent sum of di-lepton yields coming from different sources.

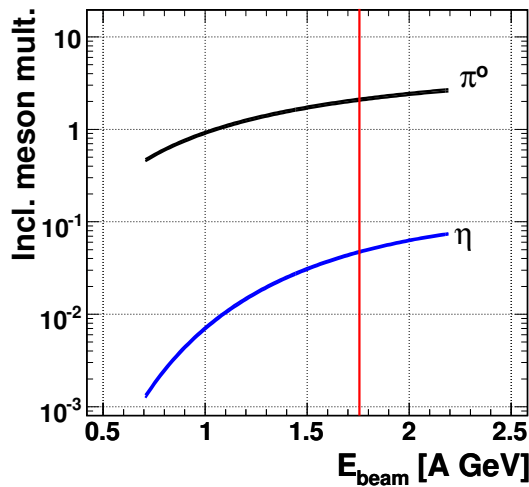


Figure 8.1.: Inclusive meson multiplicities in minimum bias Ar+KCl collisions as a function of the beam energy. The solid red line indicates the energy 1.756 A GeV. The lines corresponding to  $\pi^0$  and  $\eta$  production represent a fit to measurements by TAPS [78, 79].

In case of Ar+KCl collisions, the mean minimum bias multiplicities of  $\pi^0$  and  $\eta$  mesons were guessed from a fit to the TAPS data systematics [78, 79], see Figure 8.1. Since the minimum bias multiplicities of heavier mesons ( $\omega$ ,  $\rho$ ,  $\phi$ ) are experimentally not known, they were estimated by means of the  $m_{\perp}$ -scaling ansatz [81], see Table 8.1. Moreover, we took into account the bias caused by our LVL1 trigger which preferentially selected more central events, see Section 5.5. Therefore, the

## 8. Discussion of results

minimum bias multiplicities were scaled up two times. The factor 2.0 was deduced from our UrQMD simulation and it reflects the enhancement of the mean pion multiplicity in LVL1 events with respect to the minimum bias reactions, see Table 5.1. Temperature slopes and parameters describing angular anisotropies of the flow were estimated from transport code calculations (HSD). Branching ratios to the channels producing di-leptons were taken from the Particle Data Group [2].

Meson	$\pi^0$	$\eta$	$\omega$	$\rho$	$\phi$
Multiplicity	2.04	$4.6 \times 10^{-2}$	$2.3 \times 10^{-3}$	$2.5 \times 10^{-2}$	$1.0 \times 10^{-4}$

Table 8.1.: Inclusive mean meson multiplicities in a minimum bias Ar+KCl at 1.756 A GeV collision which were entered to the Pluto event generator. In Pluto, these multiplicities were multiplied by the factor 2.0 to take into account the LVL1 trigger bias.

Electrons and positrons created by the Pluto event generator have to be filtered through the geometrical acceptance of the HADES spectrometer. Afterwards, their momentum is smeared realistically following the procedure described in Appendix A. Finally, pairs have to undergo the physical cuts which cannot be reproduced by the efficiency correction, namely:

- opening angle of each pair  $> 9$  deg and
- size of momentum of each lepton is within the range  $100 < p < 1100$  MeV.

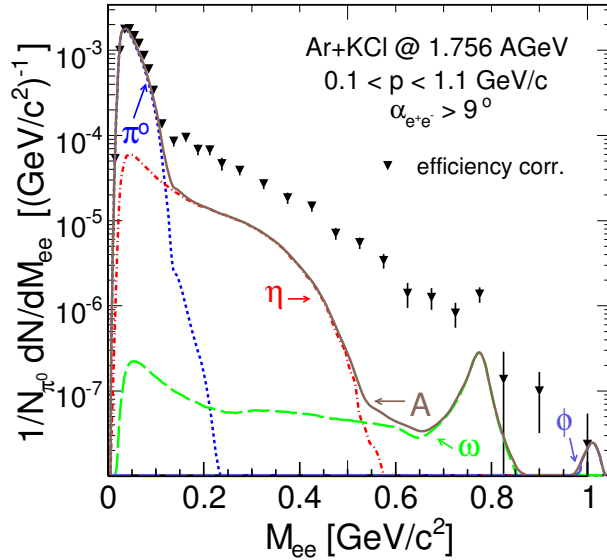


Figure 8.2.: Comparison of the experimental efficiency corrected invariant mass spectrum with the Pluto cocktail A. See the text for explanation.

First of all, I will contrast my experimental pair invariant mass spectrum with the so-called Pluto cocktail A, see Figure 8.2. This cocktail is made up from  $e^+e^-$  pairs

originating from the long-lived di-lepton sources:  $\pi^0$ ,  $\eta$ ,  $\omega$ , and  $\phi$ . We have considered the decays  $\pi^0 \rightarrow \gamma e^+e^-$ ,  $\eta \rightarrow \gamma e^+e^-$ ,  $\omega \rightarrow \pi^0 e^+e^-$ ,  $\omega \rightarrow e^+e^-$ ,  $\phi \rightarrow \eta e^+e^-$ , and  $\phi \rightarrow e^+e^-$ . Only the yields after the chemical and thermal freeze-out of the fireball are shown. The Pluto cocktail A reproduces the experimental distribution only in the region below the invariant mass 0.15 GeV, region dominated by the  $\pi^0$  Dalitz decay. The sources forming the cocktail A cannot explain substantial part of the pair yield above 0.15 GeV. In the mass range 0.15–0.40 GeV, the experimental yield is about 4–5 times larger than what we would expect from the  $\eta$  Dalitz decay alone. Yet, we can supplement the cocktail A with contributions of the short lived resonances  $\rho^0$  and  $\Delta^{0,+}(1232)$ . This gives us the Pluto cocktail B, see Figure 8.3. These resonances are mainly created in the early stages of a collision. The Pluto event generator estimates their share in pair production only at the freeze-out point. To include  $\Delta^{0,+} \rightarrow N e^+e^-$  source into the cocktail, it was assumed that within the energy regime 1–2 A GeV, the  $\Delta$  yield scales with the  $\pi^0$  yield measured at the freeze-out. The decay rate which was employed was calculated in [82]. The mass distribution of  $\rho^0$  was described with a Breit-Wigner shape having a width  $\Gamma = 150$  MeV. The mass of  $\rho^0$  was limited from below by the constraint  $M_{\rho^0} > 2M_\pi$ , where  $M_\pi$  stands for the pion mass. Further, it was taken into account that the partial decay width  $\Gamma(M_{\rho^0})_{\rho^0 \rightarrow e^+e^-}$  depends on the  $\rho^0$  mass proportionally to  $1/M_{\rho^0}^3$  as it is imposed by vector dominance [83]. Although, the Pluto cocktail B improved the agreement below the  $\omega$  peak, it does not explain the origin of the substantial part of the pair yield in the region above the invariant mass 0.15 GeV.

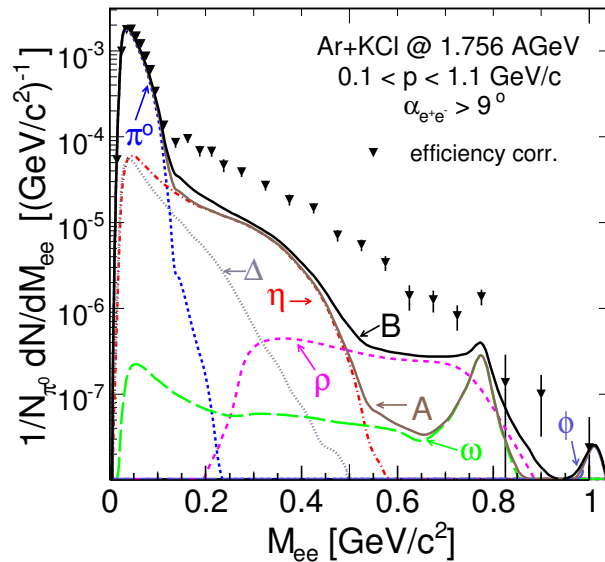


Figure 8.3.: Comparison of the experimental efficiency corrected invariant mass spectrum with the Pluto cocktail B. See the text for explanation.

Complementary information about the observed excess can be extracted from transverse momentum and rapidity distributions of signal pairs, see Figure 8.4. The significance of different di-electron sources changes according to selected invariant

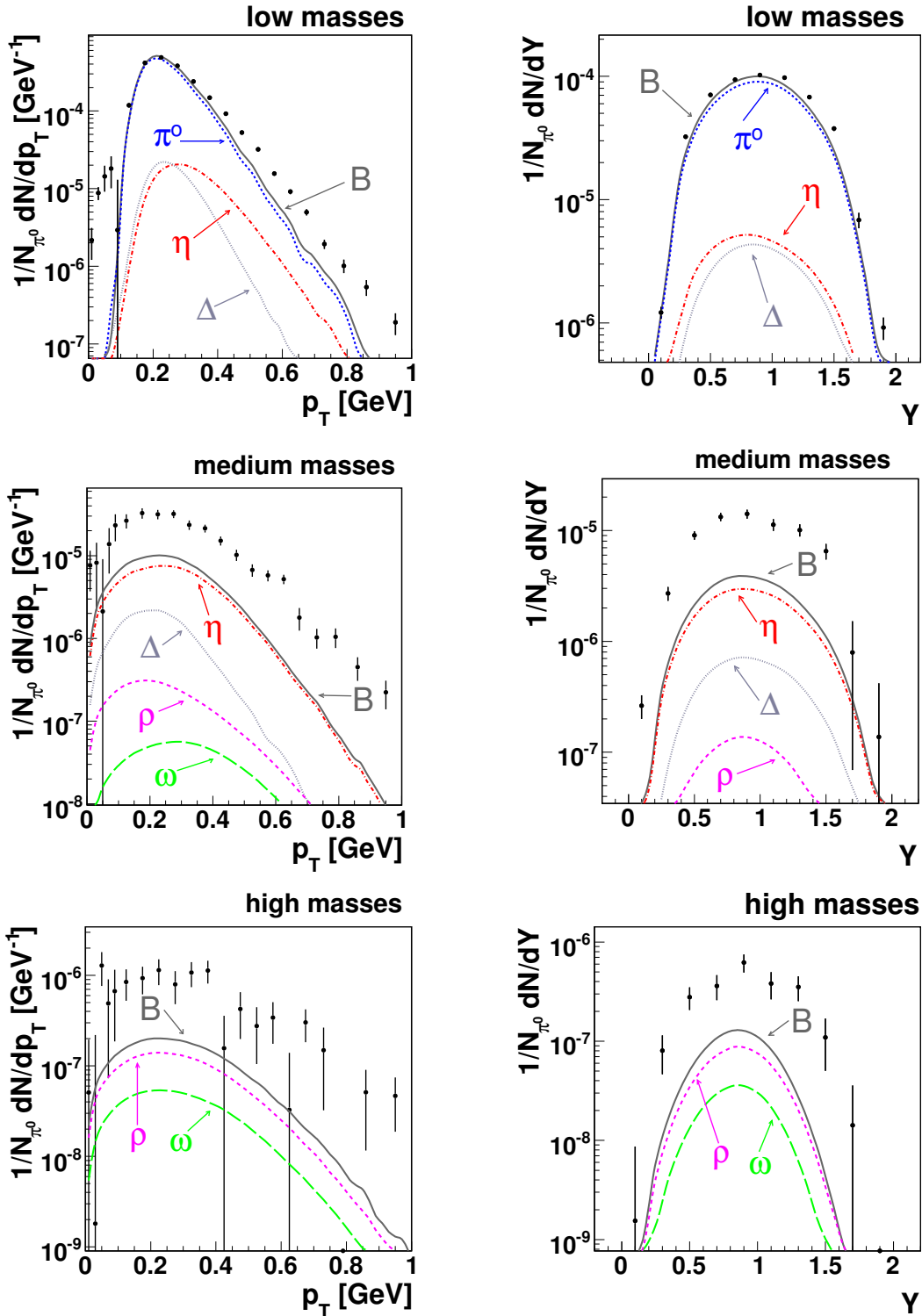


Figure 8.4.: Transverse momentum (**Left**) and rapidity (**Right**) distributions of signal pairs in experiment (black points) and in the Pluto cocktail B. Three invariant mass regions were considered: low pair masses  $M_{ee} < 150$  MeV, medium masses  $150 \leq M_{ee} < 550$  MeV, and high masses  $M_{ee} \geq 550$  MeV. The Pluto cocktail A is not shown explicitly, but in the sequence of the mass intervals, it would almost coincide with  $\pi^0$ ,  $\eta$ , and  $\omega$  source, respectively.

mass region. Therefore, I considered three invariant mass regions: low pair masses  $M_{ee} < 150$  MeV, medium masses  $150 \leq M_{ee} < 550$  MeV, and high masses  $M_{ee} \geq 550$  MeV. The  $\pi^0$  Dalitz decay is the dominant source of pairs in the low mass region. Indeed, the Pluto  $\pi^0 \rightarrow \gamma e^+ e^-$  source alone can explain a large part of the experimental yield. Nevertheless, the measured transverse momentum spectrum is somewhat harder with respect to what is predicted by the Pluto. Pairs with low invariant mass but high  $p_T$  probably origin from resonance decays. In the medium and in the high pair invariant masses regions, experimental data exceed the Pluto cocktail B roughly 3–4 times.

It is obvious that the Pluto event generator is not able to provide a satisfactory description of the measured pair yields. We have to keep in mind that predictions of the Pluto relate only to the period after the chemical and thermal freeze-out of the fireball. On the other hand, a nucleus-nucleus collision is a rather non-equilibrium system, especially in the early stages. At that time, various processes, which cannot be reproduced by a thermal model, take place, e.g., interactions of off-shell particles. On the microscopic level, the full collision dynamics is treated by the so-called *transport codes*. From the transport codes which are available on the market at present, let us mention HSD [37, 80], IQMD [40], UrQMD [69, 70, 71], or RQMD [84]. In the next Section, I will contrast the efficiency corrected pair spectra from the Ar+KCl run with a di-electron cocktail provided by the HSD group, published in [85] recently.

## 8.2. Comparison with HSD

I had two versions of the HSD cocktail at my disposal. The first one assumed that all particles have their vacuum spectral function. The latter one took into account that  $\rho^0$  and  $\omega$  follow one of the “in-medium” scenarios. According to this scenario, the vacuum spectral functions should simultaneously undergo collisional broadening and dropping mass in surrounding nuclear matter. The “in-medium” width  $\Gamma_V^*$ , increased by the collisional broadening, can be for a given vector meson  $V$  written as

$$\Gamma_V^*(M, |\vec{p}|, \rho_N) = \Gamma_V(M) + \Gamma_{\text{coll}}(M, |\vec{p}|, \rho_N).$$

Here  $\Gamma_V$  is the total width of the meson  $V$  in the vacuum and the last term can be approximately expressed as

$$\Gamma_{\text{coll}}(M, |\vec{p}|, \rho_N) \approx \alpha_{\text{coll}} \frac{\rho_N}{\rho_0}.$$

It accounts for the “in-medium” broadening of the width due to interactions with hadrons in the nuclear environment of a density  $\rho_N$ . The normal nuclear density is denoted  $\rho_0$ ,  $\rho_0 = 0.16$  nucleon/fm<sup>3</sup>. The coefficient  $\alpha_{\text{coll}}$  is responsible for the strength of this effect. For more details see [85].

The dropping mass scenario follows the idea of Hatsuda and Lee [20]. The “in-medium” shifted pole mass  $M_0^*$  is parametrized as

$$M_0^*(\rho_N) = \frac{M_0}{(1 + \alpha_{\text{drop}} \rho_N / \rho_0)},$$

where  $M_0$  denotes the vacuum pole mass of the given vector meson. The authors of the paper [85] assumed  $\alpha_{drop} \simeq 0.16$  for the  $\rho^0$  and  $\alpha_{drop} \simeq 0.12$  for the  $\omega$  meson.

In the HSD output file, the whole impact parameter range of a minimum bias Ar+KCl collision (up to  $b = 11$  fm) is divided into several consecutive subintervals, each having a width of  $\Delta b = 0.5$  fm, see the left-hand side plot in Figure 8.5. For a given impact parameter and a di-electron source, the file quotes values of pair multiplicity distribution  $dN_{ee}/(dM_{ee} dp_T dY)$ . In our case, it was requisite to take into consideration the centrality bias produced by the LVL1 trigger in the experiment. Therefore, in each impact parameter annulus, I weighted pair multiplicities from the file with the step-like function shown in the right-hand side plot in Figure 8.5. It was obtained as the ratio of the impact parameter distributions corresponding to LVL1 and minimum bias reactions, see the left-hand side plot in Figure 5.7. Using this weighting I estimated from the HSD output file that the mean inclusive  $\pi^0$  multiplicity in LVL1 trigger events was 4.4. This number was then used to normalize all HSD spectra.

The HSD output file did not involve pairs from  $\phi$  decay. On the other hand, it took into account contributions of the NN and the  $\pi$ N Bremsstrahlung.

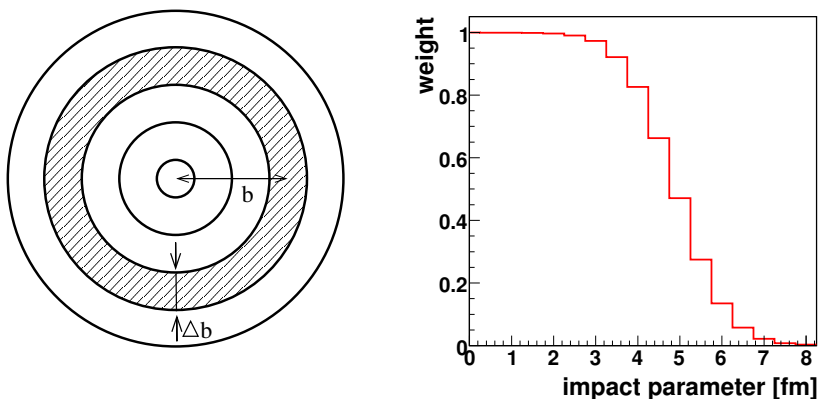


Figure 8.5.: **Left:** Impact parameter annuli. **Right:** Weights corresponding to a given impact parameter, when events are selected by the LVL1 trigger out of minimum bias Ar+KCl reactions. Data are based on our UrQMD simulation.

The experimental efficiency corrected invariant mass spectrum is contrasted to predictions of the HSD code in Figure 8.6. In the left-hand side plot, we show the cocktail which assumes that  $\rho^0$  and  $\omega$  mesons have their vacuum spectral functions. The “vacuum” HSD cocktail describes very well the experimental pair yield above the mass 0.15 GeV. Some minor discrepancies are visible only in the range 0.4–0.6 GeV, where the experimental yield is about factor 1.3–1.8 larger than the HSD cocktail. Indeed, this is the region where “in-medium” effects are expected to appear. With respect to the Pluto cocktail B, the  $\Delta$  Dalitz source is largely enhanced and declines less steeply.

The right hand-side plot in Figure 8.6 shows the situation when the spectral functions of  $\rho^0$  and  $\omega$  undergo collisional broadening and mass shift in medium.

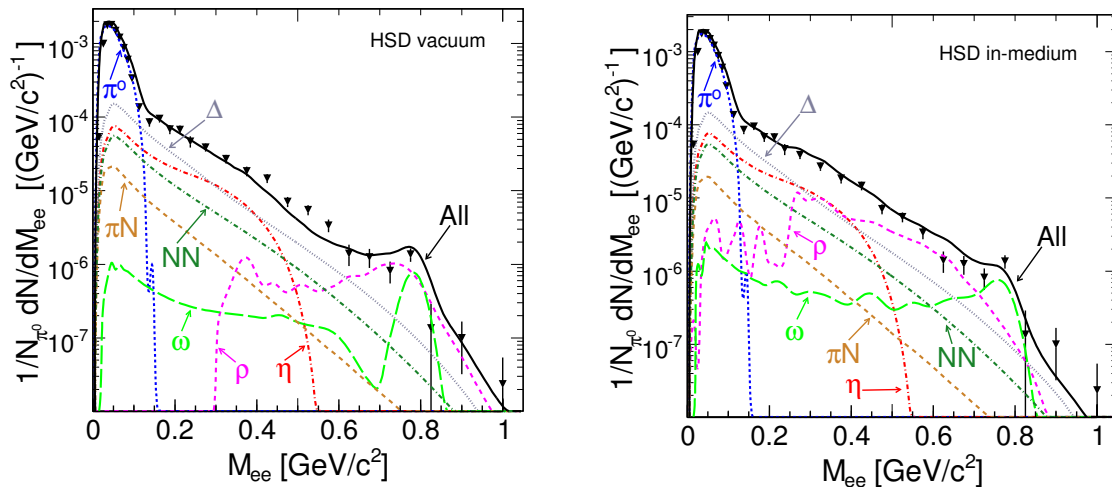


Figure 8.6.: The efficiency corrected pair invariant mass spectrum from the Ar+KCl run is compared with two versions of the HSD cocktail which assumed vacuum (**Left**) and in-medium (**Right**) behaviour of spectral functions for  $\rho^0$  and  $\omega$  mesons. With respect to the Pluto cocktail B, there are two new sources of pairs. The NN Bremsstrahlung is indicated by the dark green line and the  $\pi N$  Bremsstrahlung line has khaki colour.

The  $\rho^0 \rightarrow e^+e^-$  decay now creates preferentially pairs with lower invariant masses and the overall amplitude of this process has increased substantially. Though the “in-medium”  $\omega$  contribution exhibits also significant changes with respect to its vacuum shape, it stays far below the  $\rho^0$  in the region  $M_{ee} < 0.6$  GeV. Notice that the pair yield from the “in-medium”  $\rho^0$  filled the small gap 0.4–0.6 GeV.

In addition, we may compare the experimental efficiency corrected transverse momentum and rapidity spectra of pairs with the HSD “vacuum” and “in-medium” cocktail, see Figures 8.7 and 8.8, respectively. The pairs were divided into three groups according to their invariant masses. Both versions of the HSD cocktail describe the measured data equally well in the high mass and in the low mass region. Let us only note that in the low mass region, the HSD slightly overshoots the experimental data. Nevertheless, the discrepancies stay within the quoted systematic error. Slight differences between the “in-medium” and the “vacuum” cocktail can be seen only in the medium mass region, where the “in-medium”  $\rho^0$  improves agreement with the experimental data at low  $p_T$  and in the mid-rapidity.

So we may pose the question: Do we observe “in-medium” modification of the  $\rho^0$  in Ar+KCl reactions? It is not easy to find the true answer to this question. Unambiguous interpretation of “in-medium” signals from heavy ion experiments is always difficult. A nucleus-nucleus collision has, at least in the early stages, non-equilibrium nature. Di-electrons are typically produced from many different sources and it is nowhere written that the given transport code takes properly into account all relevant components of the cocktail. Another problem is that we do not know exactly cross-sections for many processes, which are included in the transport calculation. It seems that the Ar+KCl data are better described by the “in-medium”

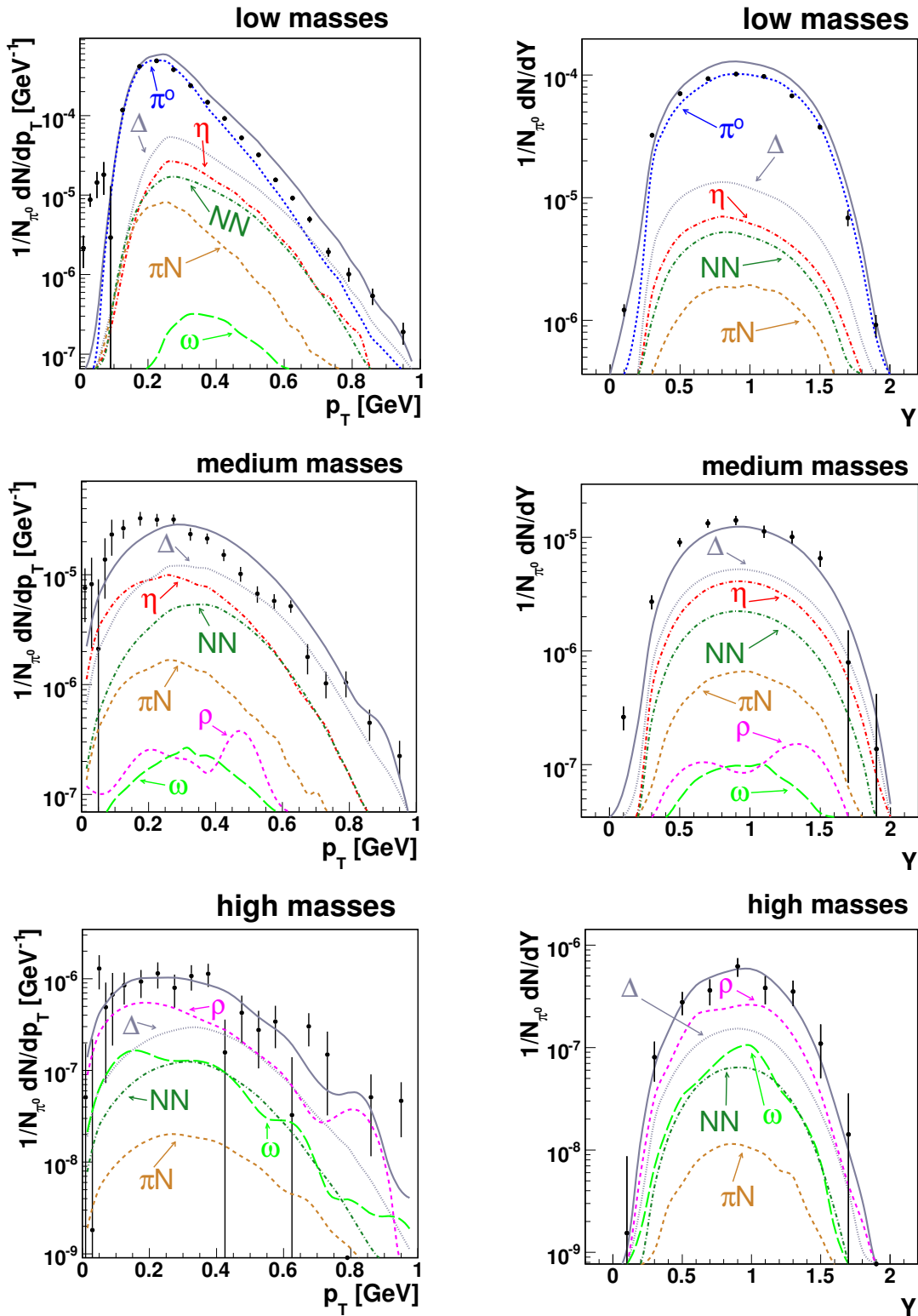


Figure 8.7.: Transverse momentum and rapidity distributions of signal pairs in experiment (black points) and in the “vacuum” HSD cocktail (grey line). Three regions of pair invariant masses were considered: low masses  $M_{ee} < 150$  MeV, medium masses  $150 \leq M_{ee} < 550$  MeV, and high masses  $M_{ee} \geq 550$  MeV.

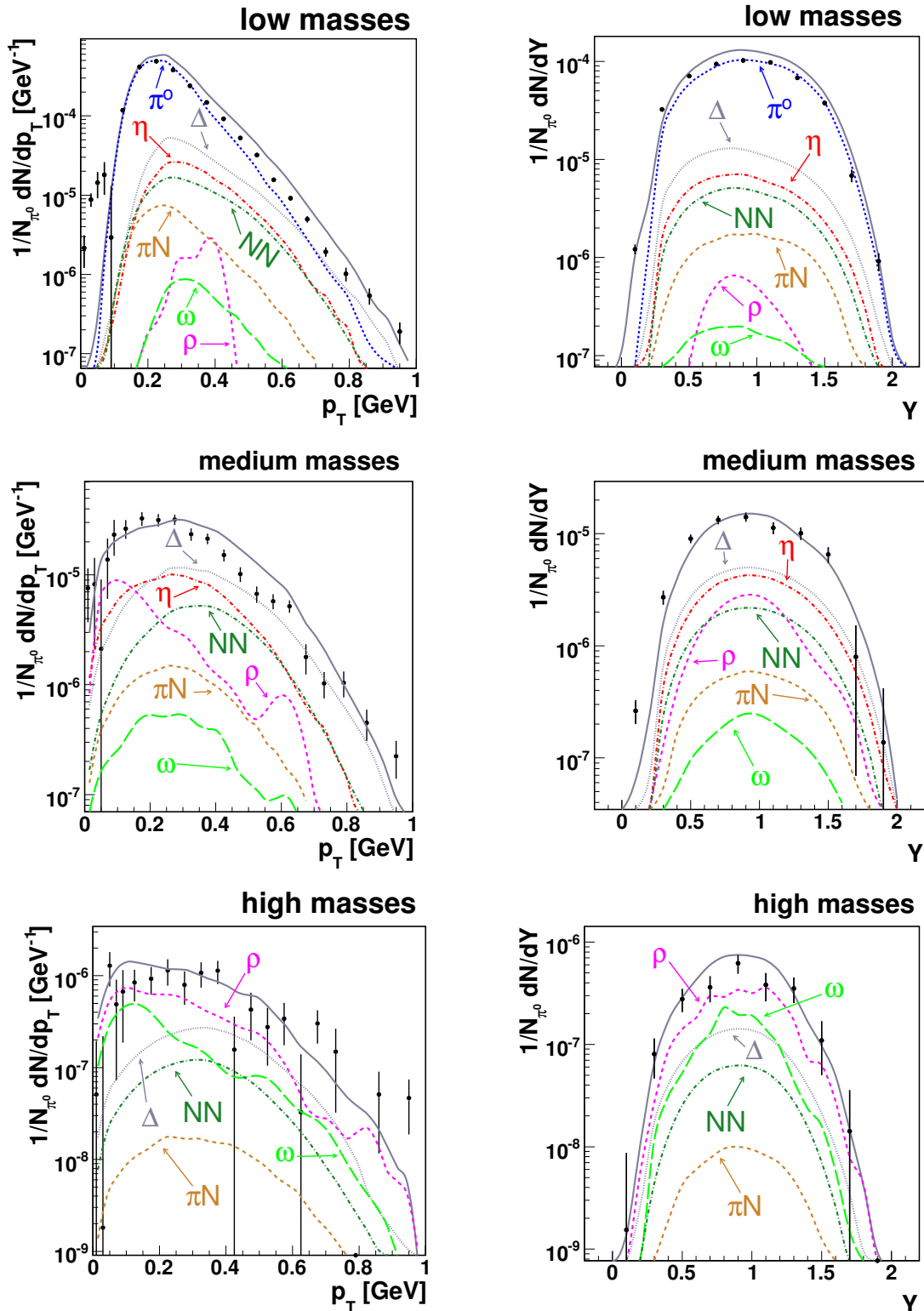


Figure 8.8.: Transverse momentum and rapidity distributions of signal pairs in experiment (black points) and in the “in-medium” HSD cocktail (grey line). Three regions of pair invariant masses were considered: low masses  $M_{ee} < 150$  MeV, medium masses  $150 \leq M_{ee} < 550$  MeV, and high masses  $M_{ee} \geq 550$  MeV.

cocktail. However, all discrepancies between the HSD “vacuum” cocktail and the measured spectra stay within the quoted systematic and statistical errors. Therefore, it is questionable to what extent the observed excess between 0.4–0.6 GeV is really produced by the “in-medium”  $\rho^0$ .

### 8.3. Comparison to lighter systems

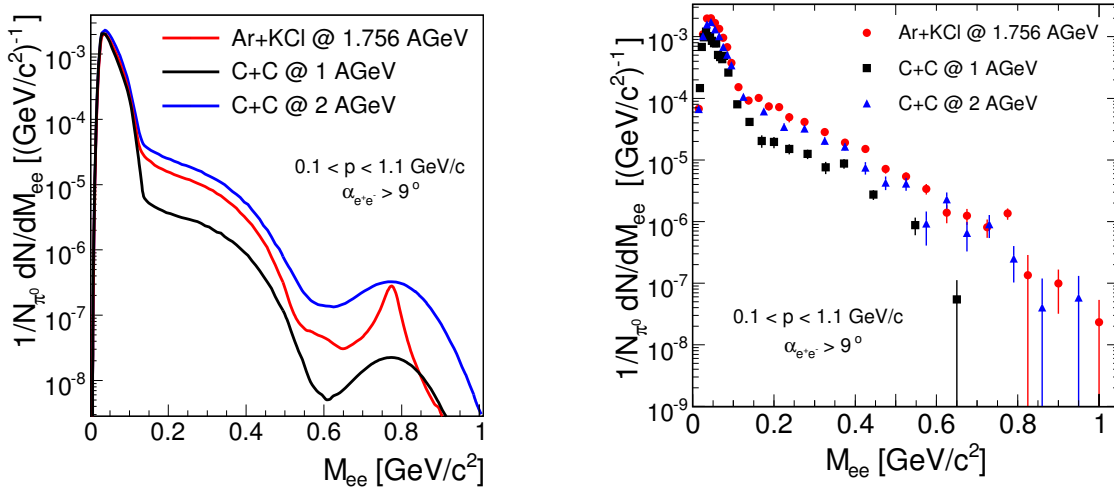


Figure 8.9.: Comparison between the Ar+KCl at 1.756 A GeV and the C+C at 1 and 2 A GeV invariant mass spectra of  $e^+e^-$  pairs. The distributions are shown in the geometrical acceptance of the C+C 1 A GeV run. For each run, I required that the cuts on momentum size  $100 < p < 1100$  MeV and opening angle  $> 9$  deg are fulfilled. All spectra are normalized per one neutral pion. **Left:** Pluto cocktail A shows expected contributions coming from  $\pi^0$ ,  $\eta$ , and  $\omega$  decays. **Right:** Experiment.

HADES started to investigate di-electron production in nucleus-nucleus collisions with the C+C at 2 A GeV [39] and the C+C at 1 A GeV [38] measurements. In this section, I will compare the results of these two predecessor experiments with the data from the Ar+KCl run. We would like to learn how different collision energy, eventually different system size, influences distribution of pair invariant masses. The analysis of the carbon data used similar pair cuts to what I employed for the Ar+KCl run, e.g., cut on 9 deg opening angle, cut on no double hit, etc. However, both C+C runs were carried out in low momentum resolution regime (kick plane method).

The left-hand side plot in Figure 8.9 shows for each HADES nucleus-nucleus run the corresponding Pluto cocktail A. Each cocktail was

- calculated from free  $\pi^0 \rightarrow \gamma e^+e^-$ ,  $\eta \rightarrow \gamma e^+e^-$ ,  $\omega \rightarrow \pi^0 e^+e^-$ , and  $\omega \rightarrow e^+e^-$  meson decays only,
- filtered with the geometrical acceptance of the C+C 1 A GeV run,
- smeared according to momentum resolution of the given run.

Further, the signal pairs were selected and I applied the 9 deg opening angle cut and the cut on size of momentum of each pair leg,  $100 < p < 1100$  MeV. After normalizing per one neutral pion, all three cocktails overlap in the region below the mass 0.1 GeV. Above this mass, individual distributions start to differ. In the  $\eta \rightarrow \gamma e^+e^-$  dominated region, the C+C at 2 A GeV cocktail exceeds the Ar+KCl cocktail. In both cases, colliding nucleons have enough energy to produce  $\eta$  in initial reactions via the process  $N + N \rightarrow N + N + \eta$ . On the other hand, we may see a strong suppression of  $\eta$  production in the C+C at 1 A GeV cocktail. Here, the energy of the primary nucleon-nucleon interactions is not sufficient to create  $\eta$  meson on-shell in one collision. The meson can emerge only after a series of intermediate-step interactions. In the  $\omega \rightarrow e^+e^-$  dominated region, differences between the individual Pluto cocktails intensify. Now, the direct creation of  $\omega$  meson in primary NN collisions is possible only in C+C at 2 A GeV reactions. In the other two runs, we may see only sub-threshold production of  $\omega$ . Note that in case of the carbon runs, the substantial broadening of the  $\omega$  peak is caused by the low mass resolution.

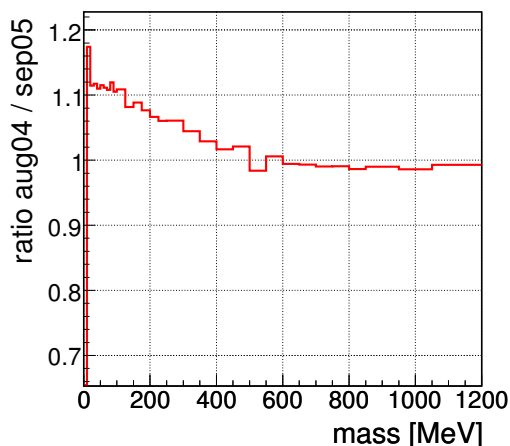


Figure 8.10.: Correction on differences in geometrical acceptance between the C+C at 1 A GeV (aug04) run and the Ar+KCl at 1.756 A GeV (sep05) run. The correction was estimated as the ratio of two invariant mass spectra obtained from the Ar+KCl Pluto cocktail which was filtered with the geometrical acceptance of the C+C at 1 A GeV experiment (numerator) and the geometrical acceptance of the Ar+KCl at 1.756 A GeV run (denominator).

In the right-hand side plot in Figure 8.9, I compare the experimental efficiency corrected invariant mass spectrum from the Ar+KCl run with the results of the predecessor C+C at 1 and 2 A GeV HADES measurements [38, 39]. For the purpose of the direct comparison of these three measurements, I reprocessed pair ntuples from the carbon experiments, but in contrast to [38, 39], I required in addition that pairs from C+C events should survive the cut on a size of lepton momentum  $100 < p < 1100$  MeV. Further, it was also necessary to take into account differences in geometrical acceptance between the C+C and Ar+KCl runs. The dissimilarities in the geometrical acceptances resulted mainly from different settings of the magnetic field. The Ar+KCl run was carried out with a stronger field with respect to the

## 8. Discussion of results

carbon runs. This correction was estimated based on the Ar+KCl Pluto cocktail filtered through the geometrical acceptance of the C+C at 1 A GeV measurement (aug04) and through the geometrical acceptance of the Ar+KCl run (sep05), see Figure 8.10. From the right-hand side plot in Figure 8.9, we find that the invariant mass distributions of pairs produced in the Ar+KCl and the C+C at 2 A GeV measurements are quite similar, despite the difference in beam energy 0.25 GeV/A unfavourable for Ar+KCl reactions. Nevertheless, in the mass range 0.15–0.55 GeV, Ar+KCl data points seem to slightly exceed the C+C at 2 A GeV spectrum. Let us point out that the corresponding Pluto cocktails exhibit the opposite order. This indicates a relative increase of the yield from “extra sources above  $\eta$ ” in Ar+KCl with respect to C+C at 2 A GeV collisions. In case of the C+C at 1 A GeV run, there was clearly not enough energy available to excite sources producing pairs with high invariant masses.

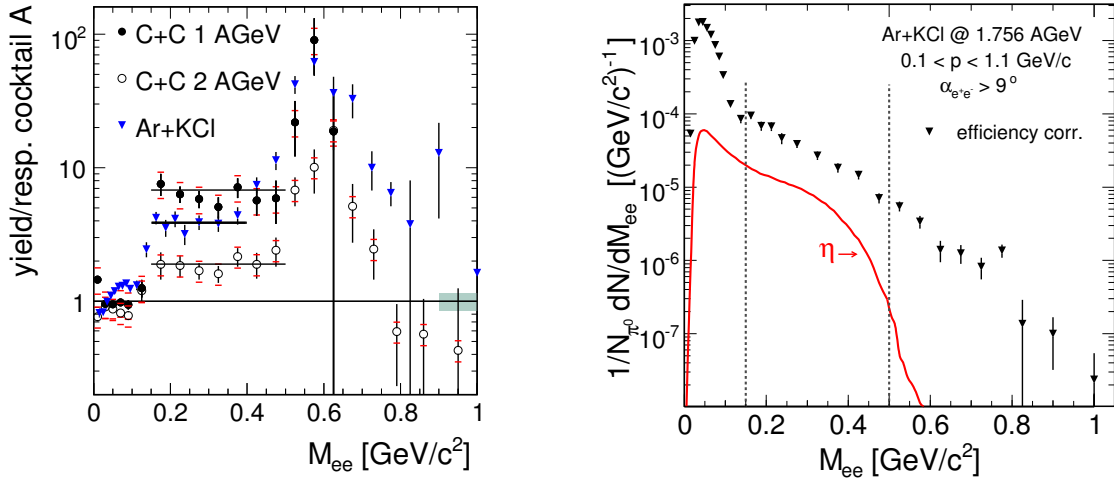


Figure 8.11.: **Left:** Ratio of an efficiency corrected invariant mass spectrum to the respective Pluto cocktail A. The ratio was evaluated for all three HADES nucleus-nucleus experiments in their particular geometrical acceptance. **Right:** The efficiency corrected pair invariant mass spectrum from the Ar+KCl run is compared with  $\eta$  Dalitz source from the Pluto event generator. The dotted vertical lines indicate the region, where the excess above  $\eta$  was calculated, i.e.,  $0.15 < M_{ee} < 0.5 \text{ GeV}$ .

For the three HADES nucleus-nucleus measurements, we evaluated the ratio between the experimental efficiency corrected data and the respective Pluto cocktail A, composed out of pairs from  $\pi^0$ ,  $\eta$ ,  $\omega$ , eventually also  $\phi$  decays, see the left-hand side plot in Figure 8.11. Like this, we may better see relative changes in participation of extra sources over the particular cocktail A when we change the reaction. Notice that all three distributions exhibit a plateau in the range of 0.15–0.50 GeV approximately. Pairs contributing to this invariant mass region originate from  $\eta$  Dalitz decays and, further, from some unknown extra sources creating the excess above  $\eta$ . The HSD calculation suggests which sources this might be, e.g.,  $\Delta$  Dalitz decay or NN Bremsstrahlung, see Figure 8.6. In paper [38], the HADES collabora-

tion proposed a procedure how to estimate the total yield  $N_{exc}$  in the full solid angle coming out of the sources which create the excess above  $\eta$  in the invariant mass region 0.15–0.50 GeV. As  $N_{exc}$  should not depend on particular detector acceptance, values of  $N_{exc}$  extracted from HADES and DLS measurements can be directly compared. Furthermore, by determining the total excess yield for different systems and energies, we may deduce some useful information about the sources producing the excess from the experimental point of view.

In the following steps, I am going to repeat the procedure described in the paper [38] to determine the  $N_{exc}$  for our Ar+KCl data:

1. The right-hand side plot in Figure 8.11 shows the experimental efficiency corrected invariant mass spectrum and the  $\eta$  Dalitz component of the Pluto cocktail. In the invariant mass region 0.15–0.50 GeV, I evaluated the ratio of the experimental pair yield  $\mathcal{Y}_{tot}$  and the  $\eta$  yield  $\mathcal{Y}_\eta$

$$F = \frac{\mathcal{Y}_{tot}}{\mathcal{Y}_\eta},$$

$$F = 4.6 \pm 0.2 (\text{stat}) \pm 1.6 (\text{syst}) \pm 1.2 (\eta).$$

The 35% systematic error was taken from Section 7.7. The third error, labeled ( $\eta$ ), takes into account the 25% uncertainty in determination of the  $\eta$  multiplicity by TAPS measurements [78, 79]. In order to be compatible with the values of  $N_{exc}$  extracted from the previous C+C measurements, I have neglected that the ratio of the Ar+KCl data to the Pluto cocktail A has the plateau shape only in the range 0.15–0.40 GeV, see the left-hand side plot in Figure 8.11. The extension to 0.15–0.50 GeV should introduce only a small systematic error, because the invariant mass spectrum steeply (exponentially) falls in this region. The influence of the two bins above 0.40 GeV upon the final result will, thus, be suppressed.

2. Since  $\mathcal{Y}_{tot}$  is a sum of the yield coming from  $\eta$  and the yield created by the sources producing the excess ( $\mathcal{Y}_{exc}$ ),  $F$  may be rewritten as

$$F = \frac{\mathcal{Y}_{exc} + \mathcal{Y}_\eta}{\mathcal{Y}_\eta} = 1 + \frac{\mathcal{Y}_{exc}}{\mathcal{Y}_\eta}.$$

3. To extrapolate the excess yield to the full solid angle, it is necessary to make two assumptions. First, pairs originating from the  $\eta$  Dalitz decay and from the sources creating the excess have similar acceptance in a given spectrometer. Second, sources producing the excess have similar dependence on centrality of a nucleus-nucleus collision as  $\eta$  meson. If this holds then  $N_{exc}$  can be determined as

$$N_{exc} = (F - 1) b_\eta m_\eta \xi. \quad (8.1)$$

Here  $b_\eta$  is the branching ratio to the  $\eta$  Dalitz decay ( $b_\eta = 0.006$ ) taken from [2]. The symbol  $m_\eta$  stands for the mean  $\eta$  meson multiplicity in minimum bias Ar+KCl at 1.756 A GeV reactions in the full solid angle ( $m_\eta = 0.046$ ) deduced

from the systematics of TAPS measurements. The fraction of  $\eta$  Dalitz decays, which contribute to the pair invariant mass region 0.15–0.50 GeV in the full solid angle, is denoted as  $\xi$ . Using the Pluto cocktail for Ar+KCl reactions, I estimated that  $\xi = 11.57\%$ . Finally, for the above-mentioned values, we obtain

$$N_{exc} = (115 \pm 5 \text{ (stat)} \pm 40 \text{ (syst)} \pm 40 \text{ } (\eta)) \times 10^{-6}.$$

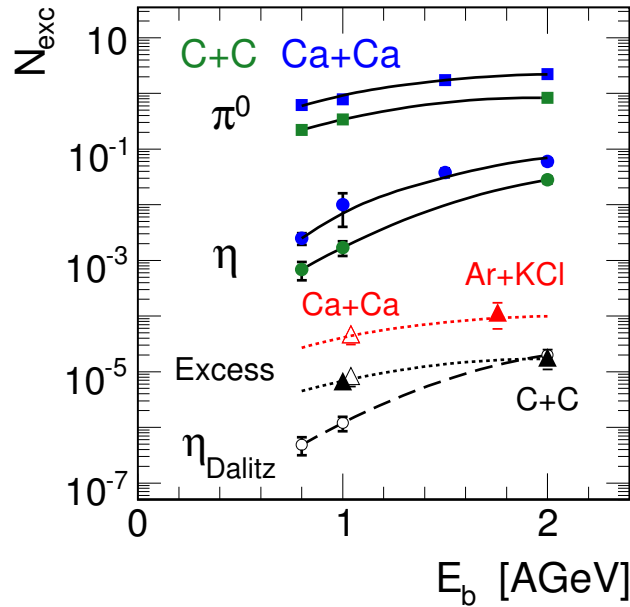


Figure 8.12.: The four upper curves show the inclusive mean meson multiplicities as a function of beam energy for C+C and Ca+Ca reactions. The blue (Ca+Ca) and the green (C+C) data points are based on TAPS measurements [78, 79]. The red and the black dotted curves below represent the probable dependence of the  $N_{exc}$  on the beam energy ( $E_b$ ) for Ca+Ca/Ar+KCl and C+C systems, respectively. See the text for explanation.

Now let us concentrate on Figure 8.12. The four upper curves show the dependence of the inclusive mean multiplicity of  $\pi^0$  and  $\eta$  mesons on the beam energy  $E_b$  in C+C (green points) and Ca+Ca (blue points) reactions. Data are based on TAPS measurements [78, 79]. The full triangles below correspond to the total yield of extra sources above  $\eta$  ( $N_{exc}$ ) measured by HADES in C+C at 1 and 2 A GeV runs (the full black triangles) [38] and in the Ar+KCl at 1.756 A GeV run (the full red triangle). The empty triangles depict the values of  $N_{exc}$  deduced from the DLS di-electron production measurements [34] in C+C at 1.04 A GeV (the black empty triangle) and Ca+Ca at 1.04 A GeV (the red empty triangle) reactions. In paper [38], the HADES collaboration claimed that the HADES and the DLS excess points from C+C collisions follow remarkably similar trend with the increasing beam energy per nucleon as the mean  $\pi^0$  multiplicity measured by TAPS. Indeed, the black

curve which connects the black triangles is just the  $\pi^0$  mean multiplicity dependence scaled down to fit the data points. The plot also shows that the dependence of  $\eta$  Dalitz multiplicity on the beam energy follows a bit different trend (empty circles connected with a dashed line in the bottom part of the plot). The plot suggests that also the DLS Ca+Ca point can be reasonably connected with the HADES Ar+KCl point. The connecting curve was obtained again just by downward scaling of the TAPS inclusive  $\pi^0$  mean multiplicity dependence from the Ca+Ca collisions. Notice that Ar+KCl and Ca+Ca reaction systems are of a comparable size. Each of the mentioned nuclei contains about 40 nucleons. To conclude, it seems that in this energy regime, the excess yield grows with the beam energy like  $\pi^0$  multiplicity also in case of medium size collision systems. Thus, the excess in the Ar+KCl/Ca+Ca system exhibits similar behaviour as it was observed in the lighter C+C system. Sources which create the excess are, thus, probably connected with pion production and propagation, involving, e.g.,  $\Delta$  and low-mass  $\rho$  excitations, and eventually also Bremsstrahlung processes.

When going from C+C to Ar+KCl/Ca+Ca system, it appears that the excess curves (dotted lines in Figure 8.12) scale with the varying system size differently than the curves of the inclusive mean  $\eta$  and  $\pi^0$  minimum bias multiplicities (solid curves in the upper part of Figure 8.12). In principle, in Equation (8.1), it would be more proper to use instead of the mean minimum bias  $\eta$  multiplicity  $m_\eta$  the mean  $\eta$  multiplicity measured in events selected by the first level trigger  $m'_\eta$  in particular reaction. The formula to calculate the excess would then look like

$$N'_{exc} = (F - 1) b_\eta m'_\eta \xi .$$

A problem is that HADES is not able to determine  $m'_\eta$ . From the analysis of charged pions, we can only assess  $m'_{\pi^0}$ , the mean  $\pi^0$  multiplicity in LVL1 events. Hence, the value of  $m'_\eta$  has to be extrapolated from the known data. In first order approximation, we may assume that in this energy range, the mean  $\eta$  multiplicity grows with the number of participants like the mean pion multiplicity, see the upper part of Figure 8.12. Thus, we have

$$m'_\eta = m_\eta m'_{\pi^0} / m_{\pi^0} ,$$

where the comma marks the mean meson multiplicities measured in LVL1 trigger events. The symbols without comma stand for the mean minimum bias meson multiplicities. Note that in the ratio  $N'_{exc}/m'_{\pi^0}$ , the trigger bias is suppressed as it follows from

$$N'_{exc}/m'_{\pi^0} = (F - 1) b_\eta \xi m_\eta / m_{\pi^0} = N_{exc}/m_{\pi^0} .$$

Let us recall that the inclusive mean pion multiplicity should be proportional to the number of participants. When  $N_{exc}/m_{\pi^0}$  is evaluated for Ar+KCl and C+C system, we may investigate, how the total yield above  $\eta$  changes with varying system size. Following this idea, we have for the Ar+KCl data

$$\begin{aligned} N'_{exc}/m'_{\pi^0}|_{\text{Ar+KCl } 1.756 \text{ A GeV}} &= N_{exc}/m_{\pi^0}|_{\text{Ar+KCl } 1.756 \text{ A GeV}} = \\ &= (5.6 \pm 0.2 \text{ (stat)} \pm 2. \text{ (syst)} \pm 2. (\eta) \pm 0.6(\pi^0)) \times 10^{-5} . \end{aligned}$$

## 8. Discussion of results

---

Here, the pion multiplicity was taken from Table 8.1. The last error, labelled ( $\pi^0$ ), takes into account the 11 % uncertainty of the mean inclusive pion multiplicity.

The paper [38] quotes that for C+C at 2 A GeV measurement, the total excess yield was

$$N_{exc}|_{C+C \ 2A \ GeV} = (18 \pm 4 \text{ (stat)} \pm 7 \text{ (syst)} \pm 4 \text{ (\eta)}) \times 10^{-6} .$$

The value of  $N_{exc}|_{C+C \ 1.756A \ GeV}$  should, however, be a bit lower, around  $13.6 \times 10^{-6}$  as it is forecast by the dotted black curve connecting the black triangles in Figure 8.12. Assuming the excess scales with the beam energy like  $\pi^0$  multiplicity, we may write

$$\begin{aligned} N'_{exc}/m'_{\pi^0}|_{C+C \ 1.756A \ GeV} &= N_{exc}/m_{\pi^0}|_{C+C \ 1.756A \ GeV} = N_{exc}/m_{\pi^0}|_{C+C \ 2A \ GeV} = \\ &= (2.2 \pm 0.5 \text{ (stat)} \pm 0.8 \text{ (syst)} \pm 0.5 \text{ (\eta)} \pm 0.2(\pi^0)) \times 10^{-5} . \end{aligned}$$

Here the mean minimum bias pion multiplicity for C+C 2 A GeV collisions was taken from Figure 8.12,  $m_{\pi^0}|_{C+C \ 2A \ GeV} = (0.83 \pm 0.08)$ .

It appears that the ratio  $N_{exc}/m_{\pi^0}$  increases when moving from C+C to the heavier Ar+KCl/Ca+Ca system. Therefore, some non-trivial dependence of the total yield of the excess on the number of participants can be expected. However, to make any definite statement, systematic and statistical errors have to be reduced.

## 9 Summary and conclusions

The thesis reports on a HADES measurement of inclusive electron-positron pair emission from Ar+KCl collisions at a kinetic beam energy of 1.756 A GeV. The experiment was carried out with my active participation at GSI Darmstadt in September and October 2005.

Investigation of production and properties of the light vector mesons in hot and dense nuclear matter through their di-electron decay is one of the key topics pursued by the HADES collaboration in their long-time research programme. Data from this activity will help us to understand better to what extent the light vector mesons modify in the surrounding hadronic medium in the SIS/Bevalac energy regime of 1–2 A GeV. After the two pioneering C+C runs [38, 39], Ar+KCl is the heaviest nucleus-nucleus system which has been studied so far using the HADES spectrometer. In the future, the collaboration will continue in this research programme with a series of measurements performed with even heavier systems, like Ni+Ni or Au+Au. Data provided by HADES are also a valuable wellspring of information about various rare sources of electron-positron pairs, e.g, NN Bremsstrahlung and  $\Delta$  Dalitz decay. Therefore, the spectrometer is also used to measure di-electron production in elementary reactions such as p+p or p+n.

In the Ar+KCl run, we managed to collect amount of data corresponding to about  $2.1 \times 10^9$  first level trigger events. The first level trigger signal was derived from a charged particle multiplicity  $\geq 16$  in the Time of flight wall. The mean pion multiplicity in first level trigger events was with respect to minimum bias reactions two times bigger. At the  $\omega$  pole mass, the expected mass resolution is slightly better than 3 %.

My analysis proceeded as follows. Electrons/positrons candidates were selected out of tracks which were associated with Cherenkov RICH rings. RICH rings had to satisfy several quality criteria. Further, each lepton candidate had to have its velocity within a certain range defined by the Time of flight wall resolution. Finally, for lepton candidates detected in the TOFino-Shower region, the positive lepton signature from the Shower detector was required. The average purity of the reconstructed lepton sample was well above 95 %. I checked this by means of the UrQMD simulation as well as by an alternative approach based on event mixing of experimental data, which I developed.

Di-electrons were assembled from identified single electrons and positrons. A requisite was to suppress contributions of photon conversion, misidentified hadrons, and tracking fakes. Conversion pairs were effectively rejected with an opening angle cut ( $\alpha_{e^+e^-}^{op} > 9^\circ$ ). Tracking fakes were removed from the sample by means of selecting uniquely defined good quality tracks. Further, I applied a cut on a lepton momentum size which required  $100 < p < 1100$  MeV/c. The upper cut reduced the hadron contamination of the lepton sample.

I compared the reconstructed and efficiency corrected invariant mass, transverse momentum, and rapidity distributions corresponding to signal pairs with predictions of thermal model based Monte Carlo event generator Pluto. The Pluto generator employs known experimental data on production of neutral mesons in the studied

## 9. Summary and conclusions

energy region. Above the invariant mass 0.15 GeV, the efficiency corrected spectra of pairs from Ar+KCl exhibit a large excess over our Pluto cocktail, which was composed from electromagnetic decays of the long-lived components ( $\pi^0$ ,  $\eta$ ,  $\omega$ , and  $\phi$ ) of the fireball.

Further, I made a comparison of my efficiency corrected spectra with predictions of sophisticated transport code HSD. The HSD code seems to describe the experimental distributions of pairs reasonably, see Figure 9.1. HSD assumed either the “vacuum” or the “in-medium” behaviour of  $\rho^0$  and  $\omega$  spectral function. In the “in-medium” scenario, the spectral function of the given vector meson underwent collisional broadening and mass shift simultaneously. The “in-medium” cocktail seems to describe the measured data better. Nevertheless, within the current systematic and statistical errors, I am not able to reject any of the scenarios. The HSD simulations indicate the relevance of pair production from decays of short-lived resonances in the SIS/Bevalac energy regime of 1–2 A GeV.

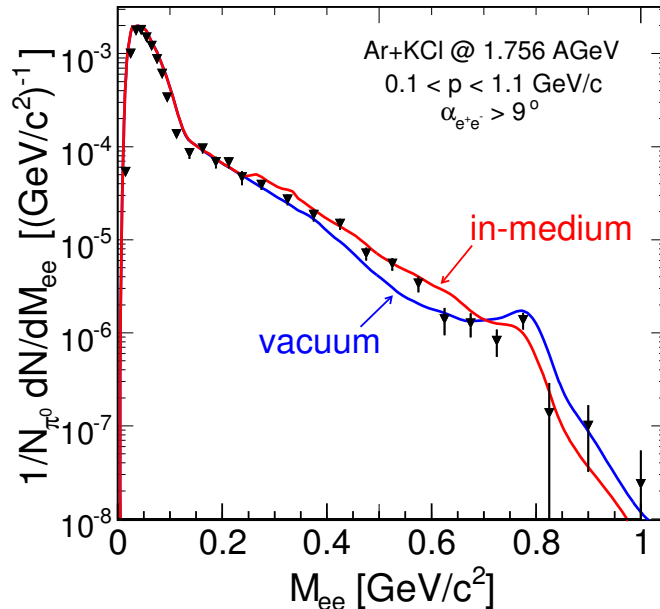


Figure 9.1.: The efficiency corrected invariant mass spectrum of  $e^+e^-$  pairs from Ar+KCl collisions at 1.756 A GeV (black triangles) is compared with two predictions of the HSD transport code. The HSD calculations assumed either “vacuum” (blue curve) or “in-medium” (red curve) behaviour of spectral functions for the light vector mesons  $\rho$  and  $\omega$ . The errors which are shown are statistical. All spectra are normalized per one neutral pion.

Further, in a model dependent way, I studied the total yield from the extra sources which create an excess above the expected production rate from the  $\eta \rightarrow \gamma e^+e^-$  decay in the invariant mass region 0.15–0.50 GeV. The HADES Ar+KCl measurement together with the data from the DLS Ca+Ca experiment support the idea that the total yield from this excess grows with the beam energy like the inclusive mean  $\pi^0$  multiplicity. Sources which create the excess are, thus, probably connected with pion production and propagation, involving, e.g.,  $\Delta$  and low-mass  $\rho$  excitations, and

---

eventually Bremsstrahlung processes. We have also pointed out that there might be a non-trivial dependence of this excess on the number of reaction participants.

I consider the main contributions of the thesis to be the following:

- Calibration of the TOF detector in the Ar+KCl run.
- New design of the first level trigger emulator which enabled to determine the range of selected impact parameters in the Ar+KCl run.
- Development of a method which allows to assess purity of the sample of identified leptons. This method is based on event mixing of experimental data and its results are consistent with the purity determined from our simulation.
- The main outputs of the thesis are invariant mass, rapidity, and transverse momentum spectra of pairs corrected on reconstruction efficiency.
- The obtained efficiency corrected spectra were compared with predictions of Pluto and HSD.
- Investigation of the total yield from the sources, creating the excess above the expected  $\eta$  Dalitz contribution, for the Ar+KCl system using a model dependent approach.

# A Efficiency correction

In Section 7.5, we skipped some important intermediate figures and steps, which should be shown to increase a confidence in our efficiency corrected spectra. Therefore, this appendix deals in more detail with correction on efficiency and self-consistency check procedure.

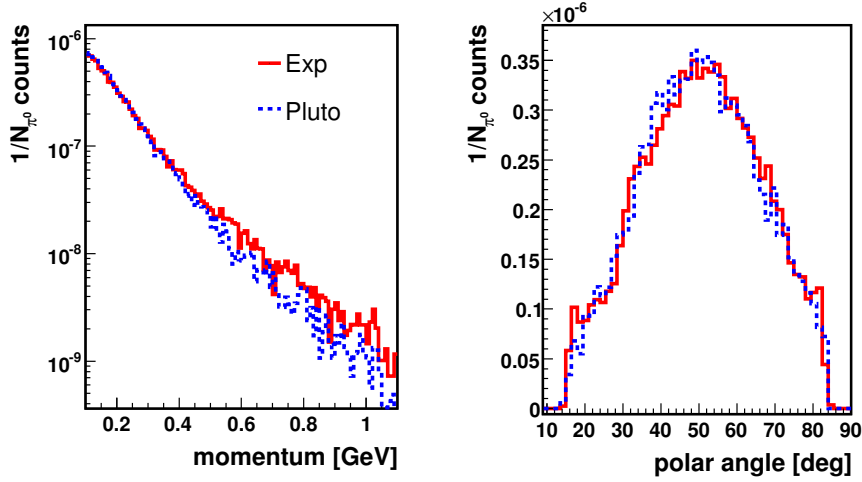


Figure A.1.: Distributions of momentum (**Left**) and polar emission angle (**Right**) of signal single leptons. Comparison between the experiment (red solid line) and the scaled down simulated Pluto cocktail B (blue dashed line). Experimental distributions are normalized per one neutral pion. Spectra are not efficiency corrected.

In Section 6.5, I contrasted single electron/positron distributions from the experiment and the UrQMD simulation. At that level of our analysis, a large part of electrons and positrons originated from sources producing mainly close pairs. The subsequent pair cuts reduced, however, the number of close pairs significantly, see Section 7.3. At the pair level of the analysis, the experimental and the simulated distributions of single leptons are comparable only after all the pair cuts are applied and the combinatorial background is subtracted. In this way, we obtain distributions corresponding to “signal single leptons”, see Figure A.1. Simulated distributions were scaled down by a factor 1.69 to sit on top of the experimental data. On the left-hand side plot, we may see a momentum distribution corresponding to signal single leptons. Up to the momentum 0.5 GeV, our simulation (Pluto cocktail B) provides a good description of the shape of the experimental data. This is the region, where  $\pi^0$  Dalitz decay is the dominant source of di-leptons. Above the momentum 0.5 GeV, the experiment exhibits a somewhat harder momentum spectrum of leptons. The hard tail of the spectrum can originate, for instance, from decays of baryonic resonances produced in early stages of a nuclear collision. To the contrary, Pluto was designed to generate a pair cocktail at the point of the thermal freeze-out. The right-hand side plot in Figure A.1 shows a distribution of polar emission angle of signal single leptons.

Hence, we have shown that our simulation, scaled down by a factor 1.69, reliably reproduces the shape of experimental single lepton distributions at least for the electrons and positrons from the  $\pi^0$  Dalitz source. A possible source of the observed discrepancy is probably located in RICH or MDC digitizers. In the future, it is necessary to remove this drawback.

Now, let us deal with the procedure of the self-consistency check. This test is used to estimate to what extent are our efficiency corrected spectra under control. At the beginning of the self-consistency check, we have a pair cocktail. The analysis then proceeds simultaneously in two branches:

1. We process the initial cocktail with our analysis chain (HGeant, digitizers, lepton identification, pair cuts) and at the end, we obtain efficiency corrected signal spectra.
2. Out of the initial cocktail, signal pairs are selected. Those, which are not in the geometrical acceptance of the spectrometer, are excluded. In the next step, momenta of leptons are realistically smeared and we test whether the pairs survive our physical cuts, i.e., the 9 deg cut on the opening angle and the cut on size of momentum of each pair leg  $100 < p < 1100$  MeV. Finally, we fill histograms corresponding to the signal.

If our analysis end efficiency correction works properly, the spectra obtained from 1. and 2. should overlay.

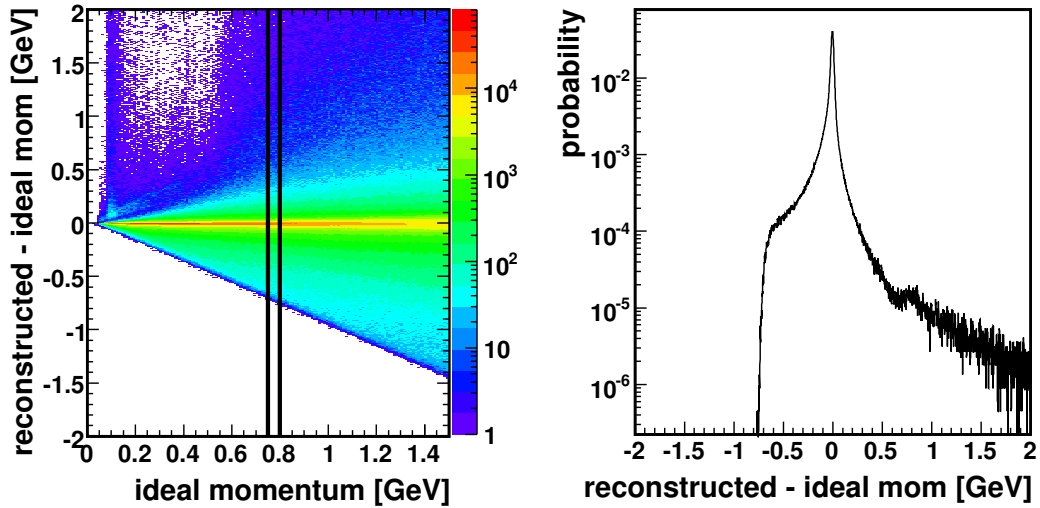


Figure A.2.: **Left:** Distribution of reconstructed minus ideal momentum versus ideal momentum. The distribution was obtained from white lepton spectrum (sector with 4 MDCs). The region between the two black lines is projected on the y-axis and shown in the plot on **Right**.

In the branch 2., we have to estimate smearing corrections without running the HGeant simulation. In our case, the smearing was generated using a set of two dimensional histograms which contained distributions of the reconstructed minus

the ideal size of momentum (or polar or azimuthal angle) versus the ideal size of momentum, for illustration see the left-hand side plot in Figure A.2. Such histograms were filled using the information from a white lepton spectrum<sup>1</sup> which was processed with our full analysis chain (Geant, digitizers, tracking, and identification). The smearing of lepton momentum size (or angles) then proceeds in the following way. For a given ideal momentum size, the corresponding probability density distributions for momentum and angular smearing were projected, for illustration see the right-hand side plot in Figure A.2. According to these distributions, we randomly sampled the smearing corrections. Since the sectors with 3 and 4 MDC layers exhibit different resolution, we used for both cases two different sets of histograms.

For the purpose of the self-consistency check, we generated events containing the full Pluto cocktail. Before analyzing the cocktail with our analysis chain (see the branch 1. above), the Pluto cocktail was embedded into real data. This provided us a realistic environment for each event.

Results of the self-consistency check made with these data can be seen in Figures A.3, A.4, and A.5. In general, we see fairly good agreement between the acceptance filtered+smear cocktail (histograms) and the reconstructed+efficiency corrected data (black points). The realistic momentum smearing is necessary to reliably reproduce the shape of the reconstructed  $\omega$  peak. The only problematic region where the self-consistency check exhibits larger discrepancies lies at the large pair rapidities. The reconstructed+efficiency corrected rapidity distribution seems to be shifted with respect to acceptance filtered+smear cocktail histogram. Meanwhile we suspect that this feature has some connection to differences in the geometry versions which were used to generate the efficiency matrices and the Pluto cocktail for the self-consistency check. The whole thing is under investigation. Nevertheless, if we would not consider the two last points in the rapidity distributions, the maximum discrepancies do not exceed 25 %.

---

<sup>1</sup>Leptons randomly sampled from a uniform momentum and a uniform angular distribution.

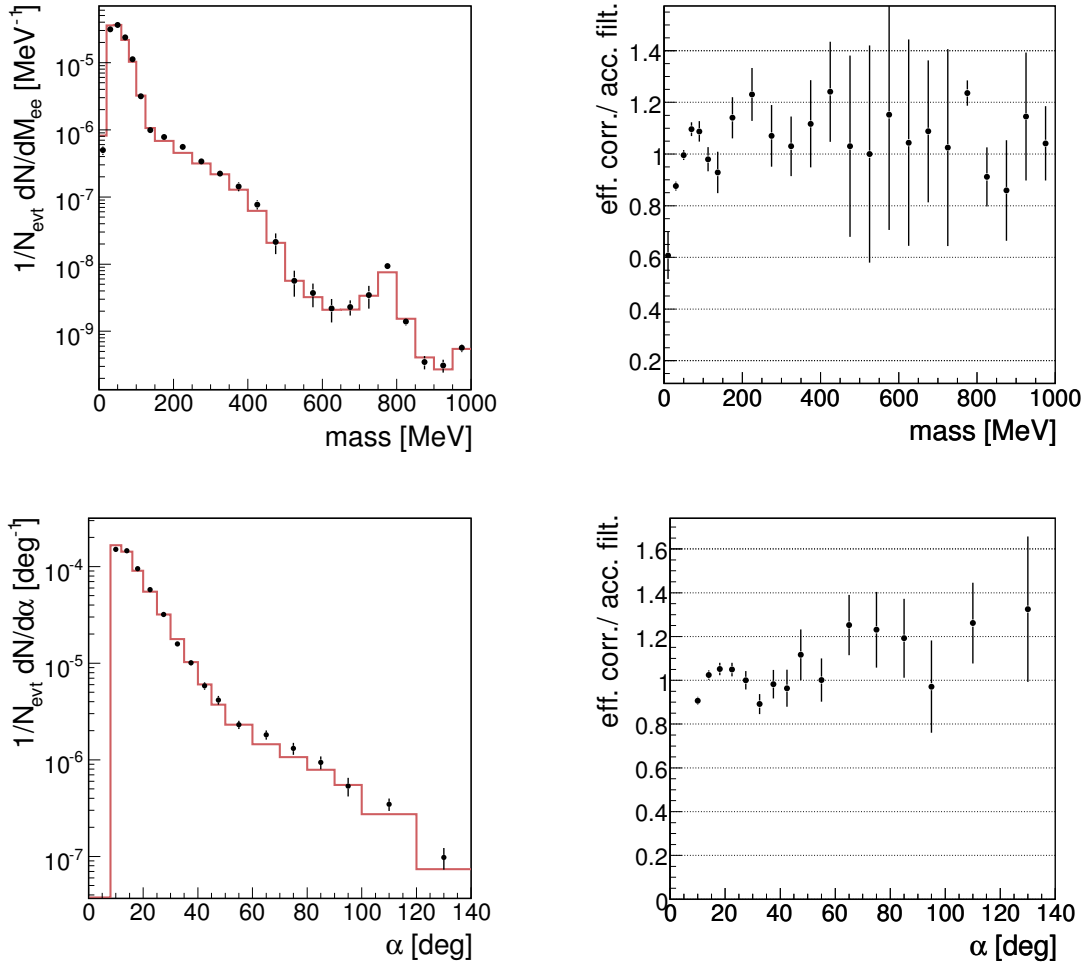


Figure A.3.: **Left:** Invariant mass and opening angle ( $\alpha$ ) spectrum of signal pairs from the full Pluto cocktail. The reconstructed+efficiency corrected data are marked with black points. The brown histograms show the acceptance filtered+momentum smeared cocktail. Spectrum is normalized per one event. **Right:** Ratio of the reconstructed+efficiency corrected data and the corresponding acceptance filtered+momentum smeared cocktail.

## A. Efficiency correction

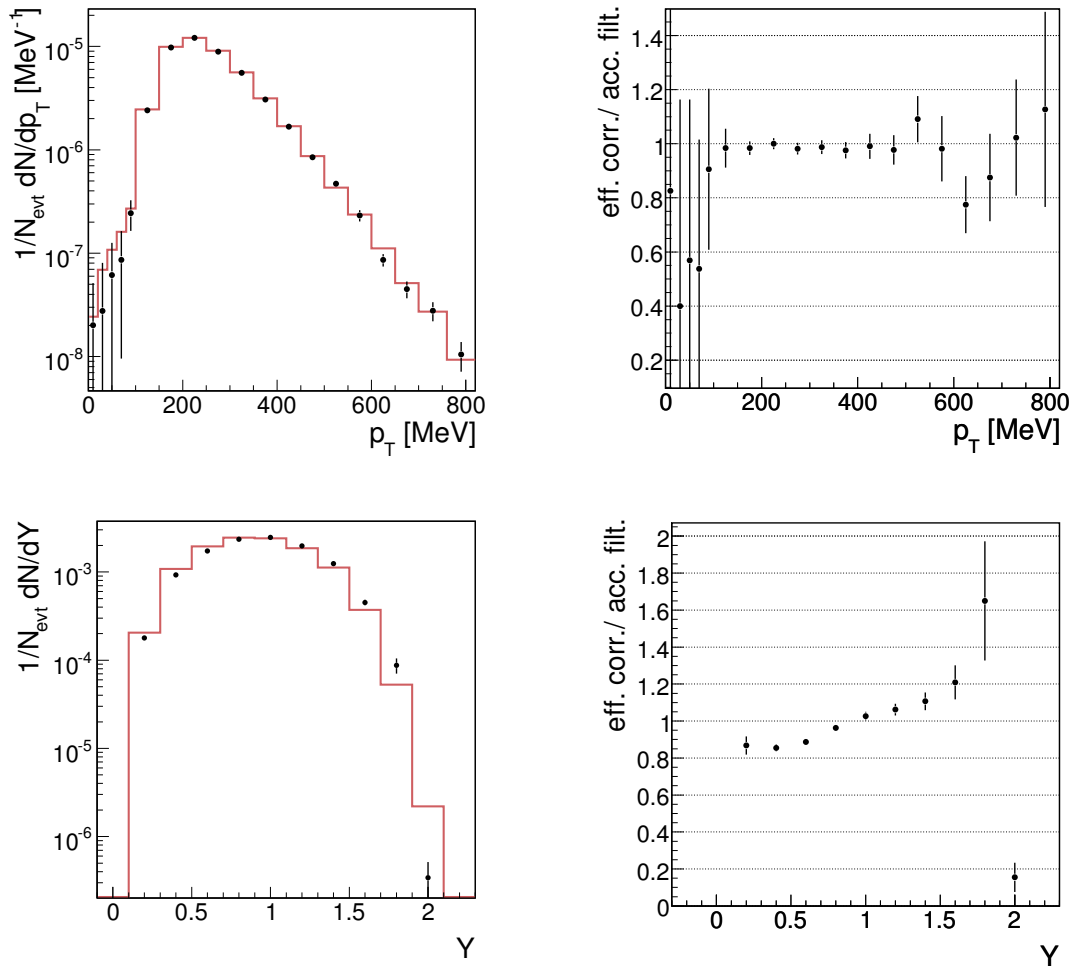


Figure A.4.: **Left:** Transverse momentum ( $p_T$ ) and rapidity ( $Y$ ) spectra of signal pairs from the full Pluto cocktail. The reconstructed+efficiency corrected data are marked with black points. The brown histograms show the acceptance filtered+momentum smeared cocktail. Spectra are normalized per one event. **Right:** Ratio of the reconstructed+efficiency corrected data and the corresponding acceptance filtered+momentum smeared cocktail.

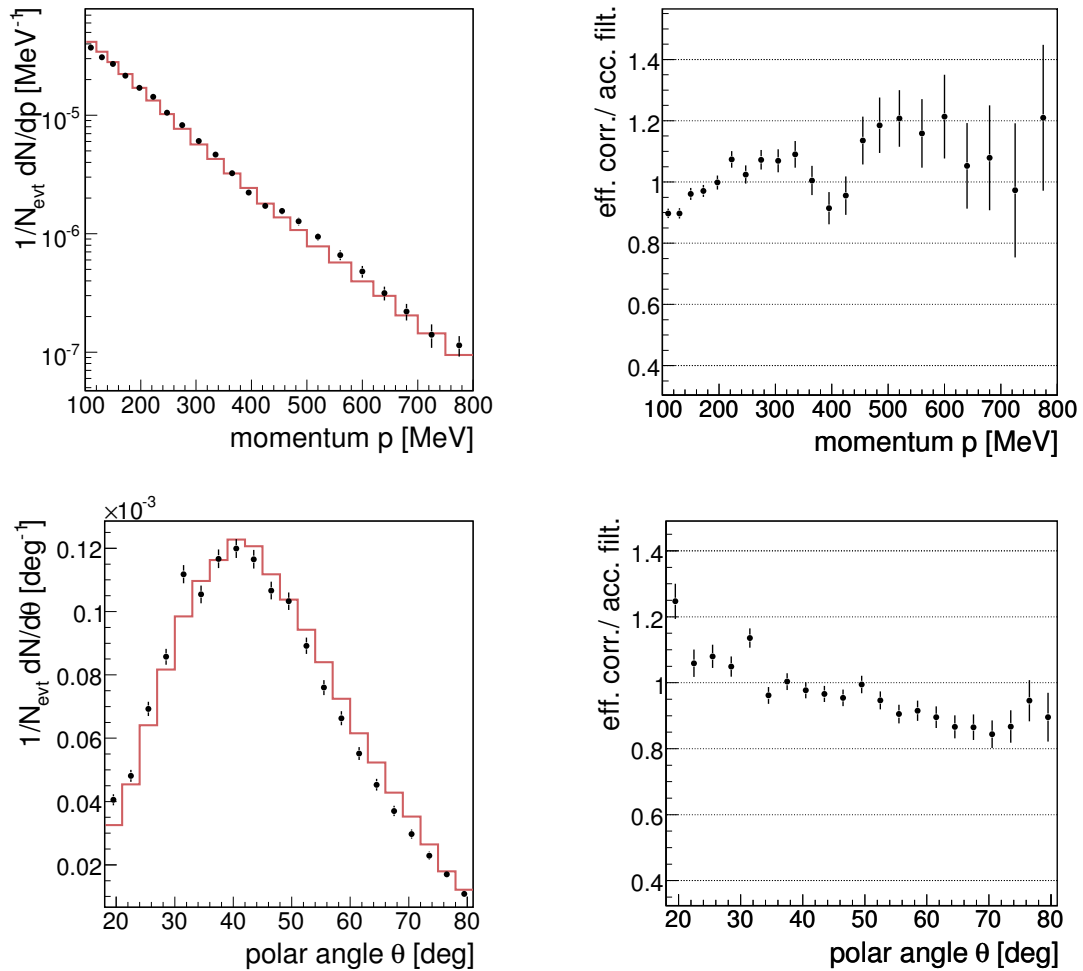


Figure A.5.: **Left:** Momentum and polar emission angle distributions of signal single leptons from the full Pluto cocktail. By the term “signal single leptons”, I mean distributions corresponding to single leptons after all pair cuts were applied and the combinatorial background was subtracted. The reconstructed+efficiency corrected data are marked with black points. The brown histograms show the acceptance filtered+momentum smeared cocktail. Spectra are normalized per one event. **Right:** Ratio of the reconstructed+efficiency corrected data and the corresponding acceptance filtered+momentum smeared cocktail.



# Bibliography

- [1] P. Braun-Munzinger and J. Stachel, Nucl. Phys. A **638** (1998), p. 3.
- [2] Particle data group: *Particle Physics Booklet*, (2002).
- [3] R. Rueckel, Phys. Lett. B **64** (1976), p. 39.
- [4] E.L. Bratkovskya, W. Cassing, R. Rapp, J. Wambach, Nucl. Phys. A **634** (1998), p. 168–189.
- [5] R. Rapp, J. Wambach, Adv. Nucl. Phys. **25** (2000), p. 1.
- [6] P. Salabura et al., Prog. Part. Nucl. Phys. **53** (2004), p. 49.
- [7] P. Salabura et al., Nucl. Phys. A **749** (2005), p. 150.
- [8] S. Yurevich et al.: *Latest results on  $e^+e^-$  pair production in CERES, Proc. of the 18th Nucl. Phys. Div. Conf. of the EPC (NPDC18), Prague, 23.-29. August 2004.*
- [9] M. Gell-Mann, R.J. Oakes, B. Renner: Phys. Rev. **175** (1968), p. 2195.
- [10] U. Vogl, W. Weise, Prog. Part. Nucl. Phys. **27** (1991), p. 195.
- [11] S. Scherer: *Introduction to Perturbation Theory*, (2002), hep-ph/0210398.
- [12] S. Klimt et al., Phys. Lett. B **249** (1990), p. 386.
- [13] J. Gasser, H. Leutwyler, Phys. Lett. B **184** (1987), p. 83.
- [14] R. D. Pisarski, Phys. Rev. D **52** (1995), p. 3773.
- [15] U.-G. Meissner, Phys. Rep. **161** (1988), p. 213.
- [16] C. Song, Phys. Rev. D **48** (1993), p. 1375.
- [17] K. Haglin, Nucl. Phys. A **584** (1995), p. 719.
- [18] S. Gao, C. Gale, C. Ernst, H. Stöcker, W. Greiner, nucl-th/9812059.
- [19] G.E. Brown, M. Rho, Physics Reports **363** (2002), p. 85–171.
- [20] T. Hatsuda, T. Lee, Phys. Rev. C **46** (1992), p. 34.
- [21] M. Urban, M. Buballa, R. Rapp, and J. Wambach, Nucl. Phys. A **641** (1998), p. 433.
- [22] F. Klingl, N. Kaiser, W. Weise, Nucl. Phys. A **624** (1997), p. 527.
- [23] W. Peters, M. Post, H. Lenske, S. Leupold, U. Mosel, Nucl. Phys. A **632** (1998), p. 109.

- [24] I. Tserruya, Eur. Phys. J. C **43** (2005), p. 399–405.
- [25] K. Ozawa et al., Nucl. Phys. A **698** (2002), p. 535–538.
- [26] R. Muto et al., J. Phys. G **30** (2004), p. 1023–1026.
- [27] M. Sekimoto et al., Nucl. Instr. Meth. A **516** (2004), p. 390.
- [28] B. Mecking et al., Nucl. Instr. Meth. A **503** (2003), p. 513.
- [29] C. Djalali et al.: *Search For Modification of Vector Mesons properties*, plenary talk at Meson 2008 conference, Cracow, Poland, June 6–11, 2008.
- [30] M.A. Kagarlis et al., Phys. Rev. C **60** (1999), 025203.
- [31] D. Trnka et al., Phys. Rev. Lett. **94** (2005), 192303.
- [32] V. Metag: *Medium modifications of mesons*, talk at 20th Indian Summer School, Řež, Czech Republic, August 27–31, 2008.
- [33] H.S. Matis et al., Nucl. Phys. A **583** (1995), p. 617–622.
- [34] R.J. Porter et al., Phys. Rev. Lett. **79** (1997), p. 1229–1232.
- [35] A. Yegneswaran et al., Nucl. Instr. and Meth. A **290** (1990), p. 61.
- [36] E.L. Bratkovskya, W. Cassing, M. Effenberger, U. Mossel, Nucl. Phys. A **653** (1999), p. 301–317.
- [37] E.L. Bratkovskya, W. Cassing, Nucl. Phys. A **619** (1997), p. 413–446.
- [38] G. Agakichiev et al., Phys. Lett. B **663** (2008), p. 43–48.
- [39] G. Agakichiev et al., Phys. Rev. Lett. **98** (2007), 052302.
- [40] <http://www-subatech.in2p3.fr/theo/qmd/sources/iqmd.html#A10>
- [41] J.P. Wessels, Eur. Phys. J. A **18** (2003), p. 521–525.
- [42] P. Wurm et al., Nucl. Phys. A **590** (1995), p. 103–116.
- [43] G. Agakichiev et al., Phys. Rev. Lett. **75**(1995), p. 1272.
- [44] P. Sonderegger, J. Phys. G **30** (2004), p. 1027–1030.
- [45] R. Arnaldi et al., Eur. Phys. J. C **49** (2007), p. 235–241.
- [46] R. Arnaldi et al., Phys. Rev. Lett. **96** (2006), 162302.
- [47] M. Masera et al., Nucl. Phys. A **590** (1995), p. 93–102.
- [48] W. Cassing, W. Ehehalt and C.M. Ko, Phys. Lett. B **363** (1995), p. 35.
- [49] W. Cassing, W. Ehehalt and I. Kralik, Phys. Lett. B **377** (1996), p. 5.
- [50] T. Åkesson et al., Z. Phys. C **68** (1995), p. 47–64.
- [51] C. Baglin et al., Phys. Lett. B **220** (1989), p. 471–478.

- 
- [52] M. Gonin, Nucl. Phys. A **610** (1996), p. 404–417.
- [53] G.E. Brown and M. Rho, arXiv:nucl-th/0509001.
- [54] G.E. Brown and M. Rho, arXiv:nucl-th/0509002.
- [55] E. Scomparin: *Dimuon and charm production in In+In collisions at the CERN SPS*, plenary talk at Quark Matter conference, Budapest, Hungary, August 4–9, 2005.
- [56] T.J. Hallman and J. Thomas, Nucl. Phys. A **590** (1995), p. 399.
- [57] D.P. Morrison et al., Nucl. Phys. A **638** (1998), p. 565.
- [58] K. Adcox et al.: *Formation of dense partonic matter in relativistic nucleus-nucleus collisions at RHIC: Experimental evaluation by the PHENIX collaboration*, Hunting the Quark Gluon Plasma, BNL-73847-2005.
- [59] A. Toia: *Dileptons at RHIC*, talk at Electromagnetic Probes of Strongly Interacting Matter workshop, ECT\* Trento, Italy, June 18–22, 2007.
- [60] G. Agakichiev et al.: “The HADES Di-Electron Spectrometer at GSI Darmstadt”, to be published in Nucl. Instr. Meth.
- [61] A. Kugler et al., Nucl. Phys. A **737** (2004), p. 78.
- [62] R. Shicker et al., Nucl. Instrum. Meth. A **380** (1996), p. 586.
- [63] HYDRA - HADES analysis package; <http://www-hades.gsi.de/>.
- [64] <http://root.cern.ch>.
- [65] <http://consult.cern.ch/writeup/geant/>.
- [66] I. Froehlich et al., arXiv:nucl-ex/0708.2382v2.
- [67] M.A. Kagarlis.: *Pluto++*, a Monte Carlo simulation tool for hadronic physics, GSI report (2000).
- [68] W.H. Press, S.A. Teukolsky, W.T. Vetterling, and B.P. Flannery: “Numerical Recipes”, 3<sup>rd</sup> Edition, Cambridge University Press (2007).
- [69] S.A. Bass et al., Prog. Part. Nucl. Phys. **41** (1998), p. 225–370.
- [70] M. Bleicher et al., J. Phys. G **25** (1999), p. 1859–1896.
- [71] <http://th.physik.uni-frankfurt.de/~urqmd/>
- [72] J. Otwinowski: *Pomiar widm par  $e^+e^-$  wyprodukowanych w zderzeniach  $^{12}C+^{12}C$  przy energii  $E_{kin} \leq 2$  AGeV przy użyciu spektrometru HADES*, Ph.D. thesis, Jagellonian University Krakow 2003.
- [73] M. Jurkovič: *The way to  $e^+/e^-$  from Ar+KCl*, talk from Hades collaboration meeting XVII, October 2006.
- [74] P. Tlustý: *Production of charged pions in Ar+KCl*, talk from Hades collaboration meeting XIX, July 2007.

- [75] M.A. Gaunar-Hering: *Dielectron production in heavy ion collisions at 158 GeV/c per nucleon*, Ph.D. thesis, Technical University Darmstadt 2001.
- [76] R. Brockmann et al., Phys. Rev. Lett. **53** (1984), p. 2012–2015.
- [77] F.-D. Berg et al., Phys. Rev. Lett. **72** (1994), p. 977.
- [78] R. Auerbeck et al., Z. Phys. A **359** (1997), p. 65–73.
- [79] R. Auerbeck et al., Phys. Rev. C **67** (2003), 024903.
- [80] W. Cassing and E.L. Bratkovskaya, Phys. Reports **308** (1999), p. 65–233.
- [81] E.L. Bratkovskaya, W. Cassing, and U. Mosel, Phys. Lett. B **424** (1998), p. 244.
- [82] C. Ernst et al., Phys. Rev. C **58** (1998), p. 447.
- [83] C.M. Ko, C.Q. Li, G.E. Brown, and H. Sorge, Nucl. Phys. A **610** (1996), p. 342.
- [84] C. Fuchs and A. Faessler, Prog. Part. Nucl. Phys. **53** (2004), p. 59–75.
- [85] E.L. Bratkovskaya, W. Cassing, Nucl. Phys. A **807** (2008), p. 214–250.